
# Soil-structure-interaction analysis in support of Groningen - B-stations verification efforts

**Francesco Cavalieri, António A. Correia**

**MOSAYK**

Date April 2020

Editors Jan van Elk & Dirk Doornhof

# General Introduction

The ground motion models are developed ideally based on free-field recording and developed to predict free field ground motions. These recordings are not impacted by the interaction between the soil and a building. However, for larger buildings the transfer of ground movement into the structure of the building can be dynamically influenced by the structure. Soil-structure interaction describes the coupling between the structure of the building to the supporting soil through the foundations.

Extensive studies have been carried out by Deltares to prepare a detailed map of the shallow subsurface (Ref. 1 to 3). Based on the description of the shallow sub-surface, amplification factors of the ground motion have been derived and included in the ground motion model (GMM) (Ref. 4).

Using representative values of the amplification factor, the response of a selection of buildings to earthquake motion was analysed for the purpose of the hazard and risk assessment. The soil-structure interaction models prepared for the index buildings used in the derivation of fragility functions were used in hazard and risk assessment (Ref. 5). The foundation of the buildings is important in the transfer of the ground motion into the buildings. For a selection of index buildings with shallow foundations as wells as buildings with pile foundations soil-structure interaction was evaluated (Ref. 6).

The B-stations accelerometers of the KNMI seismic monitoring network are housed in buildings. In this report the potential impact of the soil structure interaction resulting from these buildings on the records from these stations is investigated.

AN earlier version of this report was published in May 2020. This version supersedes this May version.

# References


1. Geological schematisation of the shallow subsurface of Groningen. For site response to earthquakes for the Groningen gas field. part 1 to 3, Pauline Kruiver, Ger de Lange, Ane Wiersma, Piet Meijers, Mandy Korff, Jan Peeters, Jan Stafleu, Ronald Harting, Roula Dambrink, Freek Busschers and Jan Gunnink, Deltares and NAM, June 2015.
2. Modifications of the Geological model for Site response at the Groningen Field, P. Kruiver, Deltares, June 2016.
3. Background document NAM database of subsurface information - Version date of database - 29 March 2018, Pauline Kruiver, Fred Kloosterman, Ger de Lange, Pieter Doornenbal, Deltares, Mar 2018.
4. V6 Ground-Motion Model (GMM) for Induced Seismicity in the Groningen Field With Assurance Letter, Julian J Bommer, Benjamin Edwards, Pauline P Kruiver, Adrian Rodriguez-Marek, Peter J Stafford, Bernard Dost, Michail Ntinalexis, Elmer Ruigrok and Jesper Spetzler, December 2019.
5. Report on the v6 Fragility and Consequence Models for the Groningen Field, Helen Crowley, Rui Pinho and Francesco Cavalieri, March 2019
6. Calibration and verification of a nonlinear macro-element for SSI analysis in the Groningen region, Francesco Cavalieri, António A. Correia, MOSAYK, April 2019
7. Soil-structure-interaction analysis in support of Groningen - B-stations verification efforts, Francesco Cavalieri, António A. Correia, mosayk, May 2020.

NAM

| | | | |
|---|---|---|---|
| **Title** | **Soil-structure-interaction analysis in support of Groningen - B-stations verification efforts** | **Date** | December 2019 |
| | | **Initiator** | NAM |
| **Autor(s)** | **Francesco Cavalieri, António A. Correia** | **Editors** | Jan van Elk and Dirk Doornhof |
| **Organisation** | **MOSAYK** | **Organisation** | NAM |
| **Place in the Study and Data Acquisition Plan** | Study Theme: Seismic Response of Buildings (URM)<br>Comment:<br>The ground motion models are developed ideally based on free-field recording and developed to predict free field ground motions. These recordings are not impacted by the interaction between the soil and a building. However, for larger buildings the transfer of ground movement into the structure of the building can be dynamically influenced by the structure. Soil-structure interaction describes the coupling between the structure of the building to the supporting soil through the foundations.<br>Extensive studies have been carried out by Deltares to prepare a detailed map of the shallow subsurface. Based on the description of the shallow sub-surface, amplification factors of the ground motion have been derived and included in the ground motion model (GMM).<br>Using representative values of the amplification factor, the response of a selection of buildings to earthquake motion was analysed for the purpose of the hazard and risk assessment. The soil-structure interaction models prepared for the index buildings used in the derivation of fragility functions were used in hazard and risk assessment. The foundation of the buildings is important in the transfer of the ground motion into the buildings. For a selection of index buildings with shallow foundations as wells as buildings with pile foundations soil-structure interaction was evaluated.<br>The B-stations accelerometers of the KNMI seismic monitoring network are housed in buildings. In this report the potential impact of the soil structure interaction resulting from these buildings on the records from these stations is investigated. | | |
| **Directliy linked research** | (1) Shake table tests<br>(2) Fragility curves for building typologies (URM)<br>(3) Shallow geology and soil<br>(4) Risk Assessment | | |
| **Used data** | Experiments | | |
| **Associated organisation** | NAM | | |
| **Assurance** | MOZAYK | | |

# D16

## DELIVERABLE

### Project Information

| | |
|---|---|
| Project Title: | **Modelling of URM buildings in support of damage fragility functions derivation** |
| Project Start: | February 2017 |
| Technical Point of Contact: | Rui Pinho |
| Administrative Point of Contact: | Roberto Nascimbene |

### Deliverable Information

| | |
|---|---|
| Deliverable Title: | **Soil-structure-interaction analysis in support of Groningen B-stations verification efforts** |
| Data of Issue: | 30th April 2020 |
| Authors: | Francesco Cavalieri, António A. Correia |
| Reviewer: | Rui Pinho |

REVISION: **18 October 2020**

# Table of Contents

# 1 Introduction

In order to develop ground motion models that are then employed in seismic hazard and risk analyses, use is typically made of free-field recordings, i.e. ground motion time-histories that are free from Soil-Structure-Interaction (SSI) effects that could be potentially introduced by the structures, and their corresponding foundations, in which the recording instrument (accelerograph, geophone, seismometer) is installed. As discussed in Stewart (2000), which summarises past investigations on the issue of selection of recordings for the development of free-field ground motion models, it is typically considered that recordings obtained from instruments installed inside a building can be considered as representative of free-field conditions if the latter is less than 2-3 stories high and does not feature a basement or a massive foundation system.

Naturally, the small buildings that host the recording stations should not be in the vicinity of topographic features such as slopes, cliffs, ridges, etc., nor should the instrument be mounted on pedestals or plinths, which, as shown by e.g. Luco et al. (1990) and Hollender et al. (2020), may affect the high-frequency content of ground motion recordings. On the other hand, as noted by e.g. Bycroft (1978), large foundation rafts or embedded structures may give rise to ground motion attenuation in locations with soil characterised by low values of shear wave velocity.

In the Groningen region (northern Netherlands), subjected to induced seismicity earthquakes, a network of accelerometers located mainly inside sheds and barns, identified as B-network and managed by the Royal Netherlands Meteorological Institute (KNMI), has been in operation for several years (Dost et al., 2017; Ntinalexis et al., 2019). A recent report by Witteveen+Bos (2019) alluded to the possibility that soil-structure-interaction (SSI) could be affecting recordings from the aforementioned B-stations, based on the fact that comparisons with recordings from a more recent network of free-field instruments (G-network) seemed to indicate an apparent tendency for lower high-frequency spectral ordinates in B-network recordings (the locations of the "pairs" of B- and G-stations are indicated in Figure 1.1, whilst response spectra comparisons for recordings from three exemplificative cases are shown in Figure 1.2), even if, as reported in Ntinalexis et al. (2019), both networks use the same equipment and processing strategies.

It is noted that the fact that differences were observed in accelerograms recorded in stations that are several hundreds of metres apart (the distance between compared B-network and G-network stations varied between 0.5 and 2.3 km) is obviously not a surprise, for reasons of both spatial incoherence (Abrahamson et al., 1991), as well as the non-negligible soil profile variations observed in the Groningen region (Kruiver et al., 2017; Rodriguez-Marek et al., 2017). In their work on the development of a spatial correlation model for the Groningen field, Stafford et al. (2019) showed that one could indeed expect very significant differences in observed motions over the distances that typically separate the "pairs" of G- and B-stations considered by Witteveen+Bos (2019). By contrast, in the study on recordings from instruments installed on buildings by Stewart (2000), the considered 46 pairs of recordings featured a separation distance not greater than 0.5 km (the mean distance was 150 m, whilst the median was 122 m).

However, whilst finding variations when comparing recordings from stations so distant apart would be normal and anticipated, one would also expect such variations to be of a relatively random nature, with no particular trend being observed (given that source-to-site distances are essentially identical). Instead, Witteveen+Bos (2019) noticed a relatively systematic attenuation of high-frequency spectral ordinates, which is one of the potential effects that SSI has been seen to cause (e.g. Abrahamson et al., 1991). Such possible SSI interference in ground-motion recordings could certainly be present in three of the 15 B-stations in operation at the time of this study, given that they feature instruments placed in the basement of buildings, one of which being also particularly large in size, hence very likely to generate the so-called kinematic interaction effects, related to base-slab averaging and embedment effects (see e.g. Stewart, 2000). However, the remaining 12 recording stations are installed at the ground level inside sheds and barns, which

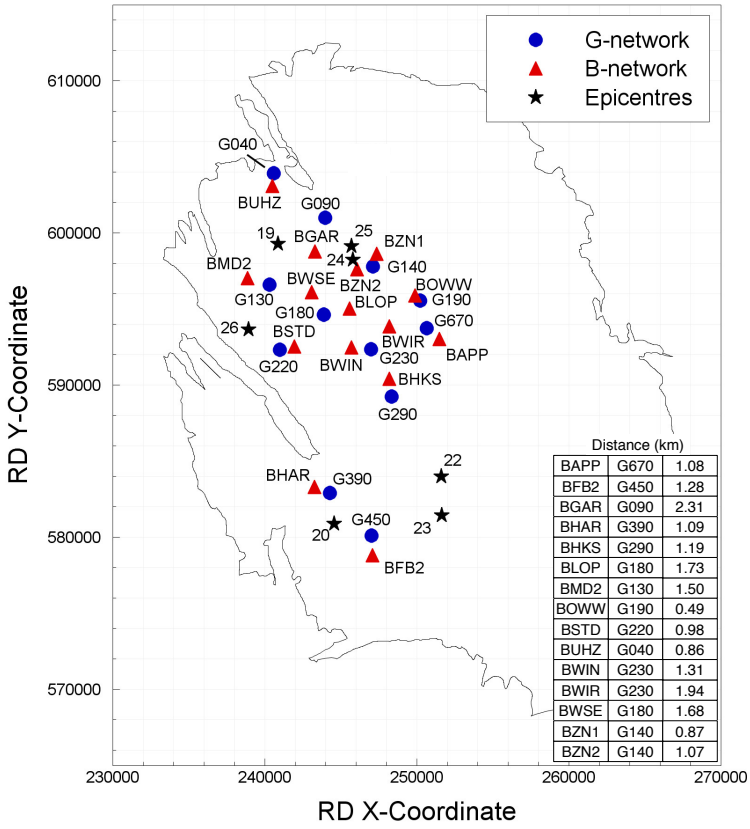


| | | |
|---|---|---|
| BAPP | G670 | 1.08 |
| BFB2 | G450 | 1.28 |
| BGAR | G090 | 2.31 |
| BHAR | G390 | 1.09 |
| BHKS | G290 | 1.19 |
| BLOP | G180 | 1.73 |
| BMD2 | G130 | 1.50 |
| BOWW | G190 | 0.49 |
| BSTD | G220 | 0.98 |
| BUHZ | G040 | 0.86 |
| BWIN | G230 | 1.31 |
| BWIR | G230 | 1.94 |
| BWSE | G180 | 1.68 |
| BZN1 | G140 | 0.87 |
| BZN2 | G140 | 1.07 |

**Figure 1.1 Locations of the 15 "pairs" of B- and G-stations and of the epicentres of the events that generated the recordings used in the comparisons (adapted from Ntinalexis et al., 2019).**

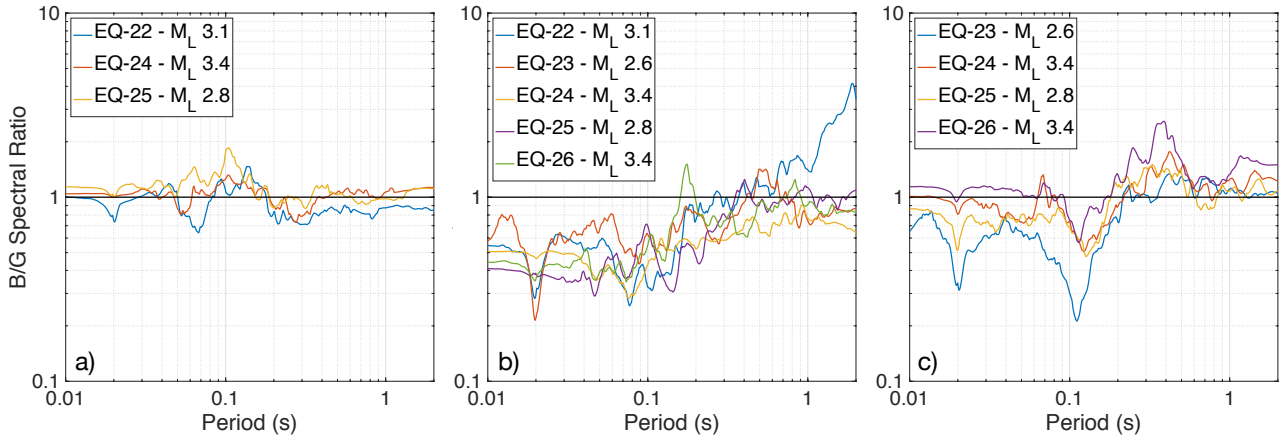


**Figure 1.2 Ratios of response spectra ordinates from three different pairs of B- and G-stations: a) G190 and BOWW (lightweight shed structure); b) G040 and BUHZ (heavy basement building), c) G670 and BAPP (lightweight shed structure) (adapted from Ntinalexis et al., 2019).**

consist of very light structures resting on strip or mat foundations with limited soil embedment (typically around 60 cm or less), small foundation element thickness, and with relatively small dimensions in plan, hence very unlikely to give rise to SSI effects. It is noted that even base-slab averaging effects due to wave passage and lagged coherency are not expected to be relevant in these 12 stations due to both their small dimensions in plan and the soft nature of the soils considered (existing studies do not even include structures with these dimensions and foundation soil shear wave velocities in their scope of application; e.g. NIST, 2012).

In order to numerically investigate the possible reasons behind the apparent bias between foundation-level and free-field recordings in the Groningen field, the use of a finite element soil-block model was adopted. This solution allows for the implementation of a direct one-step approach (i.e. without the need for substructuring/simplified SSI modelling approaches, such as those used e.g. in Cavalieri et al., 2020), which is the most refined option to account for SSI, since it is able to account simultaneously for inertial and kinematic interaction, as well as to also handle soil nonlinearities. With the aim to also overcome the limitations of the works using soil-blocks and currently available in the literature, a 3D nonlinear soil-block model representing a layered soil was used to carry out a numerical study involving a number of finite element analyses, with a view to first assess if recordings from instruments located in lightweight structures (like sheds or barns) may or may not be affected by SSI effects. Then, having not observed the latter, an attempt was made to identify an alternative explanation for the apparent trend for lower high-frequency spectral ordinates noticed in recordings from B-stations.

As described in Section 2, six soil profiles were considered in this study. The first set of three soil profiles correspond to the sites where two B-stations hosted inside shallow lightweight structures (BOWW and BAPP) and one B-station installed in the basement of a large heavy building (BUHZ) are located. The second set of three soil profiles correspond instead to three sites where G-stations (G040, G180 and G390) are located, and for which soil properties data was available; it is noted that at the time this numerical study was initiated, availability of geotechnical characterisation data for G-station locations was still limited. Notwithstanding the latter, a soil profile for one of the G-stations (G040) considered in the report by Witteveen+Bos (2019) could be obtained, which was useful for some of the analyses presented subsequently in this work (in particular those discussed in Section 6.4). Two case-study structures were modelled together with the soil-block in OpenSees (McKenna et al., 2000): a shed and a building with basement, both of which are described in Section 3.1. For what concerns instead the seismic input, 50 m deep recordings from the field (the G-stations feature instruments placed in boreholes at depths of 0, 50, 100, 150 and 200 m) were considered (see Section 3.2). The modelling approach adopted for both soil and structures, as well as the definition of the input at its base, are discussed in Sections 4 and 5. The appropriateness of the finite element model is then checked (Section 6) and employed to conduct the numerical investigations introduced above. Results are given in Section 0, whilst final discussion and conclusions can be found in Section 8.

# 2 Soil properties

From the Groningen microzonation studies by Kruiver et al. (2017) and Rodriguez-Marek et al. (2017), to which interested readers are referred to for details not included herein, it was possible to gain access not only to shear wave velocity ($V_S$) profiles and soil stratigraphy information, but also to a set of geomechanical parameters used to describe the dynamic soil behaviour in terms of the shear modulus reduction and damping curves.

For clay, the aforementioned parameters are the overconsolidation ratio (OCR), the plasticity index (IP) and the total unit weight, which allows one to define shear modulus reduction and damping curves in accordance with Darendeli (2001) relationships.

For sand, the parameters are instead the median grain size ($D_{50}$), the coefficient of uniformity ($C_u$) and the total unit weight, which permits the definition of shear modulus reduction and damping curves through the use of Menq (2003) relationships.

As already mentioned, in this study six different soil profiles were considered, corresponding to recording stations BOWW, BAPP, BUHZ, G040, G180 and G390. Their main stratigraphy and geotechnical properties are given in the sub-Sections below, where their shear wave velocity profiles are also included. To allow making a comparison, the six $V_S$ profiles are displayed in Figure 2.1, together with indication of their average $V_S$ over the top 30 metres, $V_{S,30}$.

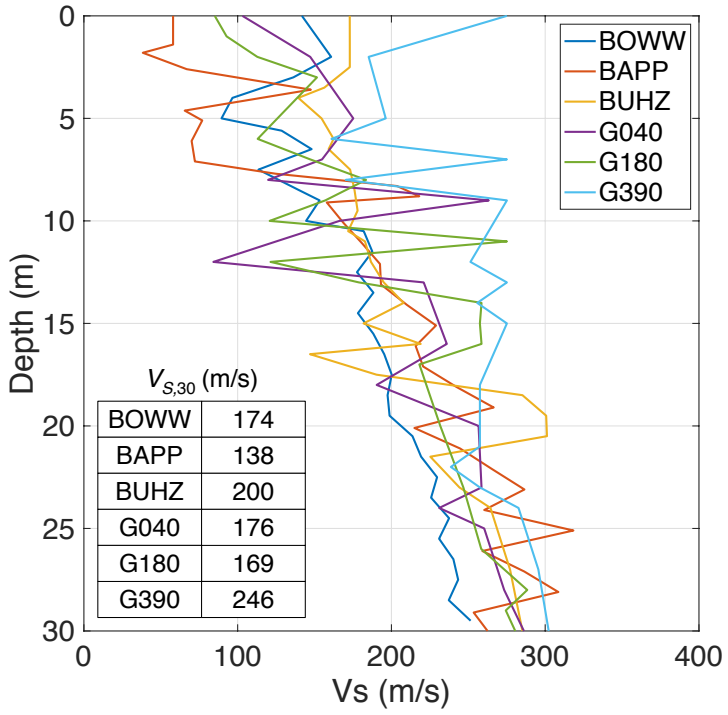


**Figure 2.1 Shear wave velocity profiles and $V_{S,30}$ values for the six considered soil profiles.**

## 2.1 BOWW

Table 2.1 shows the stratigraphy and the available geotechnical parameters within about 30 m for the BOWW soil profile, whereas Figure 2.2 shows the corresponding shear wave velocity profile.

**Table 2.1: Stratigraphy and geotechnical parameters within 30m depth for BOWW soil profile.**

| Depth (m) | Thickness (m) | Lithology | $V_S$ (m/s) | Unit Weight (kN/m$^3$) | PI (-) | OCR (-) | $C_u$ (-) | $D_{50}$ (mm) | $k_0$ (-) | $S_u$ (kPa) |
|---|---|---|---|---|---|---|---|---|---|---|
| 0 | 2 | Fine Sand | 141.8 | 18.4 | 0 | 1.0 | 5.53 | 0.08 | 0.5 | - |
| 2 | 1 | Clay Sand And Sandy Clay | 160.8 | 16.2 | 30 | 2.0 | - | - | 0.5 | 58.8 |
| 3 | 1 | | 136.2 | 16.2 | 30 | 2.0 | - | - | 0.5 | 61.9 |
| 4 | 1 | Clay | 96.6 | 12.9 | 30 | 2.0 | - | - | 0.5 | 22.8 |
| 5 | 0.6 | Peat | 89.5 | 10.8 | - | 2.0 | - | - | 0.35 | 24.8 |
| 5.6 | 0.9 | Clay | 128.6 | 12.9 | 30 | 2.0 | - | - | 0.5 | 23.9 |
| 6.5 | 1 | | 148.1 | 12.9 | 30 | 2.0 | - | - | 0.5 | 24.8 |
| 7.5 | 1 | | 113.5 | 12.9 | 30 | 2.0 | - | - | 0.5 | 25.8 |
| 8.5 | 0.5 | | 139.9 | 12.9 | 30 | 2.0 | - | - | 0.5 | 26.5 |
| 9 | 1 | | 153.3 | 12.9 | 30 | 2.0 | - | - | 0.5 | 27.2 |
| 10 | 0.5 | | 144.5 | 12.9 | 30 | 2.0 | - | - | 0.5 | 27.9 |
| 10.5 | 1 | Fine Sand | 182.0 | 19.4 | 0 | 1.0 | 2.34 | 0.12 | 1 | - |
| 11.5 | 1 | Clay Sand And Sandy Clay | 187.6 | 16.7 | 10 | 4.9 | - | - | 1.2 | 99.5 |
| 12.5 | 1 | | 177.6 | 16.7 | 10 | 4.9 | - | - | 1.2 | 106.2 |
| 13.5 | 1 | | 188.3 | 16.7 | 10 | 4.9 | - | - | 1.2 | 112.8 |
| 14.5 | 1 | | 178.2 | 16.7 | 10 | 5.0 | - | - | 1.2 | 119.5 |
| 15.5 | 1 | | 188.2 | 16.7 | 10 | 5.0 | - | - | 1.2 | 126.2 |
| 16.5 | 1 | | 195.3 | 16.7 | 10 | 5.0 | - | - | 1.2 | 132.9 |
| 17.5 | 1 | | 200.2 | 16.7 | 10 | 5.1 | - | - | 1.2 | 139.6 |
| 18.5 | 1 | Clay | 197.5 | 17.6 | 50 | 5.4 | - | - | 1.1 | 131.9 |
| 19.5 | 1 | | 198.8 | 17.6 | 50 | 5.4 | - | - | 1.1 | 138.7 |
| 20.5 | 1 | | 213.7 | 17.6 | 50 | 5.3 | - | - | 1.1 | 145.6 |
| 21.5 | 1 | | 219.3 | 17.6 | 50 | 5.3 | - | - | 1.1 | 152.4 |
| 22.5 | 1 | | 229.7 | 17.6 | 50 | 5.2 | - | - | 1.1 | 159.3 |
| 23.5 | 1 | | 225.8 | 17.6 | 50 | 5.2 | - | - | 1.1 | 166.1 |
| 24.5 | 1 | | 237.5 | 17.6 | 50 | 5.2 | - | - | 1.1 | 173.0 |
| 25.5 | 1 | | 231.0 | 17.6 | 50 | 5.1 | - | - | 1.1 | 179.9 |
| 26.5 | 1 | | 240.3 | 17.6 | 50 | 5.1 | - | - | 1.1 | 186.7 |
| 27.5 | 1 | | 243.4 | 17.6 | 50 | 5.0 | - | - | 1.1 | 193.6 |
| 28.5 | 1 | | 237.3 | 17.6 | 50 | 5.0 | - | - | 1.1 | 200.4 |
| 29.5 | 1.5 | | 251.5 | 17.6 | 50 | 5.0 | - | - | 1.1 | 209.0 |

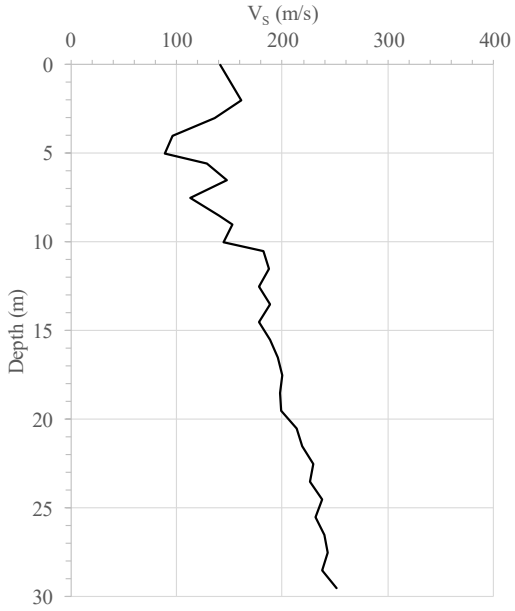


**Figure 2.2 Shear wave velocity profile for the BOWW soil profile.**

## 2.2 BAPP

Table 2.2 shows the stratigraphy and the available geotechnical parameters within about 30 m for the BAPP soil profile, whereas Figure 2.3 shows the corresponding shear wave velocity profile.

**Table 2.2: Stratigraphy and geotechnical parameters within 30m depth for BAPP soil profile.**

| Depth (m) | Thickness (m) | Lithology | $V_S$ (m/s) | Unit Weight (kN/m$^3$) | PI (-) | OCR (-) | $C_u$ (-) | $D_{50}$ (mm) | $k_0$ (-) | $S_u$ (kPa) |
|---|---|---|---|---|---|---|---|---|---|---|
| 0 | 1.4 | Clay | 58.0 | 12.9 | 30 | 2.0 | - | - | 0.5 | 12.8 |
| 1.4 | 0.4 | | 58.0 | 12.9 | 30 | 2.0 | - | - | 0.5 | 14.6 |
| 1.8 | 0.8 | Peat | 38.3 | 10.8 | - | 2.0 | - | - | 0.35 | 14.1 |
| 2.6 | 1 | Clay | 66.9 | 12.9 | 30 | 2.0 | - | - | 0.5 | 15.5 |
| 3.6 | 1.02 | | 147.6 | 12.9 | 30 | 2.0 | - | - | 0.5 | 16.5 |
| 4.62 | 0.48 | Peat | 65.6 | 11.3 | - | 2.0 | - | - | 0.7 | 15.7 |
| 5.1 | 1 | Peat | 77.0 | 11.3 | - | 2.0 | - | - | 0.7 | 16.2 |
| 6.1 | 1 | Peat | 70.1 | 11.3 | - | 2.0 | - | - | 0.7 | 16.9 |
| 7.1 | 0.6 | Fine Sand | 72.2 | 19.4 | 0 | 1.0 | 2.34 | 0.12 | 1 | - |
| 7.7 | 0.6 | Clay Sand And Sandy Clay | 124.8 | 16.9 | 50 | 4.7 | - | - | 1.1 | 63.0 |
| 8.3 | 0.5 | Fine Sand | 203.7 | 19.4 | 0 | 1.0 | 2.34 | 0.12 | 1 | - |
| 8.8 | 0.3 | Clay | 218.1 | 17.6 | 50 | 5.8 | - | - | 1.1 | 63.0 |
| 9.1 | 1 | | 158.0 | 17.6 | 50 | 5.8 | - | - | 1.1 | 67.5 |
| 10.1 | 1 | | 168.9 | 17.6 | 50 | 5.7 | - | - | 1.1 | 74.3 |
| 11.1 | 1 | | 181.0 | 17.6 | 50 | 5.7 | - | - | 1.1 | 81.2 |
| 12.1 | 1 | | 192.6 | 17.6 | 50 | 5.6 | - | - | 1.1 | 88.0 |
| 13.1 | 1 | | 193.2 | 17.6 | 50 | 5.6 | - | - | 1.1 | 94.9 |
| 14.1 | 1 | | 210.2 | 17.6 | 50 | 5.6 | - | - | 1.1 | 101.8 |
| 15.1 | 1 | | 229.0 | 17.6 | 50 | 5.5 | - | - | 1.1 | 108.6 |
| 16.1 | 1 | | 215.8 | 17.6 | 50 | 5.5 | - | - | 1.1 | 115.5 |
| 17.1 | 1 | | 220.6 | 17.6 | 50 | 5.5 | - | - | 1.1 | 122.3 |
| 18.1 | 1 | | 242.4 | 17.6 | 50 | 5.4 | - | - | 1.1 | 129.2 |
| 19.1 | 1 | | 266.5 | 17.6 | 50 | 5.4 | - | - | 1.1 | 136.0 |
| 20.1 | 1 | | 215.0 | 17.6 | 50 | 5.3 | - | - | 1.1 | 142.9 |
| 21.1 | 1 | | 244.7 | 17.6 | 50 | 5.3 | - | - | 1.1 | 149.7 |
| 22.1 | 1 | | 265.4 | 17.6 | 50 | 5.3 | - | - | 1.1 | 156.6 |
| 23.1 | 1 | | 286.5 | 17.6 | 50 | 5.2 | - | - | 1.1 | 163.5 |
| 24.1 | 1 | | 260.4 | 17.6 | 50 | 5.2 | - | - | 1.1 | 170.3 |
| 25.1 | 1 | | 318.3 | 17.6 | 50 | 5.1 | - | - | 1.1 | 177.2 |
| 26.1 | 1 | | 259.1 | 17.6 | 50 | 5.1 | - | - | 1.1 | 184.0 |
| 27.1 | 1 | | 286.4 | 17.6 | 50 | 5.1 | - | - | 1.1 | 190.9 |
| 28.1 | 1 | | 308.6 | 17.6 | 50 | 5.0 | - | - | 1.1 | 197.7 |
| 29.1 | 0.9 | | 253.5 | 17.6 | 50 | 5.0 | - | - | 1.1 | 204.2 |
| 30 | 3 | | 262.5 | 17.6 | 50 | 4.9 | - | - | 1.1 | 217.6 |

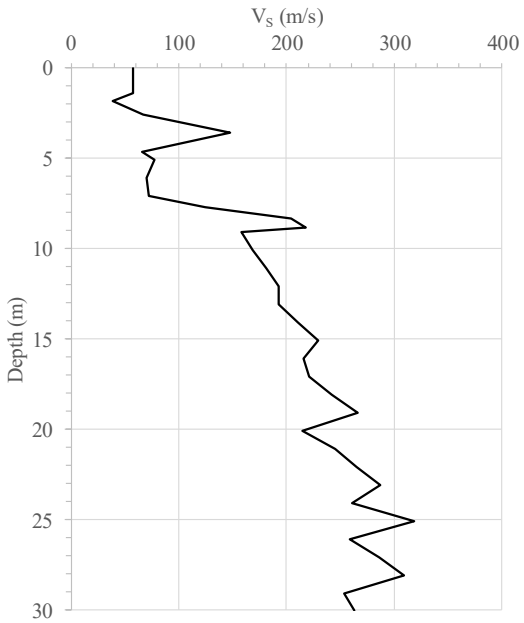


**Figure 2.3 Shear wave velocity profile for the BAPP soil profile.**

## 2.3 BUHZ

Table 2.3 shows the stratigraphy and the available geotechnical parameters within about 30 m for the BUHZ soil profile, whereas Figure 2.4 shows the corresponding shear wave velocity profile.

**Table 2.3: Stratigraphy and geotechnical parameters within 30m depth for BUHZ soil profile.**

| Depth (m) | Thickness (m) | Lithology | $V_S$ (m/s) | Unit Weight (kN/m$^3$) | PI (-) | OCR (-) | $C_u$ (-) | $D_{50}$ (mm) | $k_0$ (-) | $S_u$ (kPa) |
|---|---|---|---|---|---|---|---|---|---|---|
| 0 | 1.5 | Fine Sand | 172.9 | 18.8 | 0 | 1.0 | 2.03 | 0.11 | 0.5 | - |
| 1.5 | 1 | | 172.9 | 18.8 | 0 | 1.0 | 2.03 | 0.11 | 0.5 | - |
| 2.5 | 1 | | 172.9 | 18.8 | 0 | 1.0 | 2.03 | 0.11 | 0.5 | - |
| 3.5 | 0.5 | | 156.4 | 18.8 | 0 | 1.0 | 2.03 | 0.11 | 0.5 | - |
| 4 | 1 | Clay Sand And Sandy Clay | 139.5 | 16.2 | 30 | 2.0 | - | - | 0.5 | 68.0 |
| 5 | 1 | | 154.6 | 16.2 | 30 | 2.0 | - | - | 0.5 | 71.1 |
| 6 | 0.5 | | 162.4 | 16.2 | 30 | 2.0 | - | - | 0.5 | 73.5 |
| 6.5 | 1 | Fine Sand | 159.2 | 18.8 | 0 | 1.0 | 2.03 | 0.11 | 0.5 | - |
| 7.5 | 1 | | 173.2 | 18.8 | 0 | 1.0 | 2.03 | 0.11 | 0.5 | - |
| 8.5 | 1 | | 176.0 | 18.8 | 0 | 1.0 | 2.03 | 0.11 | 0.5 | - |
| 9.5 | 1 | Clay Sand And Sandy Clay | 178.0 | 16.2 | 30 | 2.0 | - | - | 0.5 | 89.0 |
| 10.5 | 0.5 | | 171.9 | 16.2 | 30 | 2.0 | - | - | 0.5 | 91.4 |
| 11 | 1 | | 182.8 | 16.2 | 30 | 2.0 | - | - | 0.5 | 93.7 |
| 12 | 1 | | 186.7 | 16.2 | 30 | 2.0 | - | - | 0.5 | 96.9 |
| 13 | 1 | | 195.0 | 16.2 | 30 | 2.0 | - | - | 0.5 | 100.0 |
| 14 | 1 | | 208.0 | 16.2 | 30 | 2.0 | - | - | 0.5 | 103.1 |
| 15 | 1 | | 181.9 | 16.2 | 30 | 2.0 | - | - | 0.5 | 106.3 |
| 16 | 0.5 | Fine Sand | 219.1 | 18.8 | 0 | 1.0 | 2.03 | 0.11 | 0.5 | - |
| 16.5 | 1 | Peat | 147.1 | 11.3 | - | 2.0 | - | - | 0.7 | 68.7 |
| 17.5 | 1 | Fine Sand | 190.3 | 19.4 | 0 | 1.0 | 1.76 | 0.11 | 1 | - |
| 18.5 | 1 | | 285.2 | 19.4 | 0 | 1.0 | 1.76 | 0.11 | 1 | - |
| 19.5 | 1 | | 300.7 | 19.4 | 0 | 1.0 | 1.76 | 0.11 | 1 | - |
| 20.5 | 1 | | 301.2 | 19.4 | 0 | 1.0 | 1.76 | 0.11 | 1 | - |
| 21.5 | 1.5 | | 225.3 | 19.4 | 0 | 1.0 | 1.76 | 0.11 | 1 | - |
| 23 | 1 | Clay Sand And Sandy Clay | 244.2 | 17.6 | 30 | 4.0 | - | - | 1.4 | 170.7 |
| 24 | 3 | | 264.4 | 18.1 | 30 | 5.0 | - | - | 1.2 | 180.5 |
| 27 | 3 | | 277.1 | 18.1 | 30 | 4.8 | - | - | 1.2 | 195.4 |
| 30 | 1 | | 285.2 | 18.1 | 30 | 4.7 | - | - | 1.2 | 205.4 |

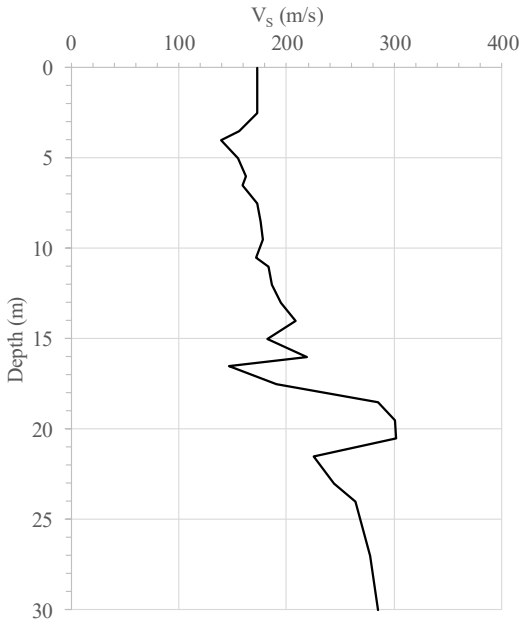


**Figure 2.4 Shear wave velocity profile for the BUHZ soil profile.**

## 2.4 G040

Table 2.4 shows the stratigraphy and the available geotechnical parameters within about 30 m for the G040 soil profile, whereas Figure 2.5 shows the corresponding shear wave velocity profile.

**Table 2.4: Stratigraphy and geotechnical parameters within 30m depth for G040 soil profile.**

| Depth (m) | Thickness (m) | Lithology | $V_S$ (m/s) | Unit Weight (kN/m$^3$) | PI (-) | OCR (-) | $C_u$ (-) | $D_{50}$ (mm) | $k_0$ (-) | $S_u$ (kPa) |
|---|---|---|---|---|---|---|---|---|---|---|
| 0 | 2 | Clay Sand And Sandy Clay | 103.1 | 16.2 | 30 | 2.0 | - | - | 0.5 | 51.9 |
| 2 | 3 | Fine Sand | 147.2 | 18.8 | 0 | 1.0 | 2.03 | 0.11 | 0.5 | - |
| 5 | 2 | | 175.2 | 18.8 | 0 | 1.0 | 2.03 | 0.11 | 0.5 | - |
| 7 | 1 | Clay Sand And Sandy Clay | 154.9 | 16.2 | 30 | 2.0 | - | - | 0.5 | 78.7 |
| 8 | 1 | Clay | 119.8 | 12.9 | 30 | 2.0 | - | - | 0.5 | 33.4 |
| 9 | 1 | Coarser sand, gravel, shells | 263.3 | 21 | 0 | 1.0 | 1.74 | 0.31 | 0.5 | - |
| 10 | 1 | Clay Sand And Sandy Clay | 166.2 | 16.2 | 30 | 2.0 | - | - | 0.5 | 88.8 |
| 11 | 1 | Clay | 125.1 | 12.9 | 30 | 2.0 | - | - | 0.5 | 39.8 |
| 12 | 1 | Peat | 84.2 | 10.3 | - | 2.0 | - | - | 0.35 | 46.2 |
| 13 | 3 | Fine Sand | 221.0 | 18.8 | 0 | 1.0 | 2.03 | 0.11 | 0.5 | - |
| 16 | 2 | | 236.0 | 18.8 | 0 | 1.0 | 2.03 | 0.11 | 0.5 | - |
| 18 | 2 | Clay Sand And Sandy Clay | 190.4 | 16.2 | 30 | 2.0 | - | - | 0.5 | 117.3 |
| 20 | 3 | Fine Sand | 256.7 | 18.8 | 0 | 1.0 | 2.03 | 0.11 | 0.5 | - |
| 23 | 1 | Clay Sand And Sandy Clay | 258.6 | 17.2 | 40 | 5.4 | - | - | 1.3 | 211.0 |
| 24 | 1 | Clay | 231.1 | 14.4 | 40 | 5.5 | - | - | 1.1 | 221.4 |
| 25 | 3 | Clay Sand And Sandy Clay | 260.3 | 18.1 | 30 | 5.0 | - | - | 1.2 | 179.4 |
| 28 | 3 | | 273.3 | 18.1 | 30 | 4.8 | - | - | 1.2 | 194.3 |
| 31 | 1 | Fine Sand | 292.6 | 19.6 | 0 | 1.0 | 1.84 | 0.12 | 1 | - |

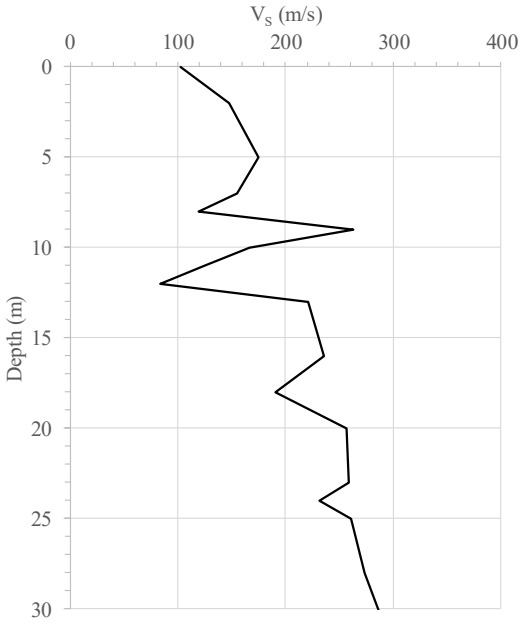


**Figure 2.5 Shear wave velocity profile for the G040 soil profile.**

## 2.5 G180

Table 2.5 shows the stratigraphy and the available geotechnical parameters within about 30 m for the G180 soil profile, whereas Figure 2.6 shows the corresponding shear wave velocity profile.

**Table 2.5: Stratigraphy and geotechnical parameters within 30m depth for G180 soil profile.**

| Depth (m) | Thickness (m) | Lithology | $V_S$ (m/s) | Unit Weight (kN/m$^3$) | PI (-) | OCR (-) | $C_u$ (-) | $D_{50}$ (mm) | $k_0$ (-) | $S_u$ (kPa) |
|---|---|---|---|---|---|---|---|---|---|---|
| 0 | 1 | Clay Sand And Sandy Clay | 85.1 | 16.2 | 30 | 2.0 | - | - | 0.5 | 48.0 |
| 1 | 1 | Clay | 92.8 | 12.9 | 30 | 2.0 | - | - | 0.5 | 15.5 |
| 2 | 1 | Clay Sand And Sandy Clay | 112.8 | 16.2 | 30 | 2.0 | - | - | 0.5 | 55.0 |
| 3 | 3 | Fine Sand | 151.6 | 18.8 | 0 | 1.0 | 2.03 | 0.11 | 0.5 | - |
| 6 | 1 | Clay | 113.0 | 12.9 | 30 | 2.0 | - | - | 0.5 | 26.8 |
| 7 | 1 | Clay Sand And Sandy Clay | 147.2 | 16.2 | 30 | 2.0 | - | - | 0.5 | 72.9 |
| 8 | 1 | Fine Sand | 183.5 | 18.8 | 0 | 1.0 | 2.03 | 0.11 | 0.5 | - |
| 9 | 1 | Clay Sand And Sandy Clay | 157.0 | 16.2 | 30 | 2.0 | - | - | 0.5 | 80.4 |
| 10 | 1 | Clay | 120.8 | 12.9 | 30 | 2.0 | - | - | 0.5 | 34.5 |
| 11 | 1 | Moderate Coarse Sand | 275.1 | 21 | 0 | 1.0 | 2.23 | 0.19 | 1 | - |
| 12 | 1 | Peat | 121.4 | 11.4 | - | 5.0 | - | - | 1.1 | 48.5 |
| 13 | 1 | Clay | 178.8 | 14.4 | 50 | 5.0 | - | - | 1.1 | 110.0 |
| 14 | 1 | Clay Sand And Sandy Clay | 258.6 | 17.2 | 40 | 5.0 | - | - | 1.3 | 128.6 |
| 15 | 1 | Fine Sand | 257.5 | 19.4 | 0 | 1.0 | 1.76 | 0.11 | 1 | - |
| 16 | 1 | Clay Sand And Sandy Clay | 258.6 | 17.2 | 40 | 5.1 | - | - | 1.3 | 145.1 |
| 17 | 3 | Clay | 218.2 | 17.6 | 50 | 5.3 | - | - | 1.1 | 143.9 |
| 20 | 3 | Clay Sand And Sandy Clay | 231.8 | 18.1 | 30 | 5.2 | - | - | 1.2 | 149.9 |
| 23 | 3 | | 246.8 | 18.1 | 30 | 5.1 | - | - | 1.2 | 164.8 |
| 26 | 2 | | 258.4 | 18.1 | 30 | 5.0 | - | - | 1.2 | 177.2 |
| 28 | 1 | Fine Sand | 288.3 | 19.6 | 0 | 1.0 | 1.84 | 0.12 | 1 | - |
| 29 | 3 | Clay Sand And Sandy Clay | 274.4 | 18.1 | 30 | 4.8 | - | - | 1.2 | 195.6 |
| 32 | 1 | Fine Sand | 292.8 | 19.6 | 0 | 1.0 | 1.84 | 0.12 | 1 | - |

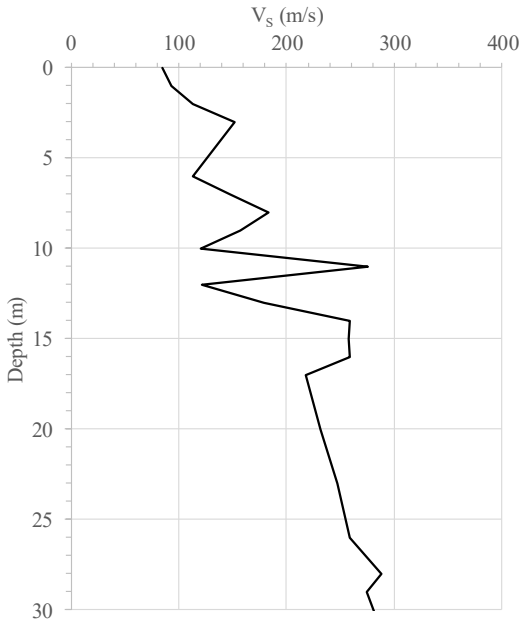


**Figure 2.6 Shear wave velocity profile for the G180 soil profile.**

## 2.6 G390

Table 2.6 shows the stratigraphy and the available geotechnical parameters within about 30 m for the G390 soil profile, whereas Figure 2.7 shows the corresponding shear wave velocity profile.

**Table 2.6: Stratigraphy and geotechnical parameters within 30m depth for G390 soil profile.**

| Depth (m) | Thickness (m) | Lithology | $V_S$ (m/s) | Unit Weight (kN/m$^3$) | PI (-) | OCR (-) | $C_u$ (-) | $D_{50}$ (mm) | $k_0$ (-) | $S_u$ (kPa) |
|---|---|---|---|---|---|---|---|---|---|---|
| 0 | 2 | Moderate Coarse Sand | 275.1 | 21 | 0 | 1.0 | 2.44 | 0.18 | 1 | - |
| 2 | 3 | Clay Sand And Sandy Clay | 185.2 | 16.9 | 50 | 4.7 | - | - | 1.1 | 71.5 |
| 5 | 1 | | 196.3 | 16.9 | 50 | 4.8 | - | - | 1.1 | 85.3 |
| 6 | 1 | Clay | 161.0 | 14.4 | 50 | 4.8 | - | - | 1.1 | 72.3 |
| 7 | 1 | Moderate Coarse Sand | 275.1 | 21 | 0 | 1.0 | 2.23 | 0.19 | 1 | - |
| 8 | 1 | Clay | 170.3 | 14.4 | 50 | 4.9 | - | - | 1.1 | 90.4 |
| 9 | 3 | Coarser sand, gravel, shells | 275.1 | 21 | 0 | 1.0 | 1.99 | 0.36 | 1 | - |
| 12 | 1 | Fine Sand | 251.4 | 19.4 | 0 | 1.0 | 2.34 | 0.12 | 1 | - |
| 13 | 1 | Moderate Coarse Sand | 275.1 | 21 | 0 | 1.0 | 2.23 | 0.19 | 1 | - |
| 14 | 1 | Fine Sand | 255.8 | 19.4 | 0 | 1.0 | 2.34 | 0.12 | 1 | - |
| 15 | 3 | Moderate Coarse Sand | 275.1 | 21 | 0 | 1.0 | 2.23 | 0.19 | 1 | - |
| 18 | 3 | Fine Sand | 257.5 | 19.4 | 0 | 1.0 | 1.76 | 0.11 | 1 | - |
| 21 | 1 | | 257.5 | 19.4 | 0 | 1.0 | 1.76 | 0.11 | 1 | - |
| 22 | 1 | Clay | 238.7 | 14.4 | 40 | 5.6 | - | - | 1.1 | 251.9 |
| 23 | 1 | Fine Sand | 257.5 | 19.4 | 0 | 1.0 | 1.76 | 0.11 | 1 | - |
| 24 | 3 | | 282.7 | 19.5 | 0 | 1.0 | 2.11 | 0.13 | 1 | - |
| 27 | 3 | | 295.5 | 19.6 | 0 | 1.0 | 1.84 | 0.12 | 1 | - |
| 30 | 1 | Clay Sand And Sandy Clay | 302.3 | 18.1 | 30 | 4.5 | - | - | 1.2 | 231.1 |

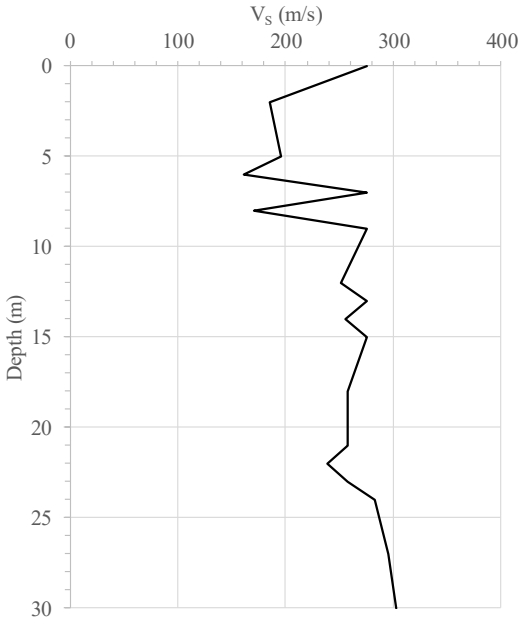


**Figure 2.7 Shear wave velocity profile for the G390 soil profile.**

# 3 Case-study buildings and seismic input

As previously mentioned, two buildings, whose main characteristics are described below, were considered, one representative of a lightweight structure with shallow foundations (which is the case for 12 of the 15 B-stations), and another in representation of a building with basement (which is the case for three B-stations).

As described in the subsequent Sections of this report, these two case-study buildings were considered in varying locations, that is, their structural models will be analysed in tandem with soil-block models featuring the different soil profiles described earlier in this report.

The range of the parametric numerical study will then be further extended by subjecting the multiple structure + soil-block models to six different ground motions (50 m deep recordings from the borehole G-stations), as described in sub-Section 3.2.

## 3.1 Case study buildings

As an example of a lightweight structure with shallow foundations, the shed structure that houses the BOWW station (Figure 3.1) was adopted in this study. It is a wooden shed, with base dimensions approximately equal to 6 x 6 $m^2$; as gathered also from Figure 3.2 (left), the walls are composed of timber columns, sheeting and bracings, while the roof substructure is made of timber beams, rafters, sheeting and roof tiles. According to Witteveen+Bos (2019), the mass of this structure can be estimated as equal to 4 t and its fundamental period of vibration as equal to 0.096 s, whilst the concrete slab foundation (Figure 3.2, right) is assumed to be 0.1 m thick.

Figure 3.1 Lightweight structure case-study.


Figure 3.2 Lightweight structure case-study: views of interior (left) and of concrete slab foundation (right).

For what regards the case of buildings with a basement, the city hall of Uithuizen (Figure 3.3), where the BUHZ station is hosted, was herein considered. The building is formed by the assembly of different structures, from varying ages and construction materials, and for this study the portion corresponding to the structural drawing shown in Figure 3.4 was adopted. It features one underground storey (approximately 2.5 m high) plus two storeys above ground (around 4 m high each), with plan dimensions of 16 x 16 $m^2$ being assumed for the purpose of this study. Floor slabs and the roof are made of timber, whilst the foundation system consists of wooden piles. The walls are in masonry.

Figure 3.3 Building with basement case-study (Arup, 2015).

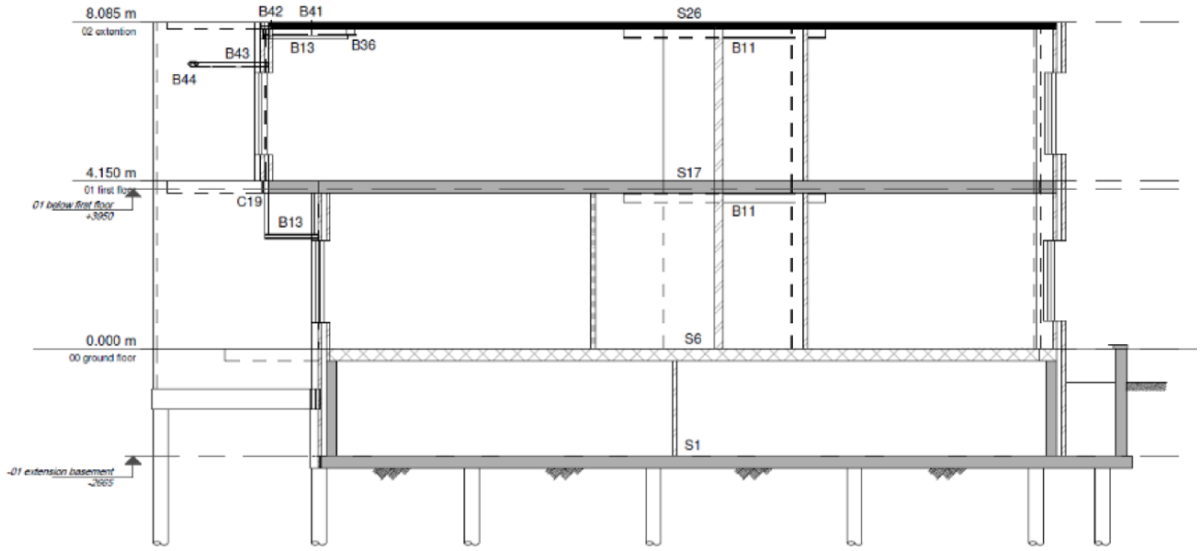


**Figure 3.4 Building with basement case-study: structural drawing (Witteveen+Bos, 2019) of portion selected for this study.**

## 3.2 Seismic input

In SSI nonlinear dynamic analyses where the soil is represented by means of a 3D soil-block numerical model, the seismic input takes the form of acceleration histories applied at the bottom of the soil-block (which in this study is 30 m deep). The subsoil in the Groningen region is constituted by a thick layer of unconsolidated deposits (over 800 m thick), which effectively implies that accelerograms recorded on "rock" are neither available nor valid as input for the soil-block model.

Typically, for such cases one would instead thus carry out deconvolution of surface recordings down to the depth of the soil-block. However, and particularly in the case of Groningen, where very soft soils (i.e. featuring very low shear wave velocity values, as well epitomised by Figure 2.3) are present and thus nonlinear soil response needs to be considered, deconvolution analyses become not only very challenging to carry out (due to difficulties in achieving convergence in such nonlinear geophysical inversion problems), but are also strongly affected by uncertainty.

Given the above difficulties and constraints, advantage was instead taken from the availability of G-station recordings at a 50 m depth, and then "transferring" these, through the convolution process described in Section 5.1 and validated in Section 6.1, to the necessary 30 m depth of the soil-block base.

Three recordings were selected, split into three categories, as follows:

- "high" intensity, with a PGA of 0.2 m/s$^2$: record 23G461;
- "medium" intensity, with a PGA of 0.02 m/s$^2$: record 24G111;
- "low" intensity, with a PGA of 0.0013 m/s$^2$: record 25G421.

Figure 3.5, left, shows the accelerograms of all six records (two horizontal components for three recordings), whereas in Figure 3.5, right, the response spectra for the six records are plotted, readily highlighting the difference in intensity of the three groups. Details on the pre-processing of these records can be found in Ntinalexis et al. (2019).

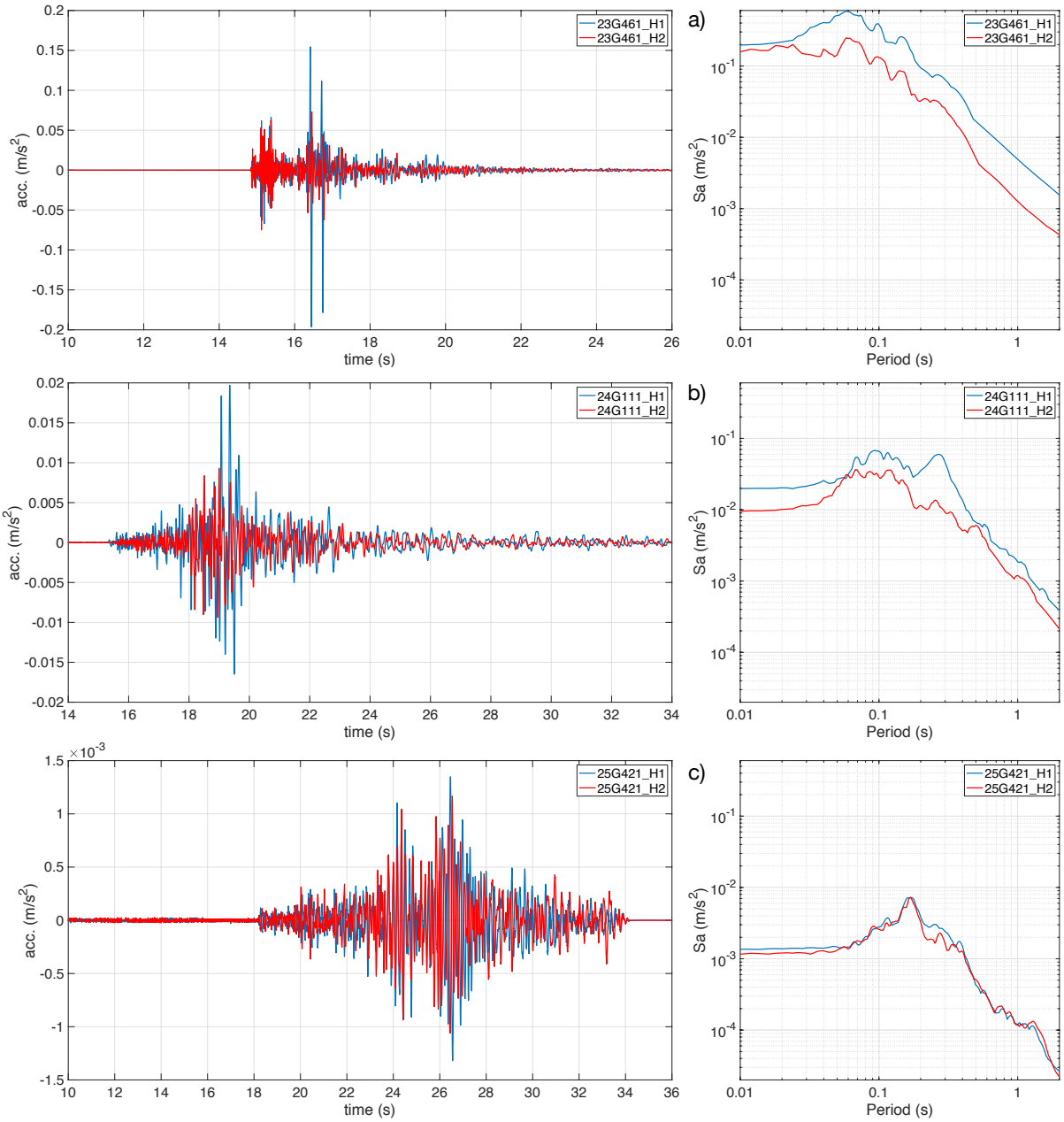


**Figure 3.5 Acceleration histories and response spectra for the two horizontal components of the three considered records: a) 23G461; b) 24G111; c) 25G421.**

For those analysis cases where it was opportune to subject the soil-block (+ structure) models to levels of ground motion intensity higher than the values recorded so far in the G-stations (see Sections 6.3 and 7.2), the adopted strategy was that of linearly amplifying record 23G461 (i.e. multiplying this record's amplitudes by a constant scalar value), given the already discussed difficulties and uncertainties associated to the deconvolution of surface recordings in soils as soft as those found in the Groningen region.

As underlined in the next sub-Section, 3D soil-block finite element analyses can be very computationally intensive, for which reason the records shown above were truncated of their initial seconds, where the values of acceleration were essentially nil. The analyses were then ran for 4 seconds only in the case of the "high" intensity record, for 6 seconds only in the case of the "medium" intensity record, and for 13 seconds in the case of the "low" intensity record, given that

such truncated durations were enough to cover the significant part of the records and corresponding soil response. A shortened duration of the analyses catered also for more immediate comparisons between acceleration history traces from different analyses (see Sections 6 and 0).

# 4 Modelling approach for soil and structures

As already discussed, the present endeavour is focussed on studying if and how the dynamic response of Groningen soil on which buildings hosting B-network stations are founded may be affected by the presence of those structures. On the contrary, understanding the details of the response of the different structural components of these buildings is outside the scope of the current work. Consequently, and with a view to limit the quite heavy computational burden of this type of 3D SSI analyses (each single run takes between two and four weeks to complete, on dedicated numerical servers), a decision was made to model only the soil-block using elements featuring the capability of capturing nonlinear response, whilst the structures would be modelled using elastic elements.

## 4.1 3D nonlinear numerical model of layered soil

A 3D numerical model of layered soil, underlain by an elastic half-space of finite rigidity that may or may not represent bedrock, was implemented in OpenSees (McKenna et al., 2000) to represent the different soil profiles described in Section 2. The soil-block model is supported vertically at the base. Periodic *equalDOF* boundary conditions, ensuring equal displacements, are applied in the two horizontal directions (global $x$ and $z$) to all nodes along the soil-block's edges, as well as to all base nodes.

The soil-block model is composed of eight-node *SSPbrick* elements using physically stabilised single-point (SSP) integration. Thanks to an enhanced assumed strain field, such elements are free from volumetric and shear locking. Linear or nonlinear materials can be assigned to soil layers. In the nonlinear case, the *PressureIndependMultiYield* material is adopted, which is an elastic-plastic material with plasticity exhibited only in the deviatoric stress-strain response, while the volumetric stress-strain response is linear elastic and independent of the deviatoric response. Being this formulation pressure-independent, the shear behaviour in monotonic or cyclic loading is insensitive to the confinement change. Real materials that can be simulated include organic soils or clay under fast (undrained) loading conditions. User-defined shear modulus degradation curves can be input, thus representing a total-stress framework.

While a pressure-dependent soil model would be able to represent more general soil behaviour phenomena, the available soil parameters for this study are not as exhaustive as required by such refined constitutive models, being limited instead to the ones used in the equivalent linear site response study by Kruiver et al. (2017) and Rodriguez-Marek et al. (2017). Therefore, it was possible to assign a shear modulus degradation curve for each soil layer, considering its initial confinement pressure, which can be fully simulated with the pressure-independent model. Moreover, it was assumed that, due to the low intensity of the motion, the volumetric threshold is not reached and thus the coupling of shear and volumetric deformations is negligible, rendering the shear modulus degradation curves a stable and reasonable soil behaviour representation.

The soil-block mesh size should be chosen in a way that allows the propagation of the shear waves below a frequency of interest, ensuring that an appropriate number of elements (typically 8 to 10) are included within the minimum wavelength, $\lambda$, of the input seismic excitation (e.g. Petridis and Pitilakis, 2018). The latter is computed as the lowest shear wave velocity of the medium divided by the highest frequency contained in the input motion. For the soil profiles at hand in this work, the average lowest $V_S$ is roughly 150 m/s; considering a frequency of interest of around 20 Hz, then the minimum wavelength $\lambda$ resulted to be 7.5 m, and using the aforementioned $\lambda/8$ ratio, a maximum mesh size of 1 m was thus chosen, which leads to a relatively dense discretisation. The discretisation along the vertical $y$-direction naturally follows the sequence of layers within the soil profile. Layers thicker than 1 m were subdivided into two or more sublayers, so that the largest sublayer thickness is 1 m. Concerning the two horizontal directions, $x$ and $z$, based on the above,

1x1 m$^2$ square elements were adopted for all soil profiles. The accuracy and efficiency of these mesh settings were checked by model validation, comparing the output results with those obtained with an alternative modelling (see Sections 5.2 and 6.1). For undrained conditions a Poisson's coefficient of 0.5 is typically assumed, but for higher numerical stability of the analyses, a value of 0.45 was adopted instead.

Due to the finite rigidity of the underlying elastic layer, the numerical model needs a compliant base, where a quiet (absorbing) boundary is used at the base of the soil-block mesh. In the developed OpenSees model, this is achieved through the use of a viscous boundary scheme consisting of two Lysmer and Kuhlemeyer (1969) dashpots attached independently at the base of the soil-block in the global *x*- and *z*-directions; the viscous dashpots of the quiet boundary absorb downward propagating waves so that they are not reflected back into the model (radiation damping). To this aim, three additional nodes were first created, one of which is fixed and the remaining two are free to move along the global *x*- and *z*-directions, respectively. The free nodes are then linked to the centroid node of the soil-block base by *equalDOF* constraints along their free directions. To define the dashpots, two *zeroLength* elements were created between the fixed node and the two free nodes defined above, and the OpenSees viscous uniaxial material was used. Following the method of Joyner and Chen (1975), the dashpot coefficient, $c_b$, is defined as the product of the mass density, $\rho_b$, and shear wave velocity, $V_{S,b}$, of the underlying elastic layer, and the soil-block base area, $A$.

$$c_b = \rho_b V_{S,b} A \tag{4.1}$$

At a quiet boundary, an acceleration history cannot be input directly, because the boundary must be able to move freely to absorb incoming waves, and thus it needs to be transformed into a stress or force history, function of the particle velocity of the upward propagating motion. For the case at hand, earthquake excitation is input to the system as two force histories, $F_x(t)$ and $F_z(t)$, in the two directions, applied at the dashpot free nodes and proportional through the dashpot constant in Equation (4.1) to the two velocity time series, $v_x(t)$ and $v_z(t)$, at the model base.

$$F_x(t) = c_b v_x(t) \tag{4.2}$$

$$F_z(t) = c_b v_z(t) \tag{4.3}$$

Given the application of seismic input along two horizontal directions and the consideration of vertical displacements of both soil-layers and structures, it should be clear from the above that the analyses carried out in the present study are fully three-dimensional. However, it is noted that the findings of this work are based on acceleration histories retrieved from the model in only one of the two horizontal directions, given the symmetric (square) properties of both soil-block and structures (for a description of the latter see Sections 4.2 and 4.3) and the similarity in intensity of the two components for all six records. As a consequence, all the time-history plots included in the remainder of the paper show acceleration responses along the same horizontal direction, namely *x*-direction (i.e. the one related to the H1 component of the records).

During application of the static gravity loads, the soil brick elements are initially limited to linear elastic response, before the activation of soil nonlinear behaviour which occurs in a second phase of the loading. Afterwards, seismic input is applied as specified above.

In Figure 4.1, below, a rendering of the soil-block model for soil profile BAPP is shown.

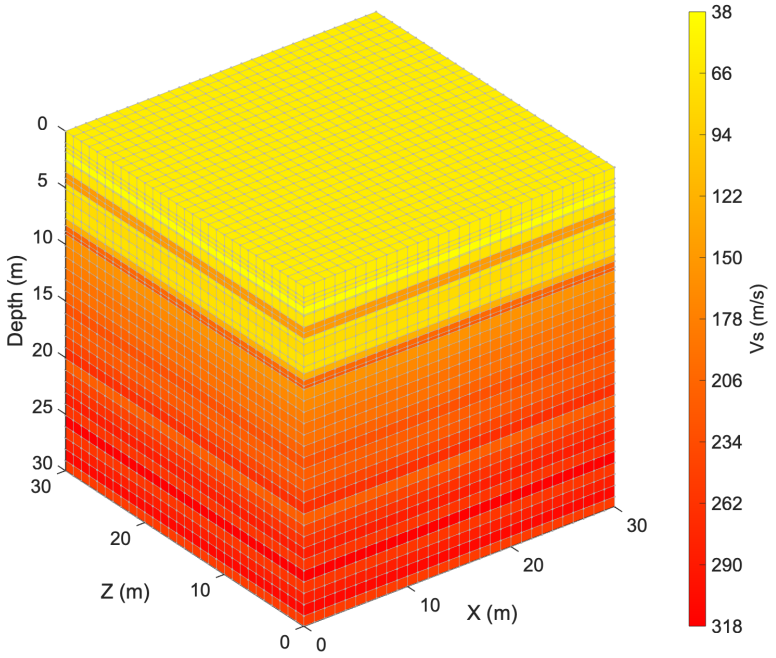


Figure 4.1 Developed soil-block model (for the BAPP soil profile).

## 4.2 3D numerical model of lightweight structure

The model for the lightweight structure described in Section 3.1 is comprised of an elastic superstructure that is fixed to an elastic square slab. The latter is modelled with the same *SSPbrick* elements used for soil, though obviously characterised by concrete material properties, and also the same discretisation used for soil elements is applied to the slab, which is thus composed of 1x1 m$^2$ square elements, 0.1 m thick. The superstructure is composed of four vertical panels (modelling the walls) and a horizontal panel (modelling the roof); the base nodes of the walls are linked to the upper nodes of the slab by *equalDOF* constraints in all three directions, and therefore the mesh for the panels follows the same horizontal discretisation used for the soil. The shell mesh spacing along the vertical direction was chosen to be half the structure's height, i.e. 1.2 m.

For all panels, shell elements of type *ShellMITC4* are employed, which use a bilinear isoparametric formulation combined with a modified shear interpolation to improve thin-plate bending performance. The shell section used within this element is of the type *ElasticMembranePlateSection*, which is an isotropic section suitable for plate and shell analysis.

In the absence of information on sectional dimensions and material mechanical properties, the thickness of the panels and their Young's modulus were set to values (see Table 4.1) that allowed matching of the total mass of the superstructure and fundamental period of vibration reported in Witteveen+Bos (2019). While the slab weight is automatically taken into account by OpenSees, through the *SSPbrick* elements, the superstructure weight must be input manually: to do so, concentrated vertical loads corresponding to the mass were applied to the upper nodes of the slab along its border.

Figure 4.2 shows the BOWW profile soil-block with the 6x6 m$^2$ shed structure on top (the wall and roof panel elements are rendered in transparent fashion so as to allow visualisation of the concrete slab, represented in green colour). Table 4.1 reports the adopted values for the most relevant properties of the shed structural model.

Table 4.1: Properties of the lightweight structure model (t: timber, c: concrete).

| Mass of superstr. (tonnes) | Base dimensions (m) | Height (m) | Period (fixed-base) (s) | $E_c$ (kPa) | $\nu_c$ | $\rho_c$ (tonnes/m$^3$) | Thickness of slab (m) | $E_t$ (kPa) | $\nu_t$ | $\rho_t$ (tonnes/m$^3$) | Thickness of walls/roof (m) |
|---|---|---|---|---|---|---|---|---|---|---|---|
| 4 | 6 x 6 | 2.4 | 0.096 | 3.0E+07 | 0.3 | 2.5 | 0.1 | 8.4E+06 | 0.2 | 0.63 | 0.07 |

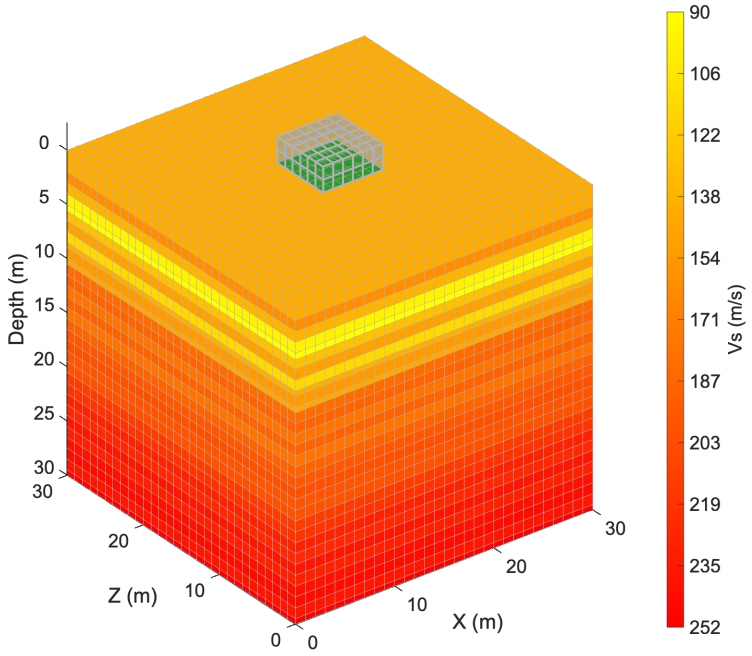


Figure 4.2 BOWW soil-block with lightweight structure model on top (note: the wall and roof panel elements are rendered in transparent fashion so as to allow visualisation of the concrete slab, represented in green colour).

## 4.3 3D numerical model of building with basement

Due to the presence of a basement, which necessarily needs to be embedded in the soil, the assembly of this structural model was considerably more complex than that described above for the lightweight structure, even if the modelling strategy was the same.

After the creation of the soil-block model, the removal of several soil brick elements close to the surface is needed, in order to model the excavation opening that houses the underground storey. The soil nodes previously belonging to the soil brick elements have to be deleted from the model; alternatively, they could be linked by *equalDOF* constraints to one of the remaining soil nodes in the model. Subsequently, it becomes possible to create several *SSPbrick* elements, characterised by concrete material properties, to model the elastic square slab at the bottom of the excavation hole. The same discretisation used for soil elements is applied to the slab, which is thus composed of 1x1 m$^2$ square elements, 0.25 m thick. As done for the shed structure, in order to take into account the superstructure's weight, concentrated vertical loads corresponding to the total mass (i.e. 363 tonnes) were applied to the upper nodes of the slab along its border.

The superstructure is again composed of four vertical panels (modelling the masonry walls) and three horizontal panels (modelling the timber floor slabs and the roof). The base nodes of the walls are linked to the upper nodes of the slab by *equalDOF* constraints in all three directions, and

therefore the horizontal mesh for the vertical panels, as well as the mesh for the horizontal panels, follow the same horizontal discretisation used for the soil. Concerning the shell mesh along the vertical direction, within the excavation height the panels are discretised as the adjacent soil and linked to the corresponding soil nodes by *equalDOF* constraints in all three directions, whilst above ground the spacing equals the inter-story height, i.e. 4 m; a more refined mesh is not needed here, since the building has an elastic behaviour and there are no other constraints on the spacing (as it happens instead for the horizontal directions). For all panels, shell elements of type *ShellMITC4* are employed, with shell section of type *ElasticMembranePlateSection*, characterised by timber material properties for the floor slabs and the roof, and masonry material properties for the walls.

In order to model the soil constraints at the ground level, "copies" of the shell nodes at that level are created and linked to the corresponding (i.e. sharing the same position) soil nodes by *equalDOF* constraints in all three directions, as well as to the "original" shell nodes by *zeroLength* elements. For the latter, the *Elastic-Perfectly Plastic Gap* material is used. The gap size is zero, since structural shell elements are intended to be adjacent to the soil-block. Very high values for stiffness and maximum force are assigned, with the force being negative in order to model a compression gap.

Wooden piles are introduced as elastic beam elements of type *elasticBeamColumn*, characterised by the same vertical discretisation used for soil elements, and linked to the corresponding soil nodes by *equalDOF* constraints in all three directions. In order to assign the same rotation, not only displacement, to the slab and the pile heads, piles are extended over the thickness of the slab. The first two pile nodes are then linked to the corresponding upper and lower nodes of the slab by *equalDOF* constraints in all three directions. The pile horizontal spacing was assigned as 4x4 $m^2$ along both directions, for a total of 5x5 = 25 piles under the 16x16 $m^2$ base slab.

The fundamental period of the fixed-base structural model is 0.2 s, which is a value expected for a two-storey building. Figure 4.3 shows the soil-block with the house on top and an embedded basement (the soil, wall and roof panel elements are rendered in transparent fashion, so as to allow visualisation of both the concrete slab, represented in green colour, as well as of the timber piles, represented in brown colour). Table 4.2 reports the adopted values for the most relevant properties of the house with basement structural model.

**Table 4.2: Properties of the house with basement structural model (t: timber, c: concrete, m: masonry).**

| Mass of superstr. (tonnes) | Base dimensions (m) | Height of superstr. (m) | Height of basement (m) | Period (fixed-base) (s) | $E_c$ (kPa) | $\nu_c$ | $\rho_c$ (tonnes/m$^3$) | Thickness of slab (m) | $E_m$ (kPa) | $\nu_m$ | $\rho_m$ (tonnes/m$^3$) | Thickness of walls (m) |
|---|---|---|---|---|---|---|---|---|---|---|---|---|
| 363 | 16 x 16 | 8.0 | 2.5 | 0.2 | 3.0E+07 | 0.3 | 2.5 | 0.25 | 9.0E+06 | 0.2 | 1.8 | 0.22 |

| $E_t$ (kPa) | $\nu_t$ | $\rho_t$ (tonnes/m$^3$) | Thickness of floor slabs/roof (m) | Pile diameter (m) | Pile length (m) | Pile spacing along $x$ (m) | Pile spacing along $z$ (m) |
|---|---|---|---|---|---|---|---|
| 1.1E+07 | 0.2 | 0.63 | 0.2 | 0.35 | 16 | 4 | 4 |

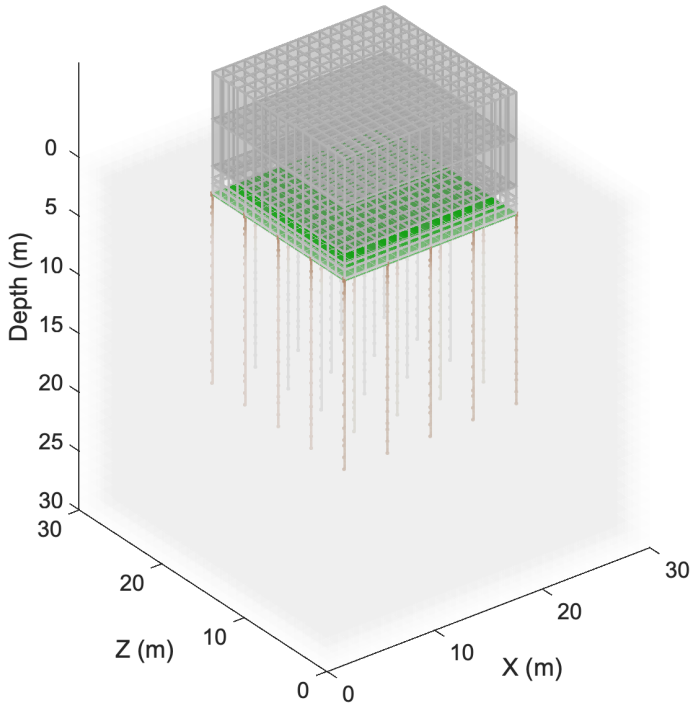


**Figure 4.3 Soil-block with a 16x16 m² house with basement on top (note: the soil, wall and roof panel elements are rendered in transparent fashion, so as to allow visualisation of both the concrete slab, represented in green colour, as well as of the timber piles, represented in brown colour).**

Given the larger footprint of the building with basement, with respect to the shed structure, the employment of a soil-block model with a larger size in plan (e.g. 60x60 m²) would have been justified. However, analyses of such larger soil-block models, which, it is recalled, must also feature the capability of modelling the response of the soil in the nonlinear range, became computationally unfeasible, especially considering the timeframe of the present study. As such, the size of the soil-block model was kept unchanged (30x30x30 m³), also because such constraint did not impair the observations and conclusions withdrawn from these analyses (see Section 6.5).

# 5 Seismic input definition and viscous damping for soil-block

Once the soil-block numerical model was built following the procedure described in Section 4.1 above, and before any analysis may be carried out, it is first necessary to both ensure that the seismic input is defined in a form that is appropriate for it to be introduced at the base of the soil-block model, as well as to set an appropriate value for the equivalent viscous damping ratio.

## 5.1 Soil-block model seismic input preparation

The definition of the seismic input for the soil-block analyses requires thus the undertaking of an additional preparatory step. As discussed in Section 3.2, the selected G-station recordings at a depth of 50 m have to be "transferred", through convolution, to the 30 m depth of the soil-block base. This convolution process was carried out with the 1D linear equivalent site response analysis software STRATA (Kottke & Rathje, 2008).

Using STRATA, the procedure schematically described in Figure 5.1 was undertaken, with a view to compute, at a depth of 30 m, the upwards motion that constitutes the input for the soil-block analyses. The STRATA models used to evaluate the amplification factors in the Groningen region (Rodriguez-Marek et al., 2017) were used, considering the soil profiles and G-station recordings described in Section 2 and Section 3.2, respectively. The selected accelerograms were thus introduced in the STRATA models as "within" motions at 50 m depth, with the upwards propagating motion that serve as input to the OpenSees soil-block models being then extracted at 30 m depth as ½ of the outcrop motion, in order to account for free surface effects.

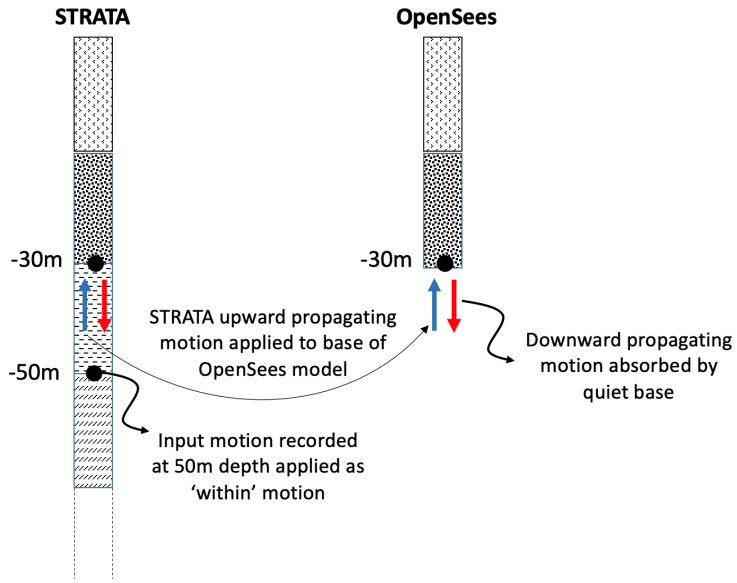


Figure 5.1 Schematic representation of the process employed to define the input motion for the soil-block.

It is noted and acknowledged that there is a degree of approximation in the soil-block seismic input preparation procedure outlined above, given that full coherency and consistency would require the acceleration history used as input for the STRATA analysis of a given soil profile to have been recorded by a borehole station at such soil profile location. This is however unfeasible, not only because for soil profiles BOWW, BAPP and BUHZ (corresponding to three B-network stations) there are no borehole recordings, but also because the use of a different seismic input for each one of the soil profiles would have prevented the comparison of the analyses results, thus significantly limiting the scope of the current numerical investigation. Nonetheless, considering

that the purpose of this study is not to precisely reproduce numerically the surface recordings starting from the borehole ones, but rather to evaluate the potential for SSI to have affected recordings at surface stations hosted inside structures, the adopted approach can be considered as being fully fit-for-purpose (even more so if one considers that shear wave velocity values at 50 or 30 m depth are essentially identical for all considered soil profiles).

One additional simplification is the assumption that the constructive interference that leads to the free-surface effects (i.e. doubling of the amplitude), is frequency-independent. In fact, it has an impact over a depth approximately equal to a quarter wavelength, with the effect tapering from the full effect at the surface to zero at the indicated depth. This implies that at some of the lower frequencies, the free-surface effect would still be seen at both depths of 30 m and 50 m, albeit with different amplitudes; whilst for higher frequencies, neither of these two depths would be affected by the free-surface effect and the correction (division by 2) would be appropriate. Since this study reveals that SSI effects are not affecting the low-frequency components of the recordings, this assumption is considered valid.

## 5.2 Equivalent viscous damping for soil-block analyses

In structural nonlinear finite element analysis, it is customary for one to introduce equivalent viscous damping with a view to both capture any sort of structural damping (e.g. frame-infill interaction) not already explicitly defined in the model, as well as to eliminate, or at least attenuate, numerical noise stemming from spurious vibration modes. In such cases, viscous damping ratios in the range of 1 to 2% are typically defined.

In the developed soil-block model, a Rayleigh damping formulation was adopted, requiring the selection of a damping ratio and two modal frequencies. Given that no soil-block eigenvalue analysis was carried out, the damping setting was made through comparison between the results from the OpenSees soil-block model, reduced to a 50 metres deep soil-column (i.e. with a 50x1x1 $m^3$ mesh), and those obtained from STRATA, where, it is recalled, shear modulus and damping degradation curves, rather than equivalent viscous damping, are introduced as input data. In particular, in OpenSees the damping settings were iteratively changed up until the attainment of the best matching with the surface acceleration history and response spectrum ordinates from STRATA, which was achieved for a 2.6% damping ratio value, set at the two identical control frequencies of 11 Hz. The comparison is displayed Figure 5.2, related to the BOWW soil profile, with nonlinear properties, subjected to record 23G461. The fact that it takes only a relatively low damping ratio value of 2.6% to make the OpenSees model yield the same results of STRATA is certainly further reassuring (this good comparison is even more significant if one considers the markedly different modelling approaches adopted in the two programs).

To gain more insight into the sensitivity of the OpenSees model to the adopted damping settings, the comparison with STRATA was also made using a minimum equivalent viscous damping ratio of 1% (used to reduce numerical noise in the results), always set at the two identical control frequencies of 11 Hz. The results shown in Figure 5.3 were obtained, where it can be readily observed how the soil response obtained in OpenSees is larger than that yielded by STRATA.

However, having observed a tendency for the impact of equivalent viscous damping to increase slightly as the mesh increases, and also to avoid the need for undertaking the required ad-hoc iterative viscous damping calibration for each combination of soil profile and accelerogram considered (recalling once more that, as discussed above, perfect matching of STRATA results is not a prerequisite of the OpenSees model in this work), the conservative option of introducing a minimum equivalent viscous damping ratio of 1% (used to reduce numerical noise in the results), keeping the two control frequencies at 11 Hz, was adopted in the analyses of the large 30x30x30 $m^3$ soil-blocks.

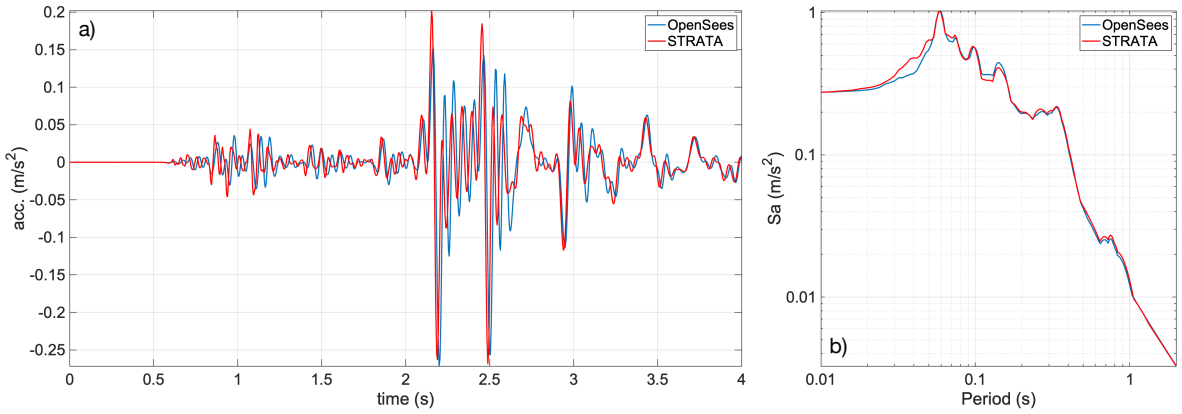


**Figure 5.2 Comparison between results obtained in OpenSees (with viscous damping ratio of 2.6%) and STRATA for a 50 m deep soil-column, in terms of free-field surface acceleration a) histories and b) spectra.**

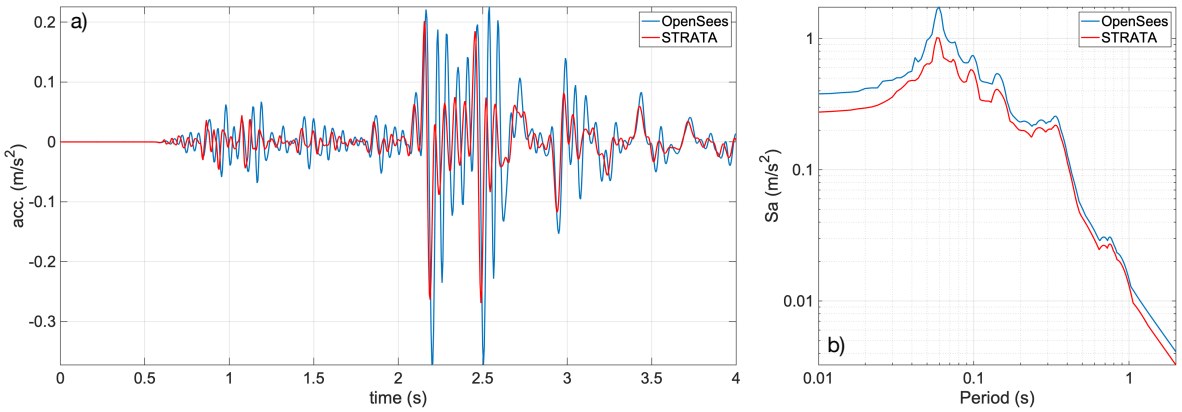


**Figure 5.3 Comparison between results obtained in OpenSees (with viscous damping ratio of 1%) and STRATA for a 50 m deep soil-column, in terms of free-field surface acceleration a) histories and b) spectra.**

# 6 Modelling approach verifications

Prior to the undertaking of the main analyses object of this study (whose results are presented in Section 0), cross-modelling validation, as well as checking on the appropriateness of the adopted modelling strategy were carried out, as described in the sub-Sections that follow.

## 6.1 Check against soil-column analysis in STRATA

As discussed before, in the present study the developed soil-block model is employed to run comparative parametric SSI analyses, where the focus is thus on the relative difference between results obtained by the same model considering different input parameters or assumptions. As such, the ability of the model to yield results that may be deemed as correct in the absolute sense could perhaps be considered as of secondary importance. However, being able to produce reliable results in absolute terms does lend valuable further reassurance and confidence to a given numerical model and to the results of subsequent comparative analyses. As such, therefore, a comparison with STRATA was herein first carried out.

Since the analyses of Section 0 were carried out for a soil-block featuring a depth of 30 metres with input motion consisting of 50 m recordings "transferred" twenty metres upwards through convolution (Section 5.1), a first check of the modelling approach was herein carried out by means of a 30 m soil-column analysis comparison with STRATA. In particular, the 30x30x30 $m^3$ OpenSees soil-block model presented in Section 4.1 was reduced into a 1x1x30 $m^3$ soil-column and its results compared with those obtained by means of a 30 m soil-column analysis in STRATA.

As can be gathered from the plots in Figure 6.1, which shows results obtained for the BOWW soil profile and record 23G461, the obtained match in terms of surface acceleration histories and response spectra is very satisfactory, especially if one considers the markedly different modelling approaches adopted in the two programs, thus demonstrating the robustness of the adopted 30 m depth soil-block modelling approach.

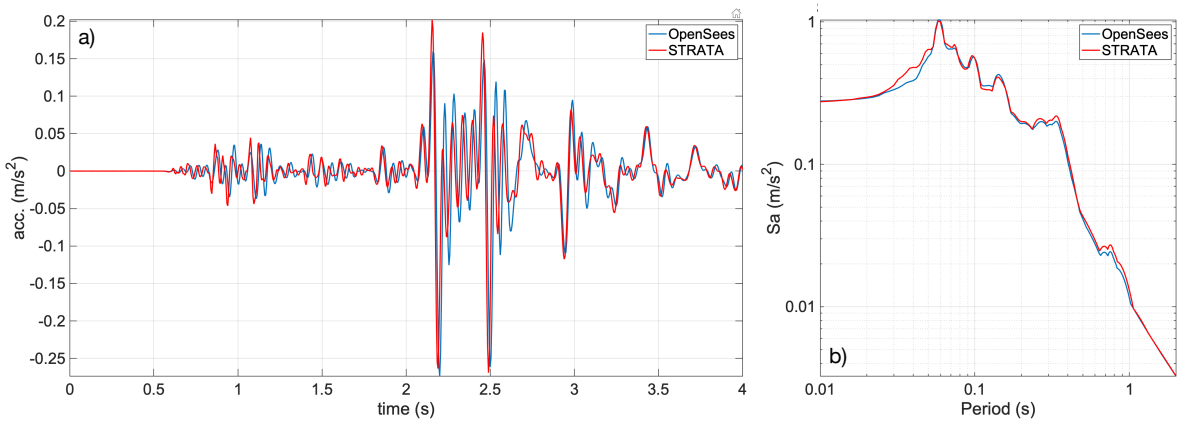


**Figure 6.1 Comparison between results obtained in OpenSees (with viscous damping ratio of 2.6%, see Section 5.2) and STRATA for a 30 m deep soil-column, in terms of free-field surface acceleration a) histories and b) response spectra.**

## 6.2 Check on boundary conditions' modelling assumptions

In this sub-Section, an effort was made to verify that the boundary conditions' modelling assumptions described in Section 4.1 are adequate; the BOWW soil profile, with linear properties,

in free-field conditions (i.e. without the shed lightweight structure on top of it) and subjected to record 23G461 was herein used for such exercise. The surface acceleration signals at six different points on the soil-block were compared, in order to check the possible presence (and influence) of wave reflections/refractions at the border of the soil domain.

The comparisons are shown in Figure 6.2 to Figure 6.7; the square in the right part of the figures is a plan view of the soil-block's upper surface, with the light grey lines showing the horizontal soil-block mesh (i.e. 1x1 m$^2$), while the red and blue dots indicate the locations of the compared surface accelerograms. As can be readily gathered, the acceleration histories at six points closer to the border of the soil domain are coincident with the one recorded at the centroid point (taken as reference), independently of their recording position, leading to the conclusions that no "border effects" are present and confirming the adequacy of the boundary conditions' modelling. It is acknowledged that, in principle, some scattered non-vertically propagating waves could develop due to the presence of a structure, but such effect is not significant (as gathered also from some of the results shown in Section 6.5).

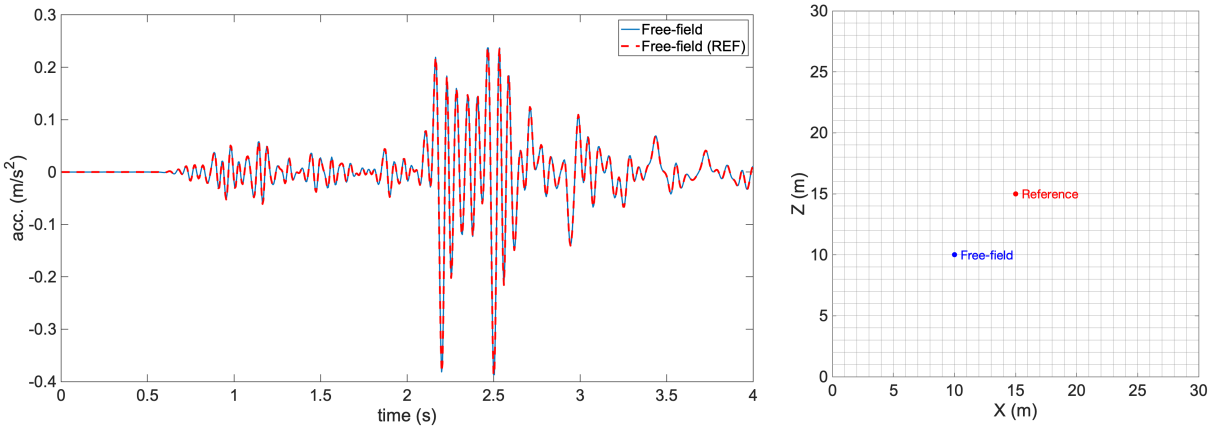


**Figure 6.2 Comparison of surface acceleration signals in the centroid point of the soil-block surface (red dot) and in one point (#1, blue dot) closer to the border.**

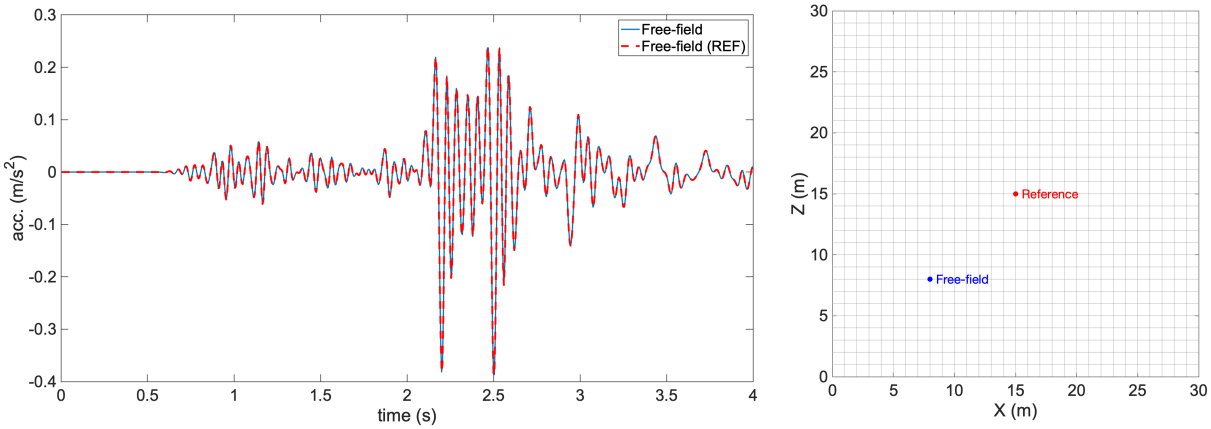


**Figure 6.3 Comparison of surface acceleration signals in the centroid point of the soil-block surface (red dot) and in one point (#2, blue dot) closer to the border.**

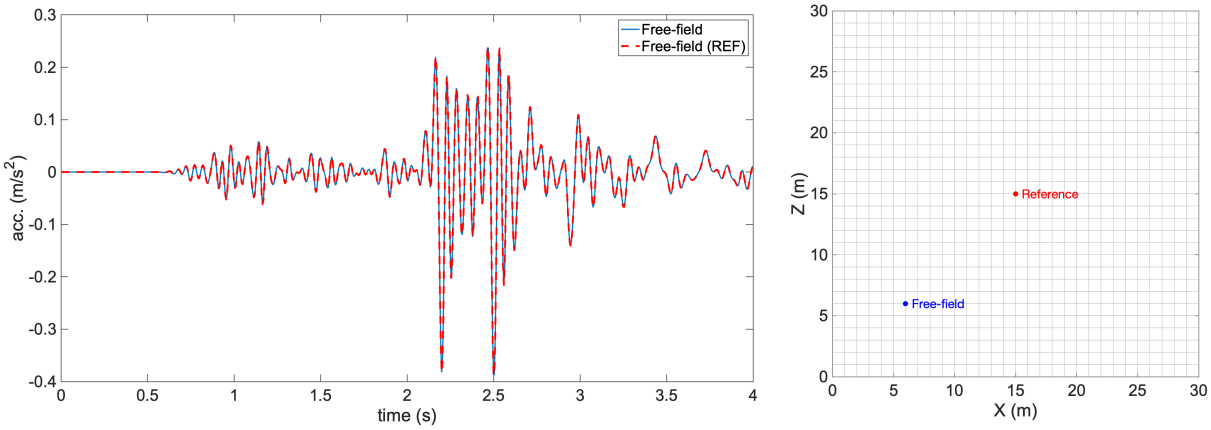


Figure 6.4 Comparison of surface acceleration signals in the centroid point of the soil-block surface (red dot) and in one point (#3, blue dot) closer to the border.

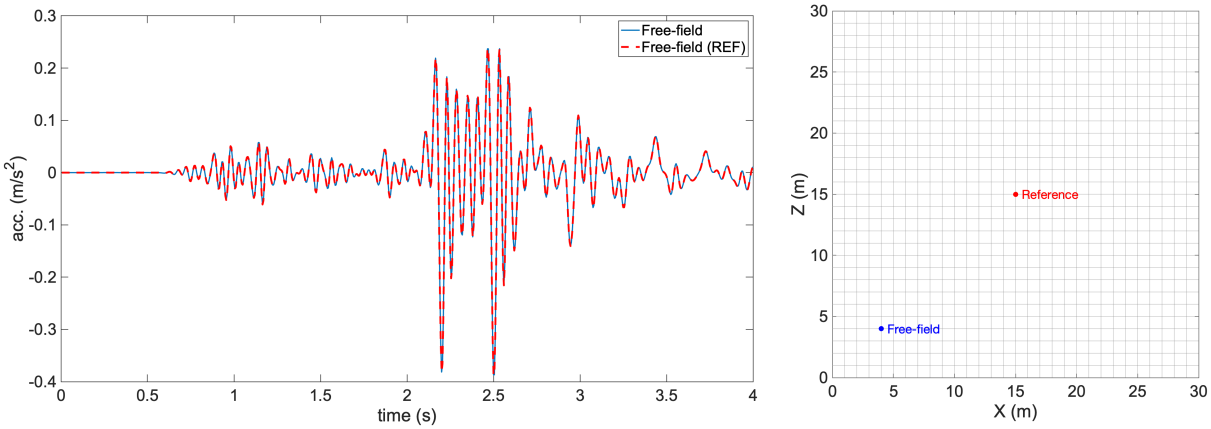


Figure 6.5 Comparison of surface acceleration signals in the centroid point of the soil-block surface (red dot) and in one point (#4, blue dot) closer to the border.

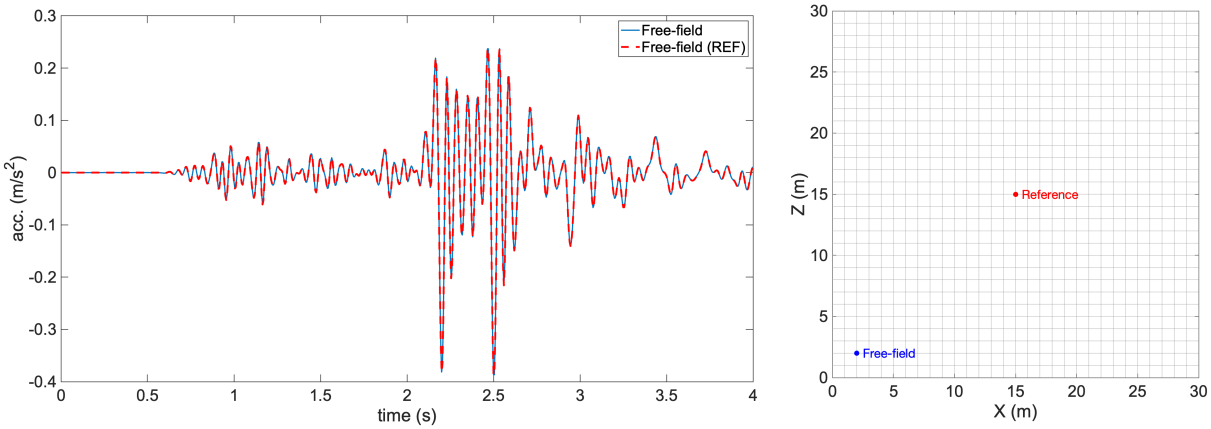


Figure 6.6 Comparison of surface acceleration signals in the centroid point of the soil-block surface (red dot) and in one point (#5, blue dot) closer to the border.

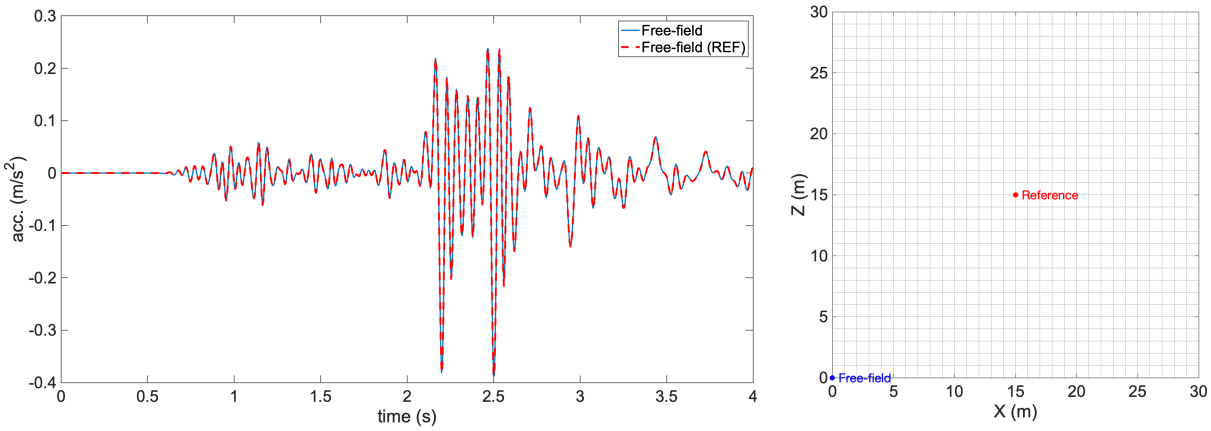


**Figure 6.7 Comparison of surface acceleration signals in the centroid point of the soil-block surface (red dot) and in one point (#6, blue dot) closer to the border.**

## 6.3 Nonlinear soil response modelling

In order to make sure that nonlinear soil response is being captured by the employed model, free-field soil-block analyses with linear and nonlinear soil material were carried out, and the corresponding surface signals (in the same location) were compared. As previously, the BOWW soil profile was considered. Figure 6.8 shows the comparison in terms of acceleration histories and response spectra for record 23G461, which is one of the strongest among the considered records. It can be noticed that the "linear" and "nonlinear" signals are practically superimposed in the time windows of lower intensity, while they diverge, albeit not significantly, around the peaks of the signal (about +0.2 m/s$^2$ and -0.4 m/s$^2$). This confirms that soil nonlinearity does play a role in the problem at hand, leading to energy dissipation that reduces the intensity of shaking at the surface in terms of accelerations.

The effect of soil nonlinearity becomes even more evident, as expected, when the soil-block model is subjected to higher intensity motions, as can be seen in Figure 6.9 and Figure 6.10, reporting the results from analyses considering, as input, record 23G461 linearly scaled by factors of 3 and 8; unlike in its linear analysis counterpart, the surface acceleration history obtained from nonlinear analysis does not scale linearly with the intensity of the input signal at the base, thus leading to an increase in the difference between the results obtained with the two analyses, highlighting the presence of nonlinear soil response and energy dissipation. Additionally to the clear reduction in acceleration amplitudes, one may also notice in Figure 6.9a) and Figure 6.10a) a slight "delay" in the nonlinear response during the larger amplitude part of the acceleration history in comparison to the linear one, corresponding to the expected shift in vibration periods towards larger values.

On the contrary, when considering input motions of lower intensity, such as e.g. record 24G111, the influence of soil nonlinearity becomes, as expected, negligible, with the "linear" and "nonlinear" signals being practically superimposed in the entire time window, as gathered from Figure 6.11.

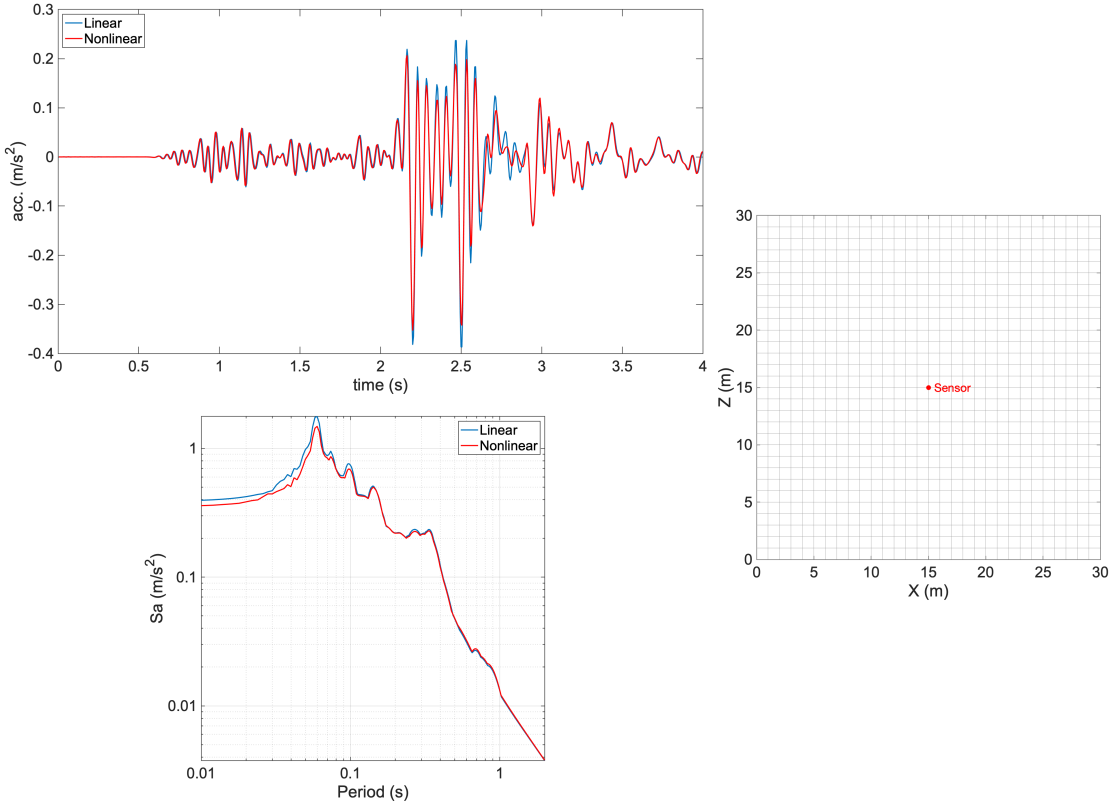


Figure 6.8 Comparison of surface free-field acceleration signals considering linear and nonlinear soil material, for record 23G461.

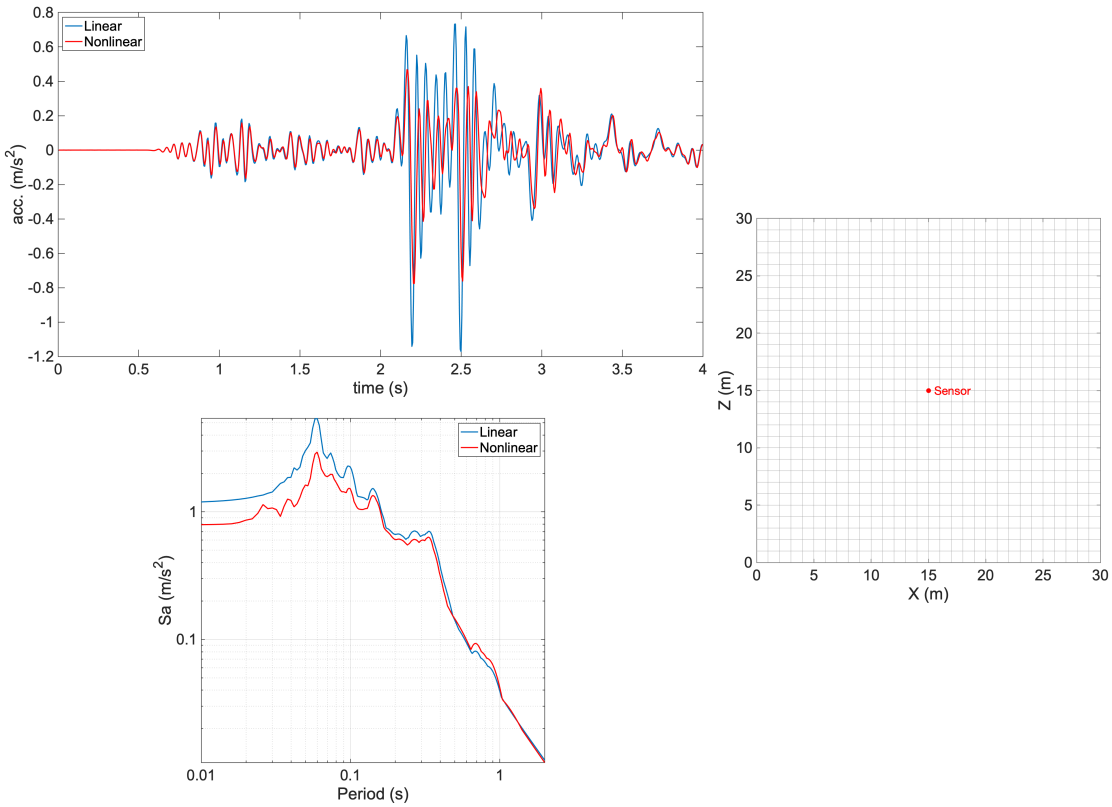


Figure 6.9 Comparison of surface free-field acceleration signals considering linear and nonlinear soil material, for record 23G461x3.

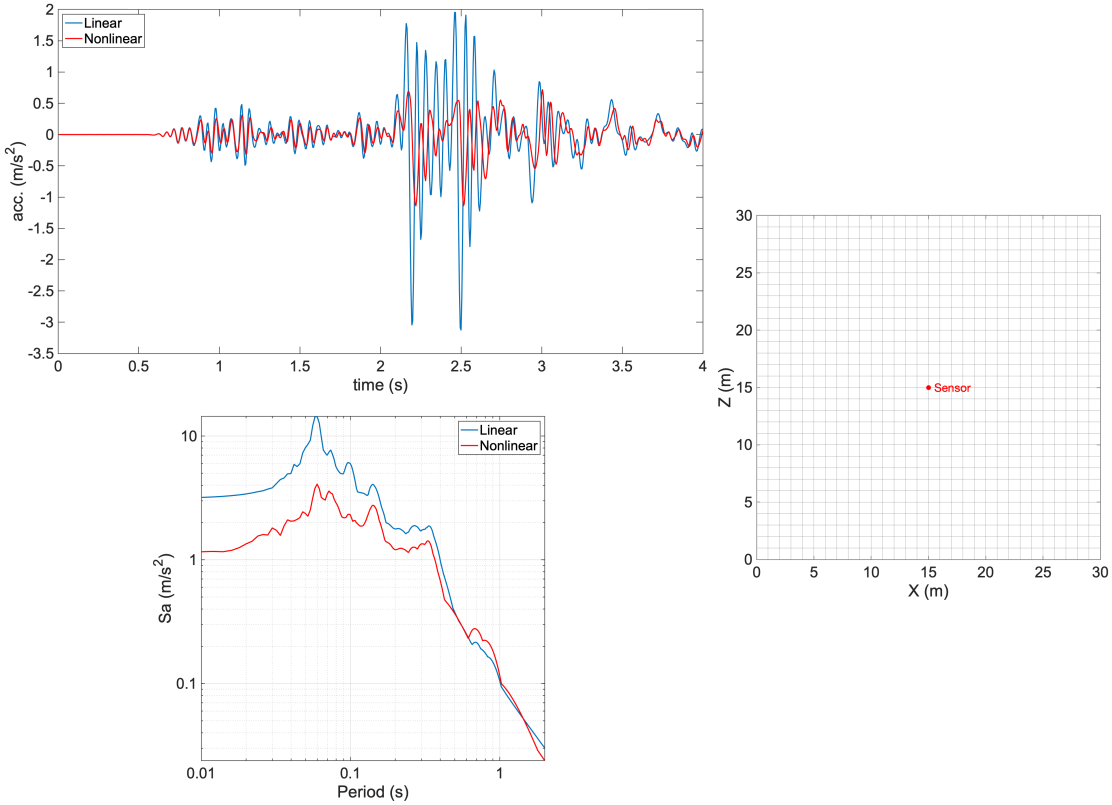


**Figure 6.10 Comparison of surface free-field acceleration signals considering linear and nonlinear soil material, for record 23G461x8.**

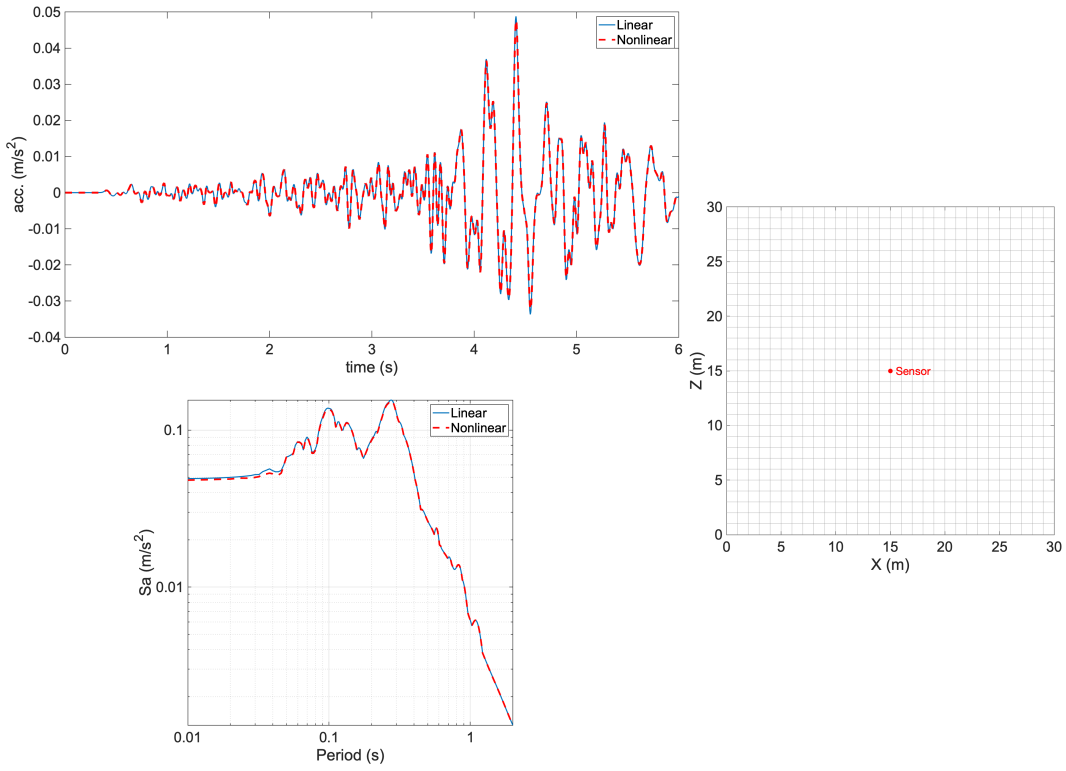


**Figure 6.11 Comparison of surface free-field acceleration signals considering linear and nonlinear soil material, for record 24G111.**

## 6.4 Soil profile variation effects

As already mentioned in Section 1, it is expected that a variation in soil profile properties will lead to differences in surface recordings. Hence, analysis of the soil-block model described in Section 4.1 considering different soil profiles should lead to the attainment of distinct results. Such comparative numerical runs were thus herein carried out, applying the same seismic input, record 23G461, at the base of the soil-block model, but then considering the six different soil profiles presented in Section 2, in free-field conditions (i.e. without any structure on top of the soil-block).

We start by comparing the signals obtained for the BUHZ and G040 soil profiles, in terms of acceleration histories and response spectra (Figure 6.12). These two locations are approximately 900 m distant one from the other and had been "paired" together in the work by Witteveen+Bos (2019). As noticed in Section 2, however, they do feature distinct soil properties, and hence would be expected to give rise to different free-field signals, something that is indeed observed in the numerical results (which, it is reiterated, correspond to free-field conditions).

In Figure 6.13 the comparison is extended to the remaining soil profiles (BOWW, BAPP, G180 and G390), in terms of response spectra. The differences in the results obtained for each of the soil profiles confirm again the capability of the developed numerical model to capture the impact of varying properties of the soil, which is reassuring.

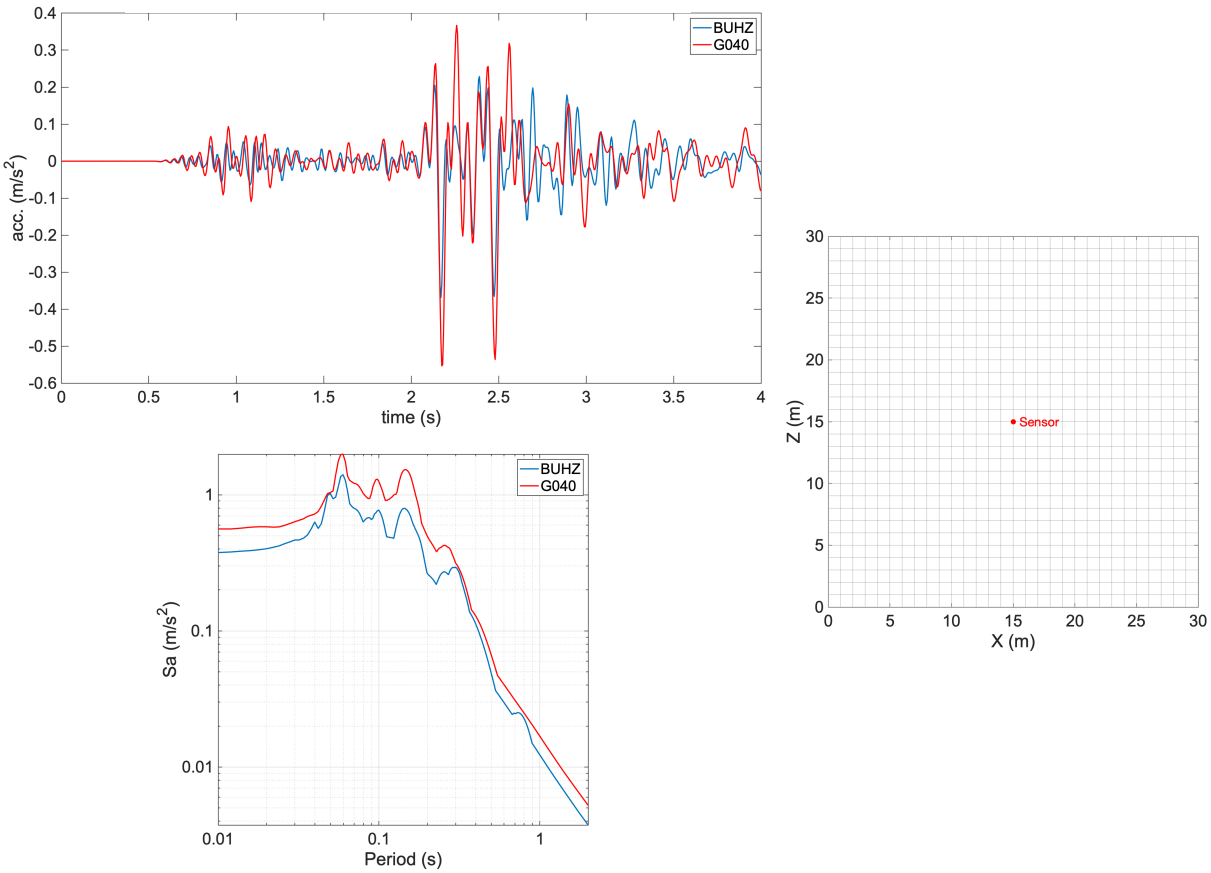


**Figure 6.12 Comparison of free-field surface acceleration signals considering soil profiles BUHZ and G040, for record 23G461.**

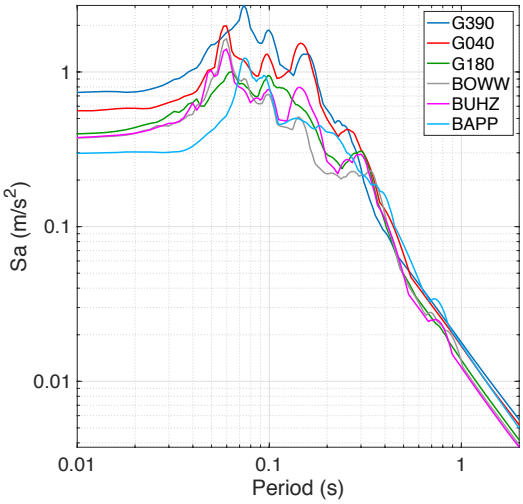


**Figure 6.13 Response spectra comparison of the free-field surface acceleration signals for all six different soil profiles, under record 23G461.**

## 6.5 Basement SSI effects

As already discussed, structures with basements typically give rise to soil-structure interaction effects, both of the inertial and kinematic type (Stewart, 2000). As such, an analysis of the soil-block model described in Section 4.1 with the structural model of Section 4.3 (building with basement) on top of it should show the presence of SSI effects, with acceleration histories from inside the building being different from free-field ones.

An analysis was thus carried out considering the BOWW soil profile subjected to record 23G461, and the acceleration signal at the basement of the building was compared (Figure 6.14) against its free-field counterpart (i.e. an acceleration history obtained at the same depth of the basement level on a soil-block without the structure on top). The square in the right part of Figure 6.14 indicates in green the footprint of the building with basement (larger than the shed footprint), while the red dot indicates the location of the accelerometer (sensor) in the structure's basement. The clear differences between the two signals, both in terms of acceleration histories as well as response spectra, confirm that the developed numerical model does capture SSI effects when these are supposed to be present, as in the case of a building with a basement.

It is noted that if the acceleration history at the basement of the building is compared with a free-field signal at surface level, rather than at basement depth, then the differences become even more pronounced (see Figure 6.15), due to the non-negligible level to which the basement is embedded in the soil. This result is fully aligned and very much corroborates the typical practice of not considering recordings from instruments located in building basements in the development of ground motion models (see Stewart, 2000).

The capability of the adopted modelling strategy in capturing inertial and kinematic SSI effects can also be gathered by noticing that, contrarily to what happens for the case of the lightweight shed structure (see Figure 6.16 and Figure 6.17), when a heavy structure with a basement is analysed, the signals recorded at three different points surrounding the structure do not correspond to free-field conditions (see Figure 6.18, Figure 6.19 and Figure 6.20, below). From these comparisons it was also observed that, as expected, the divergence between signals gradually reduces with the distance from the structure, with a signal similar to free-field being obtained at the edge of the soil-block model (Figure 6.20); this confirms also that the soil-block model size constraints discussed in Section 4.3 did not impair the analyses in any significant manner.

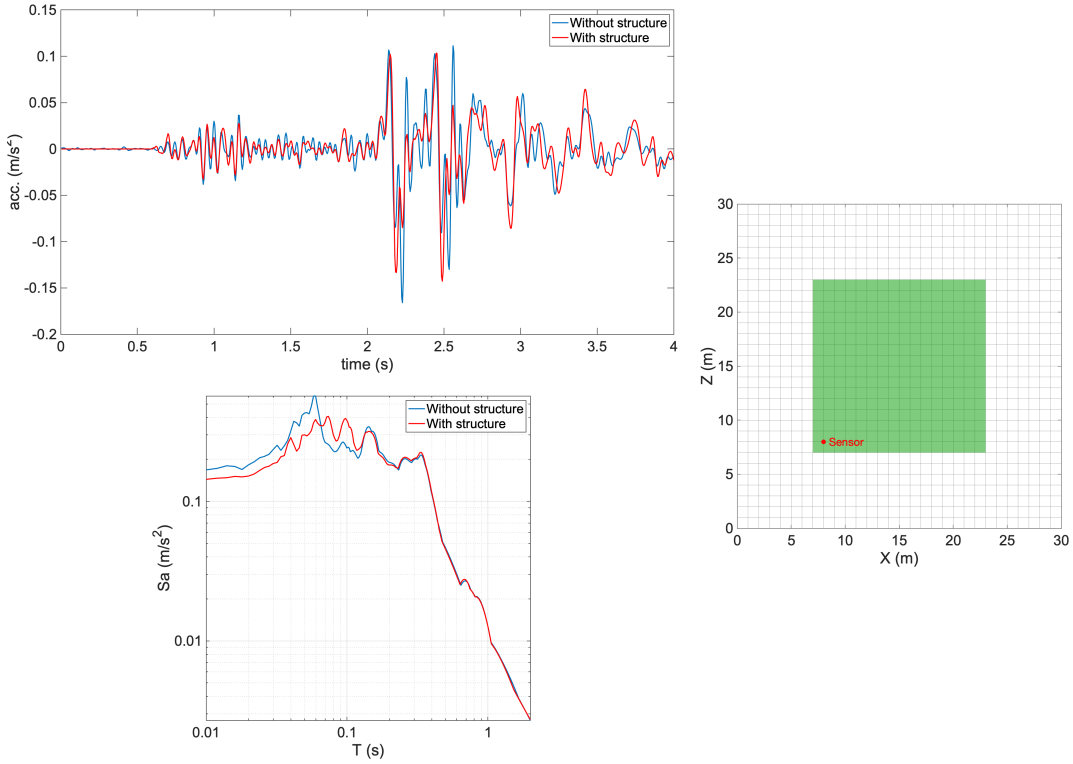


Figure 6.14 Comparison of acceleration signals at basement level depth, with and without the structure on top, for the BOWW profile and record 23G461.

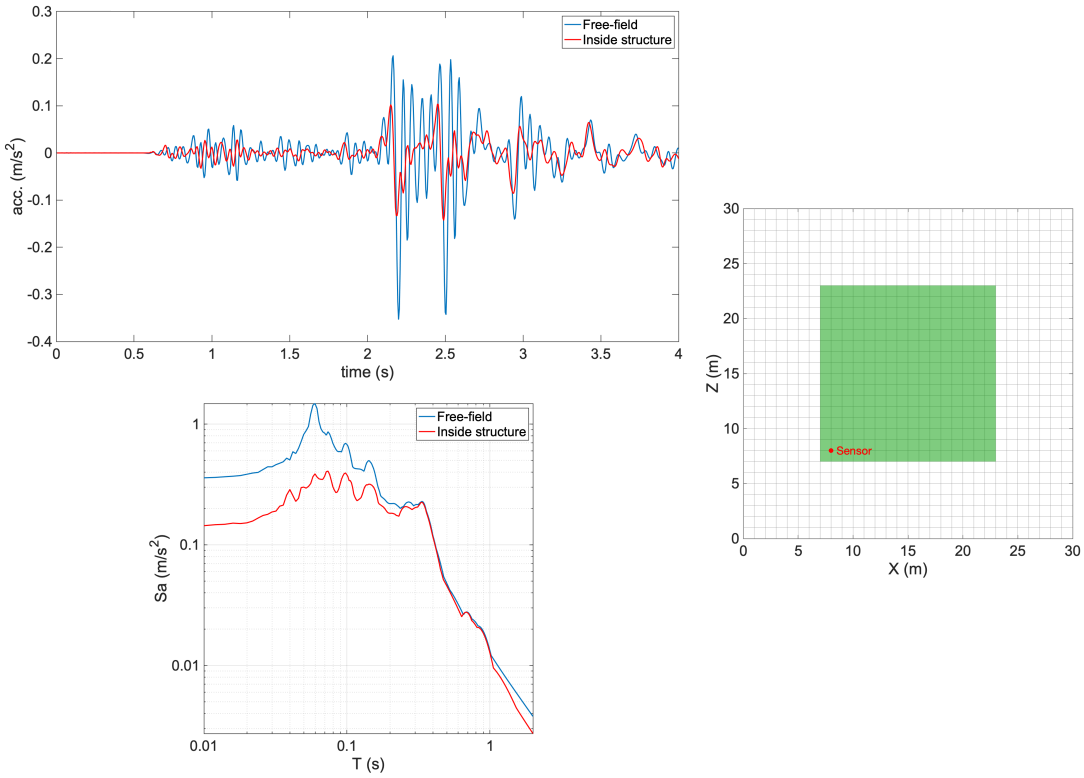


Figure 6.15 Comparison of the acceleration signal at the basement of the building with the free-field signal at surface level, for the BOWW profile and record 23G461.

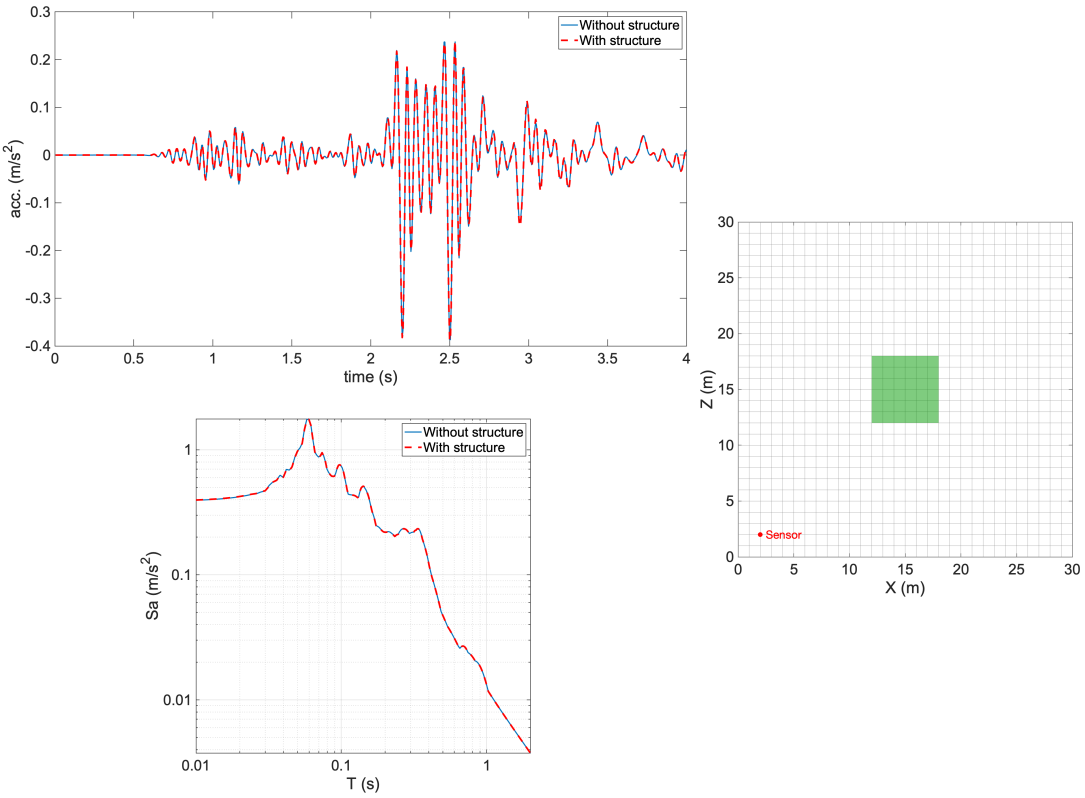


Figure 6.16 Comparison of surface acceleration signals in point #1 (red dot) from soil-block analyses with and without the lightweight shed structure on top of it, for the BOWW profile and record 23G461.

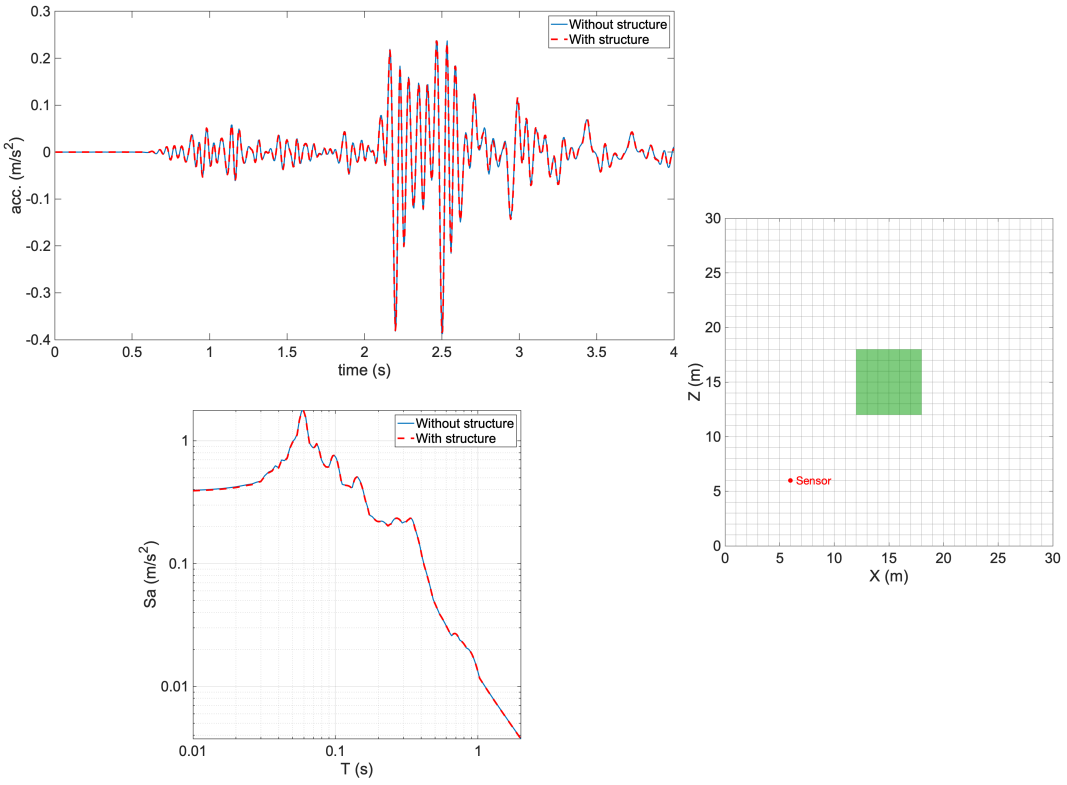


Figure 6.17 Comparison of surface acceleration signals in point #2 (red dot) from soil-block analyses with and without the lightweight shed structure on top of it, for the BOWW profile and record 23G461.

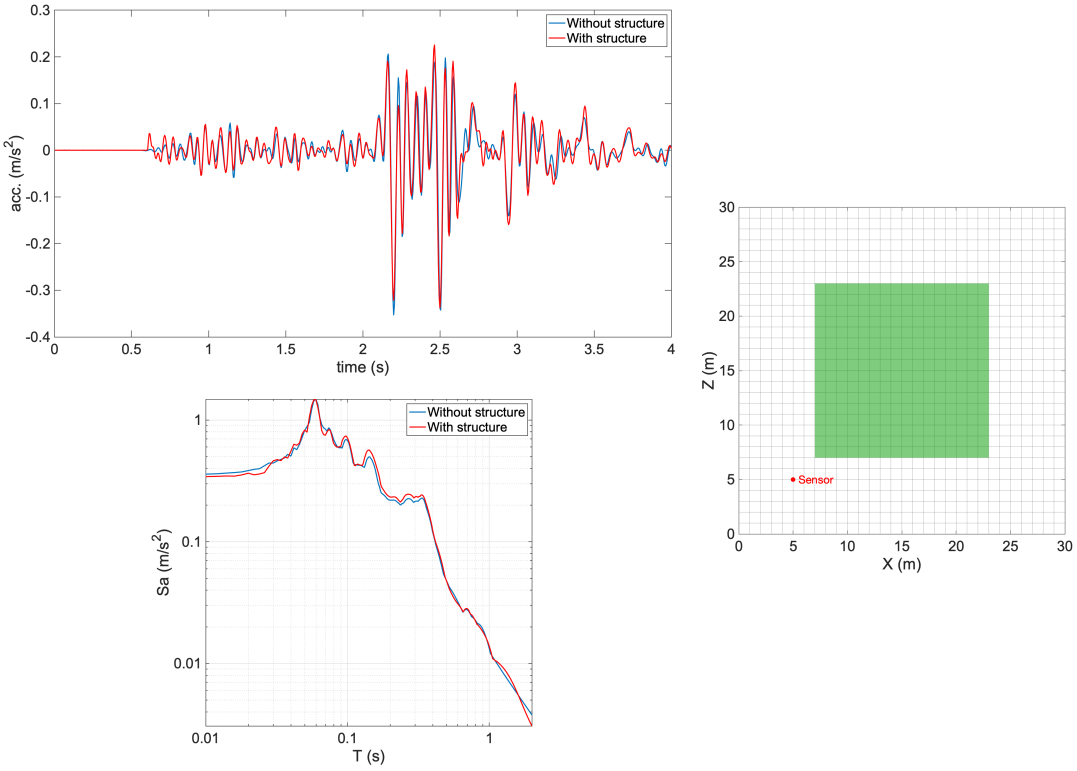


Figure 6.18 Comparison of surface acceleration signals in point #1 (red dot), from soil-block analyses with and without the heavy basement structure on top of it, for the BOWW profile and record 23G461.

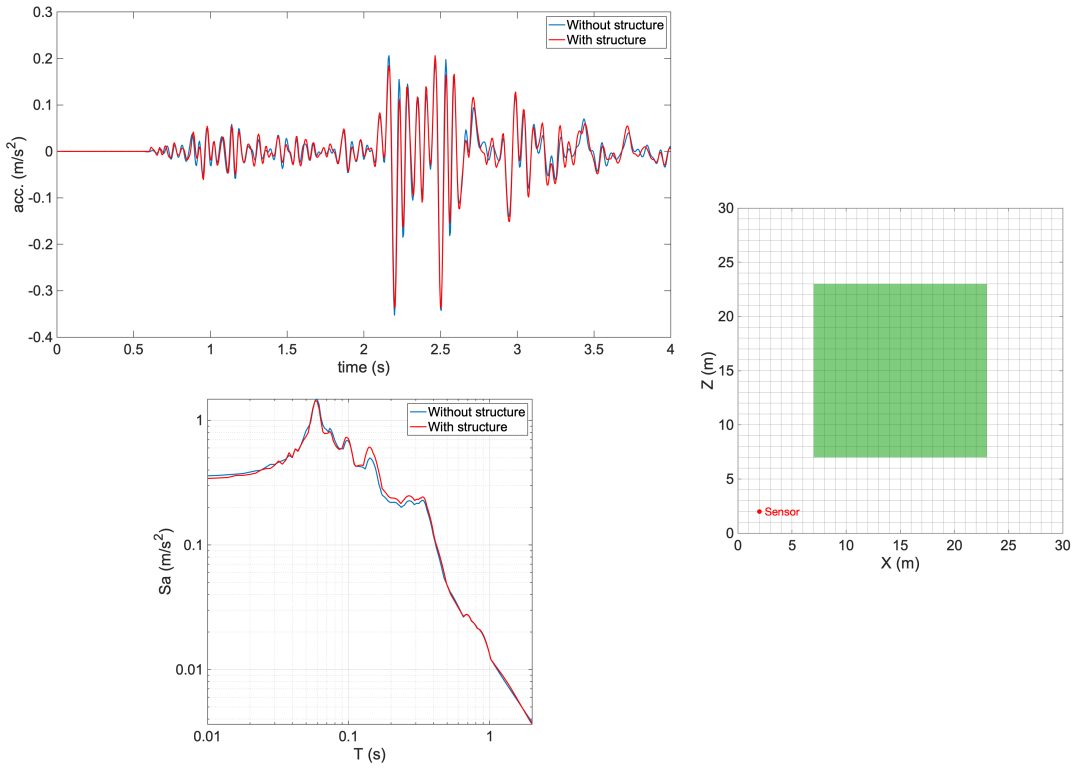


Figure 6.19 Comparison of surface acceleration signals in point #2 (red dot), from soil-block analyses with and without the heavy basement structure on top of it, for the BOWW profile and record 23G461.

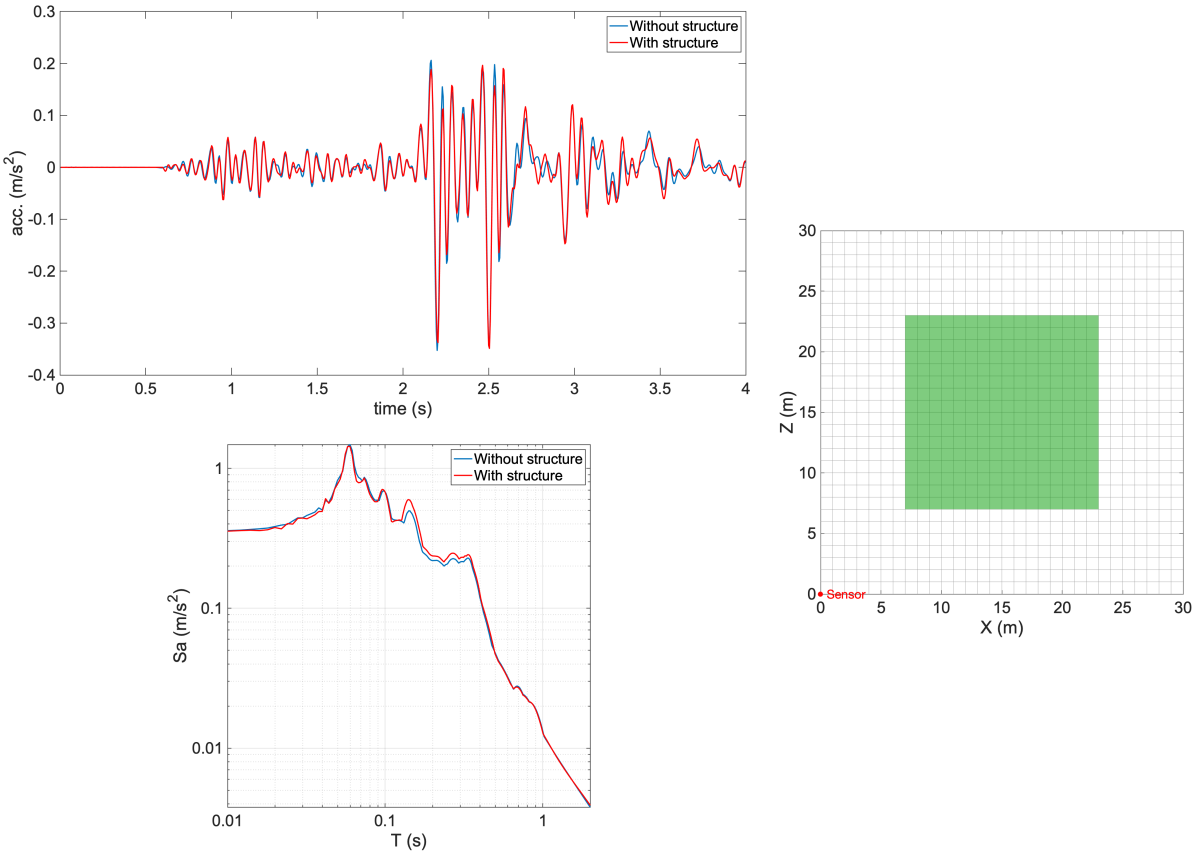


**Figure 6.20 Comparison of surface acceleration signals in point #3 (red dot), from soil-block analyses with and without the heavy basement structure on top of it, for the BOWW profile and record 23G461.**

## 6.6 Embedment and incoherence correction functions for basement recordings

A final set of preliminary analyses involved the comparison between the soil-block acceleration signals at the surface and those obtained by adjusting the numerical basement signals with the employment of embedment and base-slab averaging correction functions available in the literature (e.g. NIST, 2012, Sotiriadis et al., 2019, 2020). The latter typically involve the employment of transfer functions, which describe the ratio between the amplitude of the Fourier transforms of the foundation input motion, $u_{FIM}$, and those of the free-field surface ground motion, $u_g$.

Herein, two transfer functions found in the report by NIST (2012) were used. The first one aims at correcting the effect of the basement's embedment; for embedded rectangular foundations, the transfer function $H_{u,1}$ for foundation translation is expressed as a function of circular frequency $\omega$, basement depth $D$ and average value of the shear wave velocity within the depth of interest $V_{S,avg}$ (see NIST, 2012):

$$H_{u,1} = \frac{u_{FIM}}{u_g} = \cos\left(\frac{D \cdot \omega}{V_{s,avg}}\right), \quad \frac{D \cdot \omega}{V_{s,avg}} < 1.1 \tag{6.1}$$

$$H_{u,1} = 0.45, \quad \frac{D \cdot \omega}{V_{s,avg}} > 1.1 \tag{6.2}$$

The second transfer function aims at correcting the base-slab averaging of incoherent incident waves; a semi-empirical model based on a theoretical formulation of the kinematic interaction problem by Veletsos and Prasad (1989) was adopted. The transfer function $H_{u,2}$ for vertically propagating shear waves and a shallow foundation of width $B$ can be written as:

$$H_{u,2} = \frac{u_{FIM}}{u_g} = \left\{\frac{1}{b_0^2}\left[1 - \exp(-2b_0^2)\left(I_0(2b_0^2) + I_1(2b_0^2)\right)\right]\right\}^{1/2} \quad (6.3)$$

where $b_0 = \left(\sqrt{4/\pi}\right)\kappa_a a_0^k$ , $\kappa_a = 0.00065 \times V_{S,avg}$ (for $200 < V_{S,avg} < 500$ m/s ), $a_0^k = \omega B/2V_{S,avg}$, while $I_0$ and $I_1$ are modified Bessel functions (see NIST, 2012).

The two transfer functions for the BOWW soil profile are shown in Figure 6.21 (see Annex A for further details on their derivation), whilst the "improvement" of the signal obtained at the embedded foundation can be assessed by comparing Figure 6.22 with Figure 6.15.

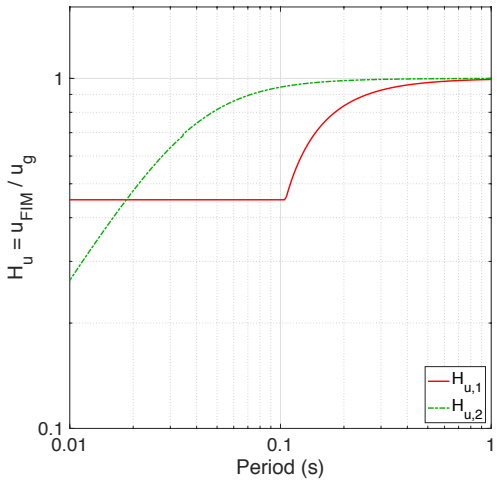


**Figure 6.21 Embedment and base-slab averaging correction transfer functions, for the considered basement building and the BOWW soil profile.**

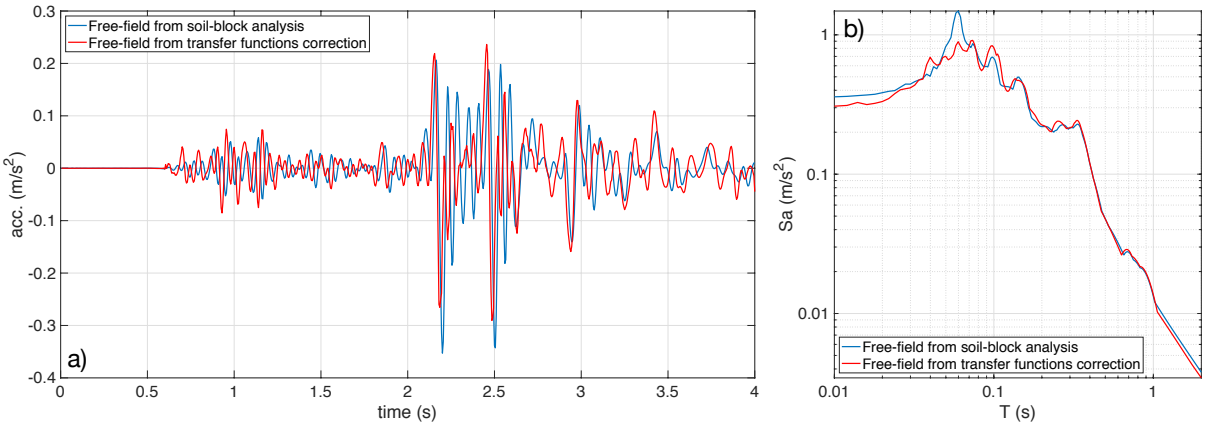


**Figure 6.22 Comparison between the soil block free-field acceleration signal and that estimated by adjusting the numerical basement signal using the transfer functions correction, in terms of a) time-histories and b) response spectra.**

It is noted that, in principle, there should be a need to apply only the $H_{u,1}$ transfer function (correcting for embedment effects) to the numerical basement signal, given that in the developed soil-block model and corresponding analyses the input motion did not feature incoherency. However, it was observed that the application of both transfer functions led to a better comparison with the free-field motion obtained with the numerical analyses (Figure 6.22), with respect to when $H_{u,1}$ was applied in isolation (Figure 6.23). Further studies should be carried out in order to understand if this is a result of e.g. an insufficient embedment correction being introduced by $H_{u,1}$, the generation of potential (minor) incoherencies due to wave reflection at the corners of the basement, or some other factor.

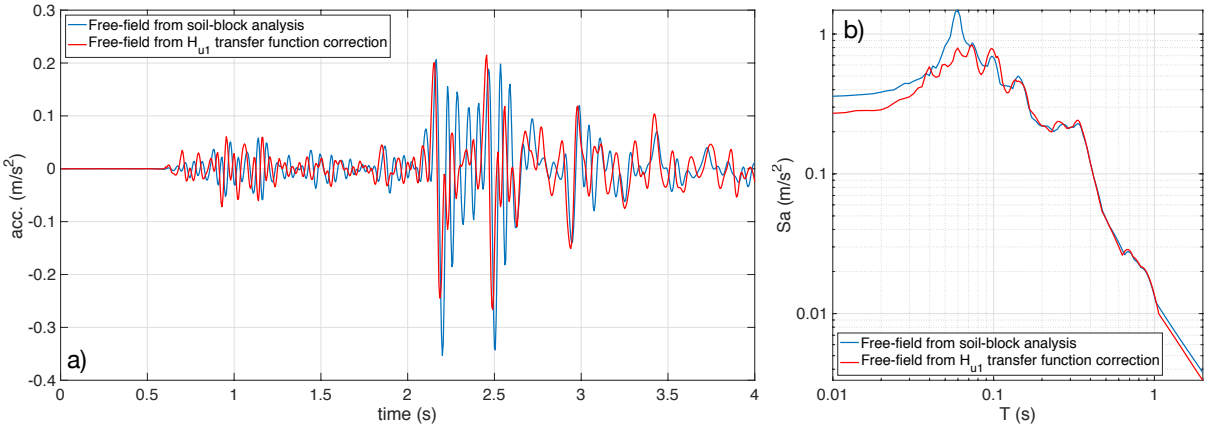


**Figure 6.23 Comparison between the soil block free-field acceleration signal and that estimated by adjusting the numerical basement signal using the transfer function $H_{u,1}$ correction alone, in terms of a) time-histories and b) response spectra.**

Independently of the above discussion, the fact that the relation between the free-field and basement level signals obtained in the soil-block model is very much comparable to what is obtained using transfer functions available in the literature (as gathered from the comparison between Figure 6.22 and Figure 6.15) is once again reassuring regarding the developed soil-block model.

# 7 Investigation of variations between free-field earthquake ground motions and foundation-level recordings in lightweight structures

The adopted modelling was shown above to be seemingly working correctly and producing results with appropriate/expected trends. Hence it is now possible to undertake the dynamic analyses aimed at, firstly, assessing if recordings from instruments located in lightweight structures (like sheds or barns) may or may not be affected by SSI effects, and then, if the latter are not observed, identifying an alternative possible explanation for the apparent trend for lower high-frequency spectral ordinates noticed in recordings from B-network stations (see discussion in Section 1).

## 7.1 Potential for the generation of SSI effects

As stated above, the possible influence of the station hosting structure on surface acceleration recordings was herein first investigated. The BOWW profile was considered, together with records 23G461, 24G111, 25G421, and soil-block analyses were carried out with the lightweight structure (in this case, a shed) on top of it, with the resulting surface acceleration signal inside the structure being then compared with those obtained in free-field conditions. Figure 7.1, Figure 7.2 and Figure 7.3 show the comparisons in terms of acceleration histories and response spectra for records 23G461, 24G111 and 25G421, respectively. From the three figures, it can be clearly seen that signals at free-field and from inside the structure are practically identical, at all levels of intensity, with no attenuation of low-period spectral ordinates (which would have been indicative of the presence of SSI); on the contrary, as further scrutinised subsequently, a very slight amplification of low-period spectral ordinates has developed.

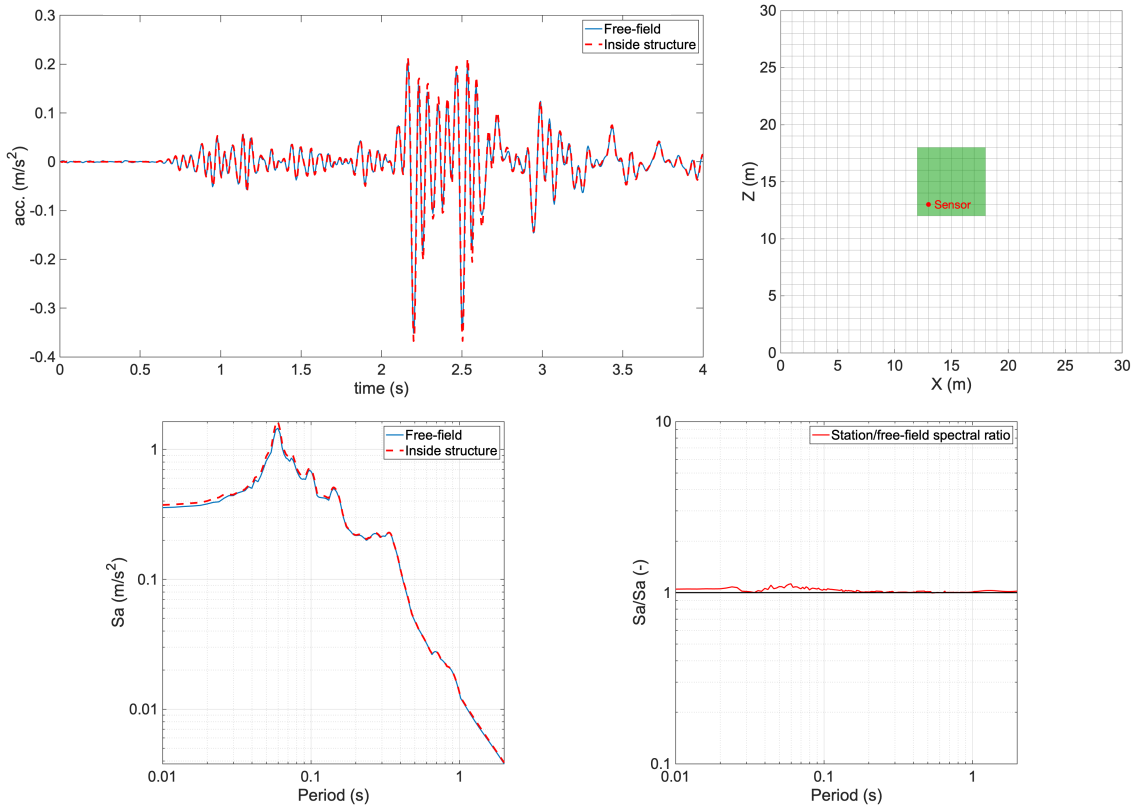


**Figure 7.1 Comparison of surface acceleration signals inside the shed (red dot) and in free-field conditions, considering the BOWW profile, for record 23G461, in terms of time-histories, response spectra and spectral ratio.**

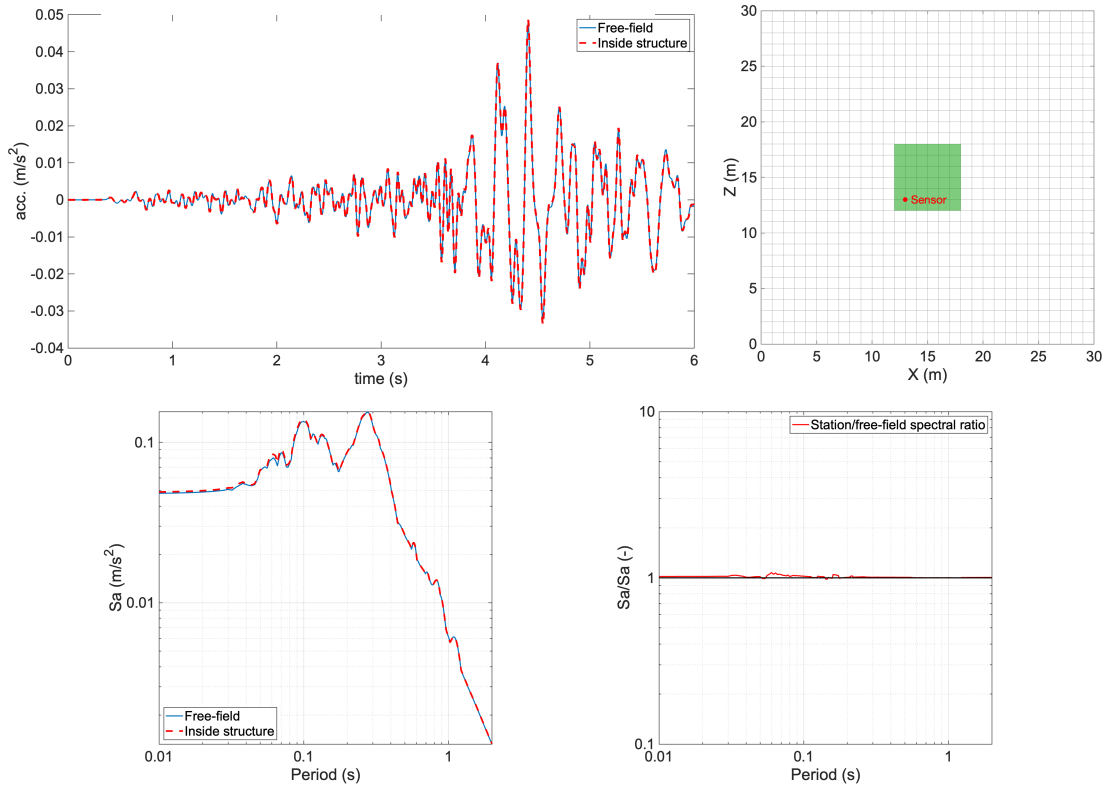


**Figure 7.2 Comparison of surface acceleration signals inside the shed (red dot) and in free-field conditions, considering the BOWW profile , for record 24G111, in terms of time-histories, response spectra and spectral ratio.**

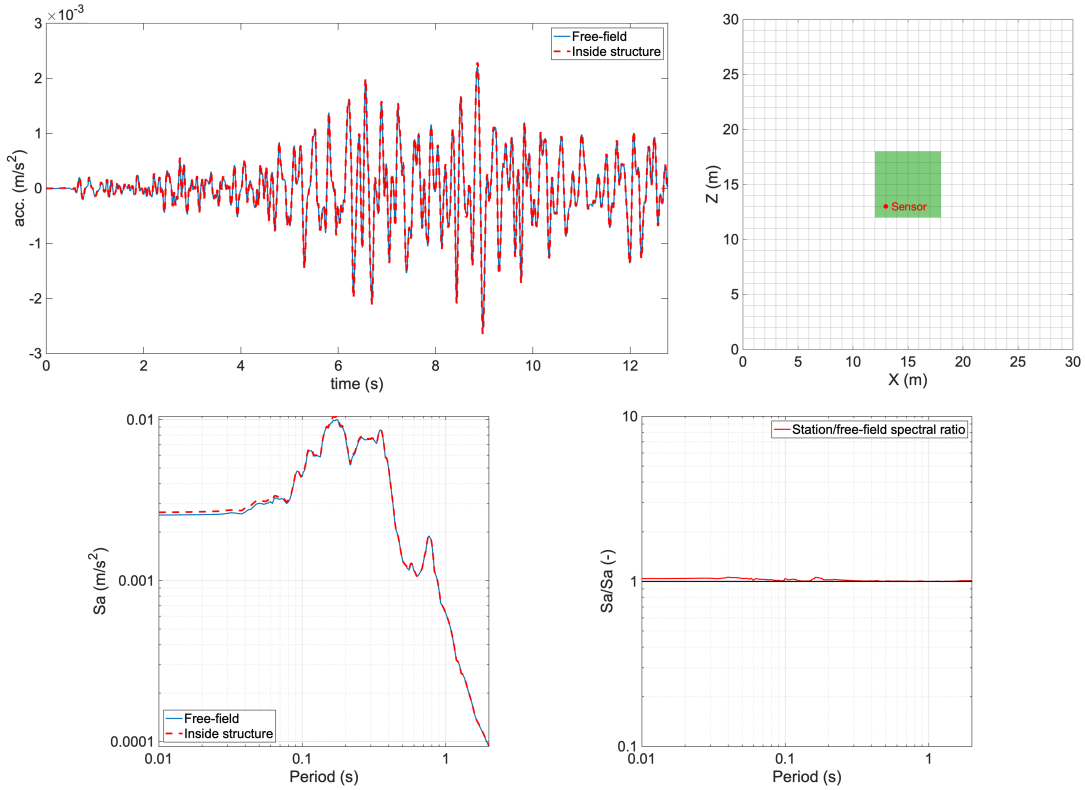


**Figure 7.3 Comparison of surface acceleration signals inside the shed (red dot) and in free-field conditions, considering the BOWW profile , for record 25G421, in terms of time-histories, response spectra and spectral ratio.**

Further similar comparisons were made considering four additional soil profiles, namely BUHZ (Figure 7.4), G040 (Figure 7.5), G180 (Figure 7.6) and G390 (Figure 7.7), together with the strongest of the records used above with the BOWW soil profile, i.e. the 23G461 accelerogram. Whilst the same trend as before is observed for the BUHZ and G180 soil profiles (i.e. signals at free-field and from inside the structure are practically identical), in the case of the G040 and G390 soil profiles the acceleration histories inside the structure deviate slightly from their free-field counterparts. Still, no systematic attenuation of low-period spectral ordinates is observed, attesting that, contrarily to the case of basement structures (Section 6.5), no SSI effects of relevance are developed by the lightweight structures hosting B-network stations.

A very slight amplification of low-period spectral ordinates can be observed in the results shown herein. To investigate the possible origin of this behaviour, and also gain further reassurance on the results obtained above, the lightweight shed structure was also analysed through a substructure SSI modelling approach, more specifically, using the validated nonlinear SSI shallow foundations macro-element by Correia and Paolucci (2020), schematically represented in Figure 7.8, implemented in the SeismoStruct structural analysis software (Seismosoft, 2020), and already employed in the development of fragility functions (Cavalieri et al., 2020) for the seismic risk analysis of the Groningen field (van Elk et al., 2019).

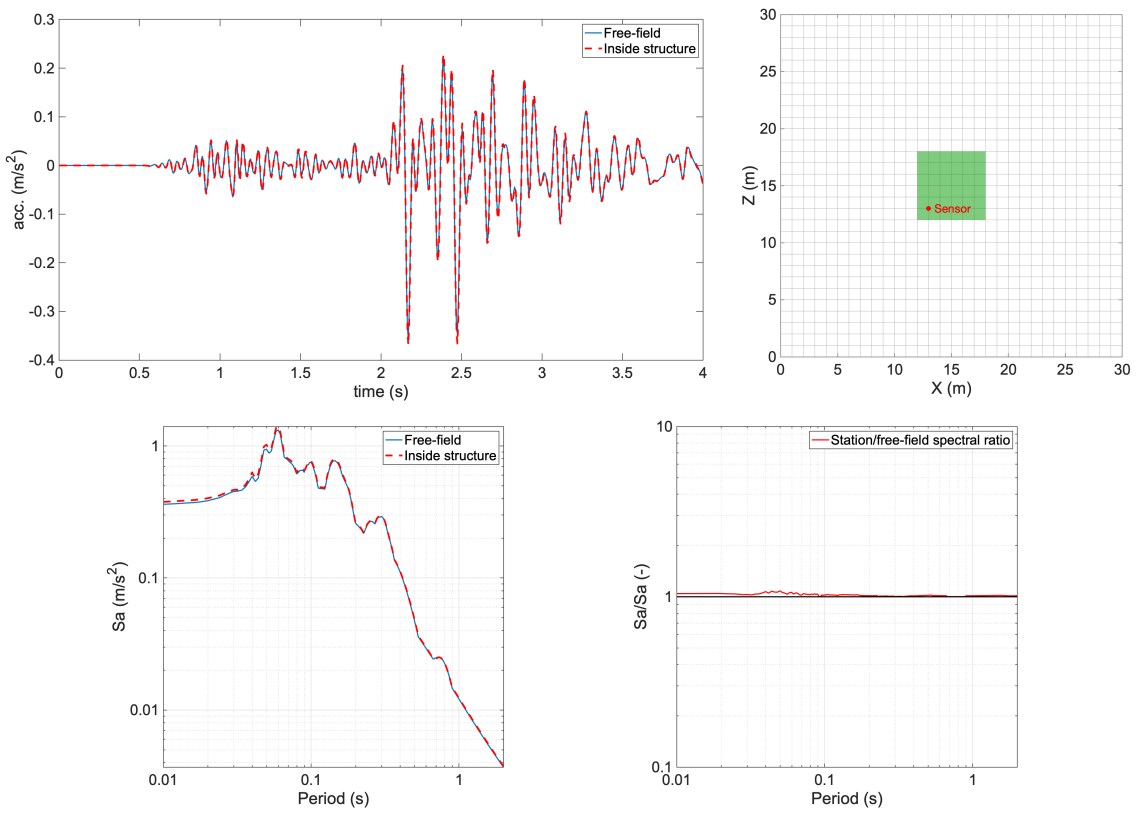


**Figure 7.4 Comparison of surface acceleration signals inside the shed (red dot) and in free-field conditions , considering the BUHZ profile, for record 23G461, in terms of time-histories, response spectra and spectral ratio.**

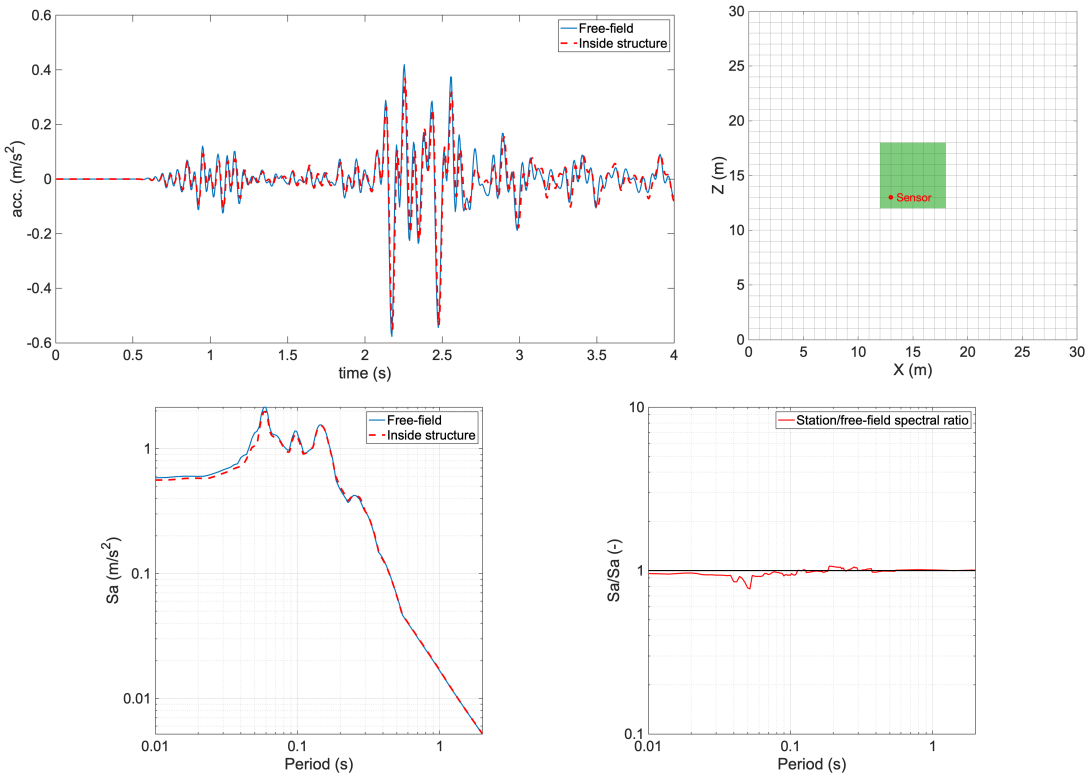


**Figure 7.5 Comparison of surface acceleration signals inside the shed (red dot) and in free-field conditions, considering the G040 profile, for record 23G461, in terms of time-histories, response spectra and spectral ratio.**

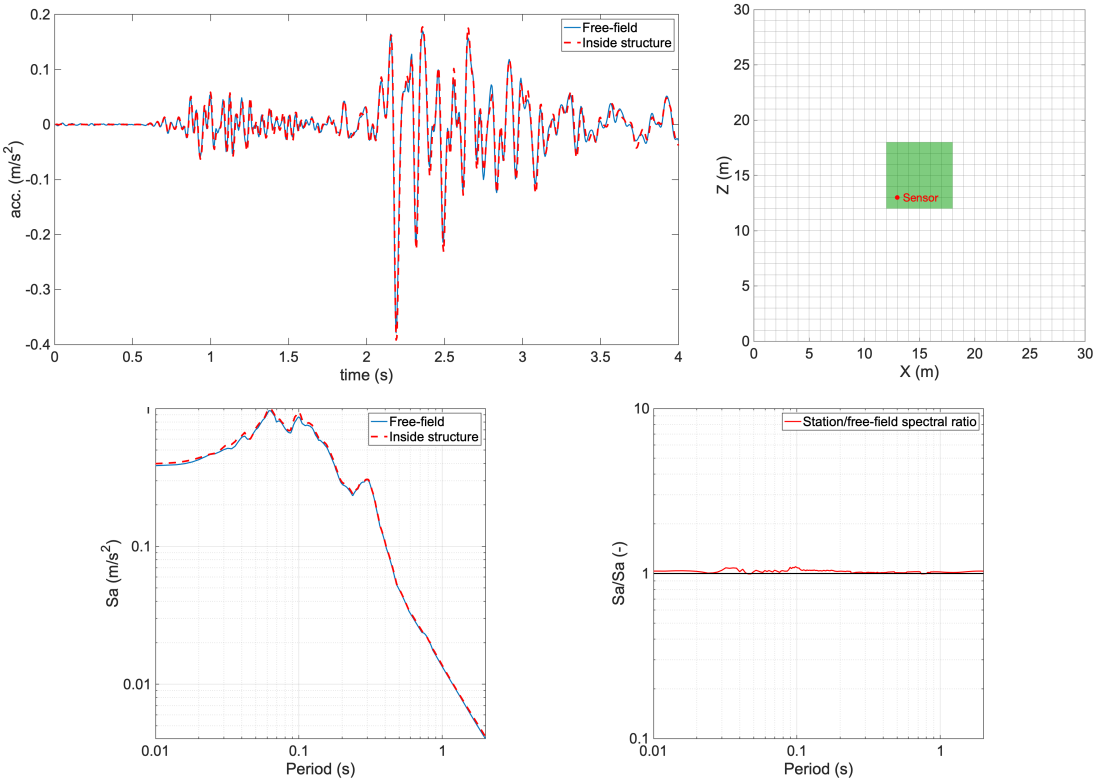


**Figure 7.6 Comparison of surface acceleration signals inside the shed (red dot) and in free-field conditions, considering the G180 profile, for record 23G461, in terms of time-histories, response spectra and spectral ratio.**

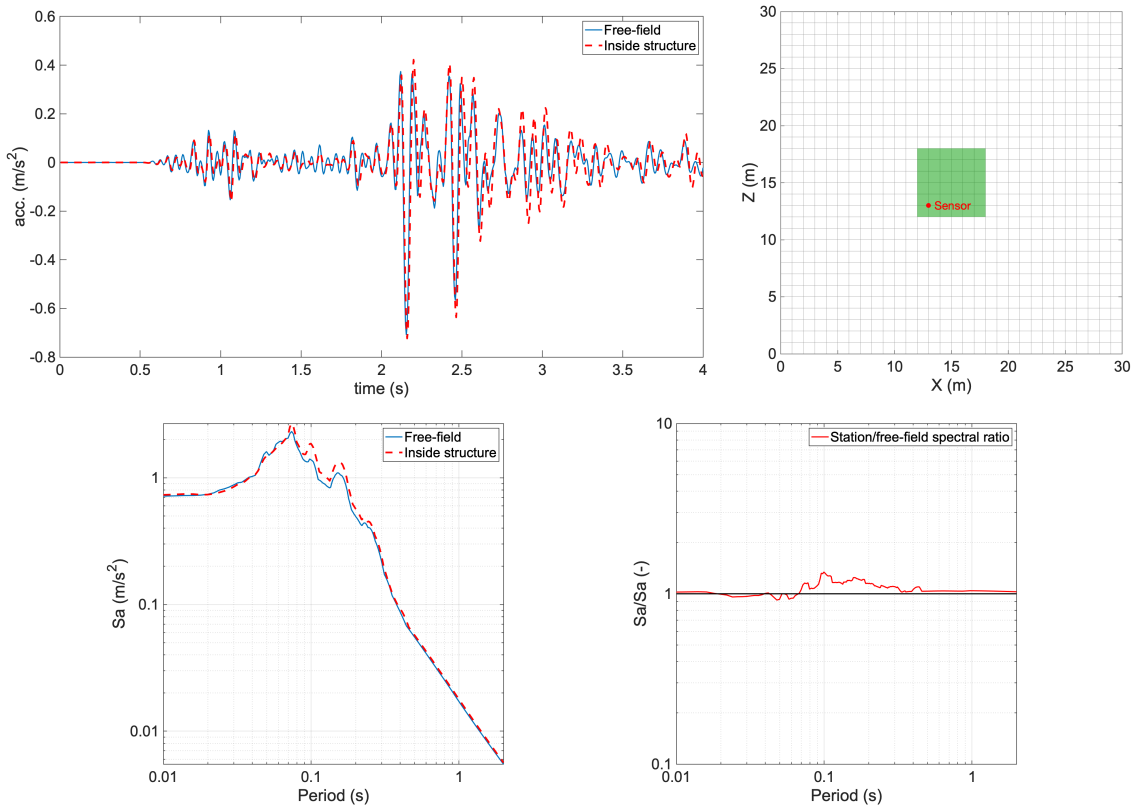


**Figure 7.7 Comparison of surface acceleration signals inside the shed (red dot) and in free-field conditions, considering the G390 profile, for record 23G461, in terms of time-histories, response spectra and spectral ratio.**

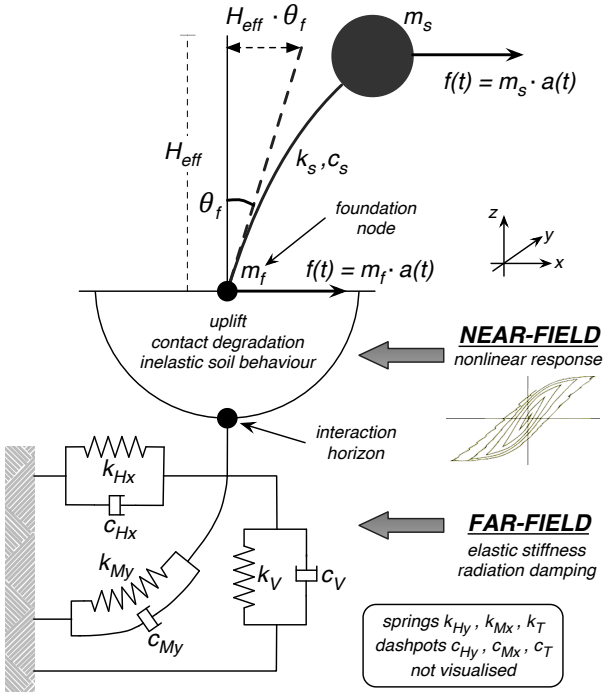


**Figure 7.8 Nonlinear SSI shallow foundations macro-element.**

The results obtained with the alternative macro-element modelling approach proved to be fully consistent with those yielded by the soil-block analyses (see Figure 7.9), including the very slight amplification of low-period spectral ordinates, also observed with the macro-element analyses. However, once the horizontal deformability of the soil was disabled in the macro-element model, thus preventing inertial interaction along the horizontal axis, such slight amplification completely disappeared, thus confirming its origin and once again reassuring the adequacy of the employed soil-block model.

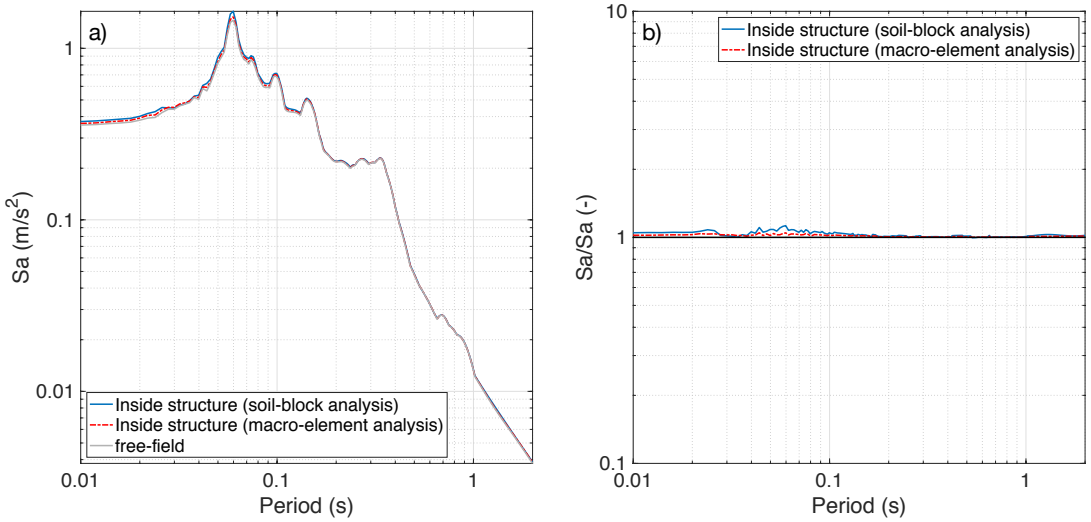


**Figure 7.9 Comparison of surface acceleration signals in free-field conditions, inside the shed (from soil-block analysis) and from a macro-element analysis, considering the BOWW profile, for record 23G461, in terms of a) response spectra and b) spectral ratios (using the free-field signal as reference).**

We took advantage of this nonlinear SSI macro-element model to also numerically check the previously mentioned observations on recordings from instruments mounted on pedestals/plinths or thick slabs being affected by SSI phenomena (Luco et al., 1990; Hollender et al., 2020). Three different concrete bases (Figure 7.10) were thus modelled and analysed, with the numerical results (Figure 7.11) confirming that, indeed, only when slender slabs (such as those seen in the lightweight structures hosting B-stations) are used as a base on which to mount the recording instrument, can SSI effects be avoided. As expected, it was observed that rocking response becomes more and more significant as the thickness of the support increases. (note: in Annex B, similar analyses for a G-station installation are also described)

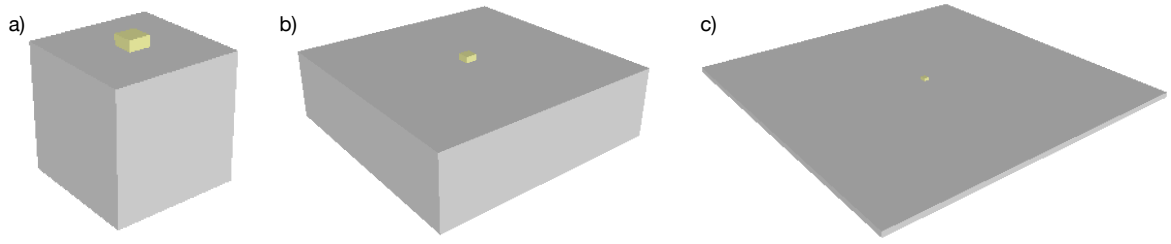


**Figure 7.10 Three concrete bases studied using the nonlinear SSI macro-element model: a) 0.6x0.6x0.6 m³ pedestal/plinth; b) 2x2x0.6 m³ thick slab; c) 6x6x0.1 m³ slender slab (like those seen in the sheds hosting B-stations).**

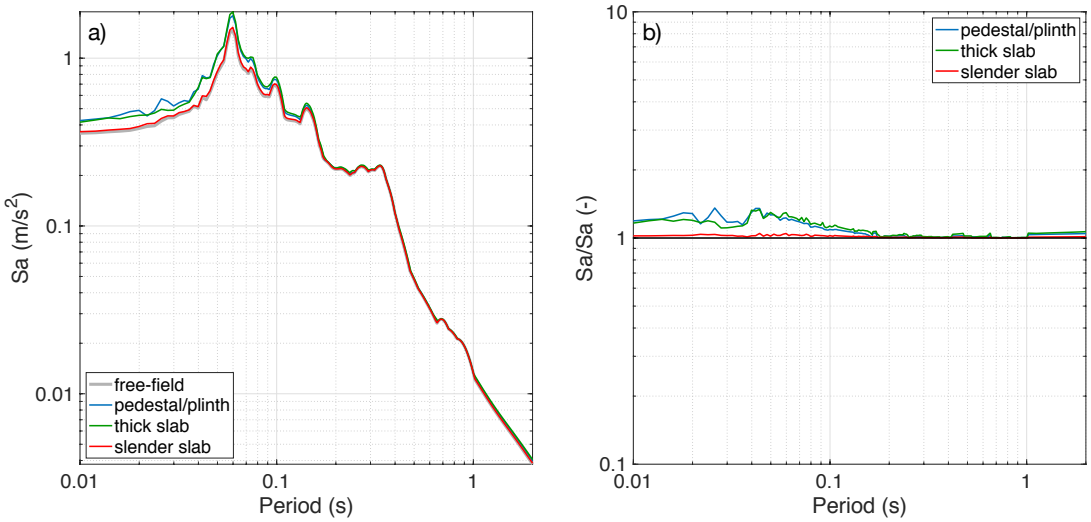


**Figure 7.11 Comparison of surface acceleration signals for three different concrete bases, considering the BOWW profile, for record 23G461, in terms of a) response spectra and b) spectral ratios (using the free-field signal as reference).**

## 7.2 Impact of likely soil consolidation

Having shown that SSI cannot constitute the explanation for the apparent trend for lower high-frequency spectral ordinates noticed in B-station recordings, a potential alternative cause for such observation is herewith explored.

Multiple ground improvement approaches have been developed and employed throughout the years to enhance the mechanical properties of soil prior to construction (see e.g. Mitchell, 1981), which has led the International Society for Soil Mechanics and Geotechnical Engineering (ISSMGE) to list close to 30 different techniques in the ground improvement methods classification distilled by its Technical Committee No. 17 (TC17). As discussed in the state-of-the-art overview by Chu et al. (2009), one of such procedures, *Preloading Using Fill*, applies a temporary load on to the ground prior to the construction of the structure to pre-consolidate compressible soil until most of the primary settlement has occurred, so as to increase the bearing capacity and reduce the compressibility of weak ground. It is a relatively inexpensive ground improvement method, even if time-consuming when compared to other available techniques (the rate of consolidation may in any case be accelerated with the insertion of vertical drains in the soil).

In the Groningen region, where the stiffness of the soil is not particularly high, it was not uncommon for soil consolidation through the Preloading Using Fill method described above to be carried out before the construction of a new structure, especially when the latter was to be grounded on shallow footings, rather than on pile foundations. This implies that the top 2-5 metres of soil directly underneath the structures hosting the B-network stations could feature mechanical properties that are enhanced with respect to soil where no construction is present (as in where the G-network stations have been installed).

The experimental verification of the above hypothesis (of shallow soil layers underneath B-stations being systematically stiffer than their G-station counterparts) is not necessarily straightforward, given the challenges in drilling boreholes for geotechnical and geophysical characterisation in soil that is directly underneath existing foundations. However, one may use the soil-block model developed in this work to assess if an improvement of the mechanical

properties of the very upper layers of soil could explain the observed low-period spectral ordinates attenuation.

Hence, a new set of analyses was deployed, whereby the mechanical properties (shear wave velocity, $V_S$, the unit volume weight, $\gamma$, and the degradation curves) in the upper two metres of soil underneath the structure were enhanced to values similar to those found in deeper layers (see Figure 7.12 and Figure 7.13, showing the increase in terms of shear wave velocity at those shallow layers, for the BOWW and BUHZ soil profiles, respectively). It is noted that, given the absence of information on the soil consolidation that might have possibly been carried out at these specific locations, the changes in soil properties herein introduced, and the corresponding numerical results, should not be considered in absolute, but rather in relative terms only.

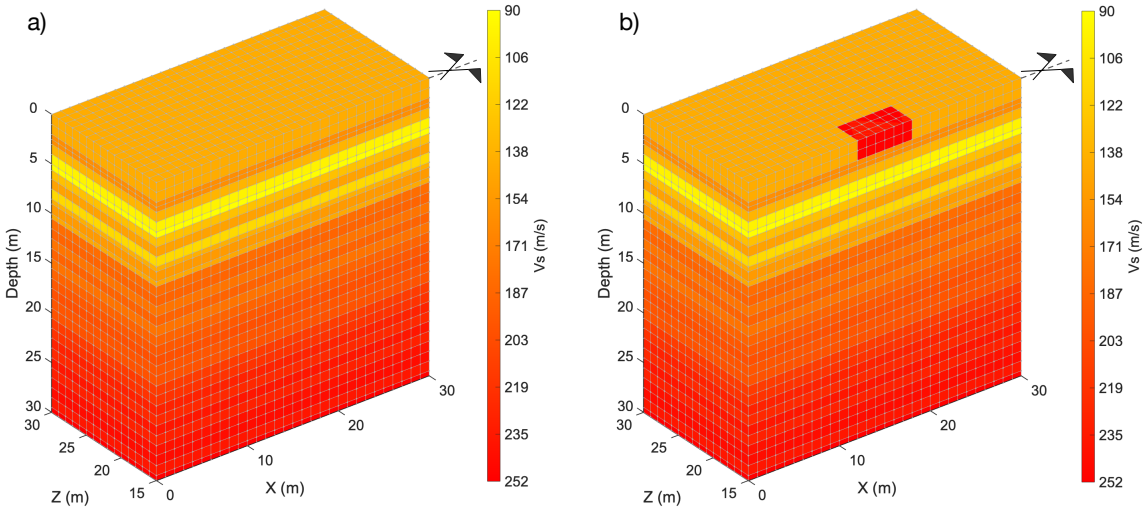


Figure 7.12 Sliced view of a) original and b) consolidated BOWW soil-block model.

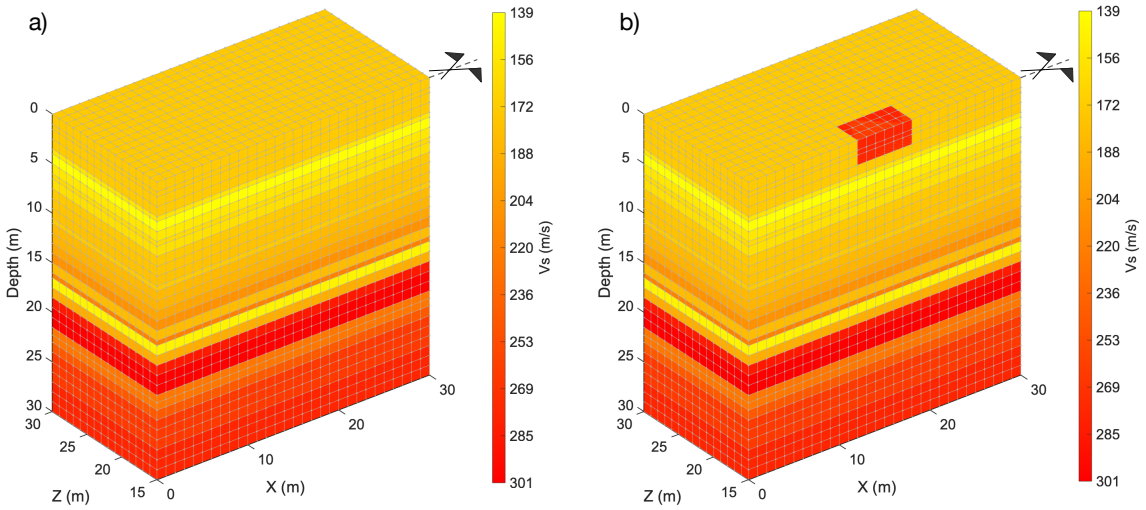


Figure 7.13 Sliced view of a) original and b) consolidated BUHZ soil-block model.

The results from these analyses, which considered four different intensity levels (25G421, 24G111, 23G461, 23G461x3) and two soil profiles (BOWW and BUHZ), are summarised in Figure 7.14 to Figure 7.19, which show comparisons (in terms of acceleration histories, response spectra and spectral ratio) between the surface recordings inside the shed and in free-field conditions. It can be readily observed that the improvement of soil mechanical properties underneath the shed

footprint does lead to attenuation of higher frequencies in the recordings carried out inside the shed (note how the station/free-field spectral ratio features values below 1 for periods below 0.1 s), irrespectively of record intensity or soil profile.

The above effectively indicates that the soil consolidation, that is likely to have been carried out prior to the construction of the structures that are now hosting the B-network stations, could be a possible, if not the only plausible, explanation to the apparent trend for lower high-frequency spectral ordinates noticed in B-station recordings.

Clearly, only after it will become somehow feasible to gain access to the actual mechanical properties of the soil directly underneath the existing foundations of the buildings, will it be possible to fully assert the accuracy of the above findings. Nonetheless, we note that, even if of an obviously distinct nature, somewhat similar observations have been made by Castellaro and Mulargia (2009), when comparing H/V spectral ratios (HVSR, i.e. the ratio between the Fourier amplitude spectra of the horizontal and the vertical components of microtremors) obtained from seismometers installed on natural ground with respect to those obtained from seismometers installed on pavements/asphalt layers, given that the latter, being stiffer than most shallow subsoils, often produce a shear wave velocity inversion.

Finally, it is noted that in Figure 7.14 to Figure 7.19 it is also observed that for period values below 0.05 s, the trend of the spectral ratio plots seems to change. The latter could be a potential artefact of the mesh size of 1 m, which, as discussed already (Section 4.1) may be potentially too coarse to accurately reproduce response frequencies above 20 Hz; a smaller mesh size could not be employed because the ensuing computational cost would have rendered this study unfeasible.

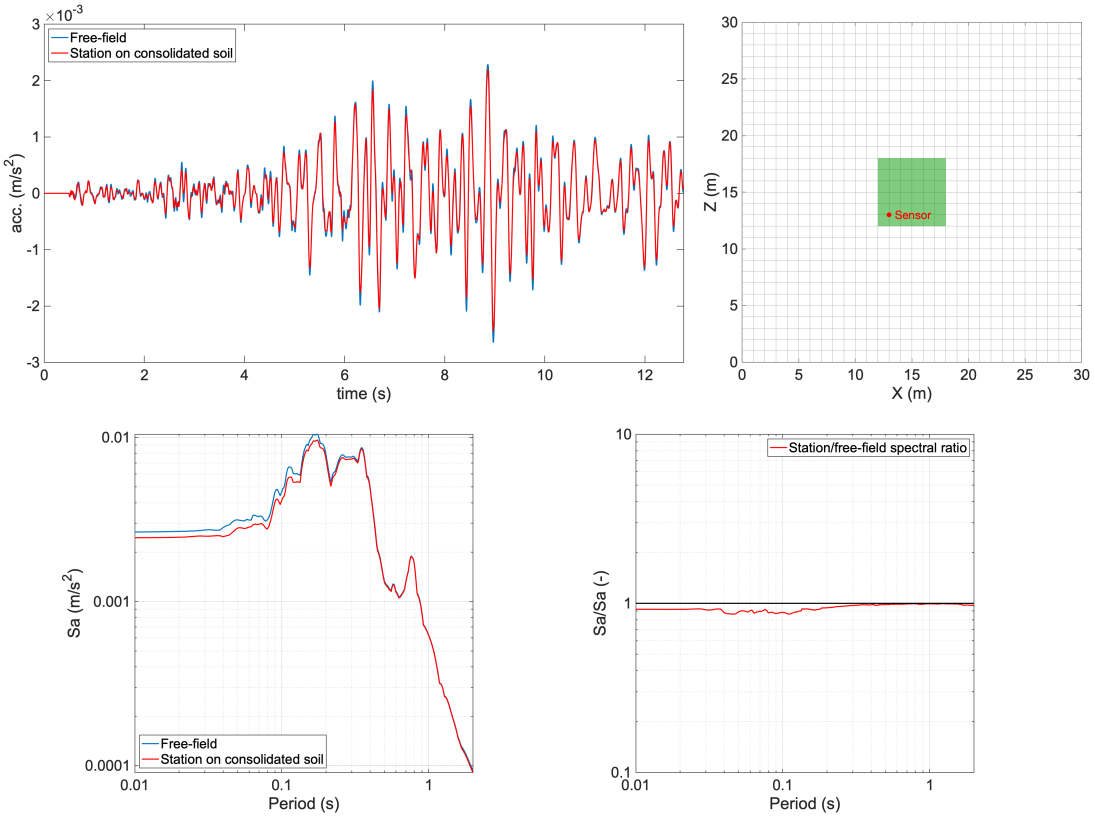


**Figure 7.14 Comparison between surface acceleration signals at free-field and from inside a structure (red dot) on consolidated soil, for the BOWW profile and record 25G421, in terms of time-histories, response spectra and spectral ratio.**

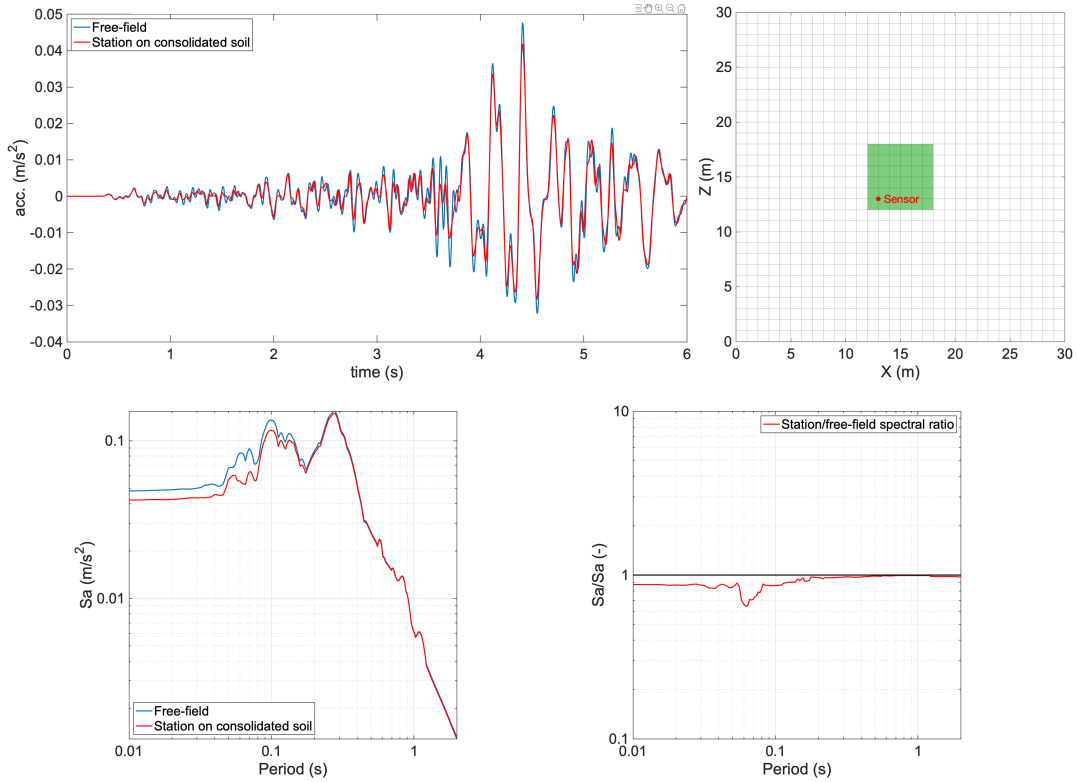


**Figure 7.15 Comparison between surface acceleration signals at free-field and from inside a structure (red dot) on consolidated soil, for the BOWW profile and record 24G111, in terms of time-histories, response spectra and spectral ratio.**

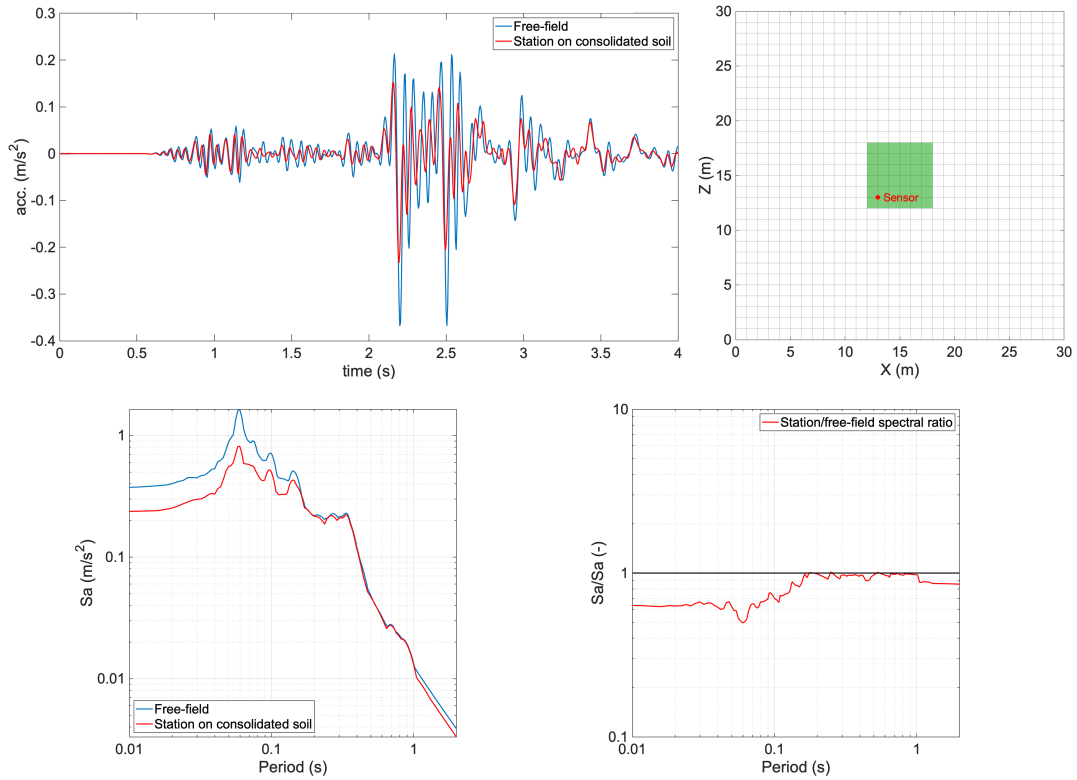


**Figure 7.16 Comparison between surface acceleration signals at free-field and from inside a structure (red dot) on consolidated soil, for the BOWW profile and record 23G461, in terms of time-histories, response spectra and spectral ratio.**

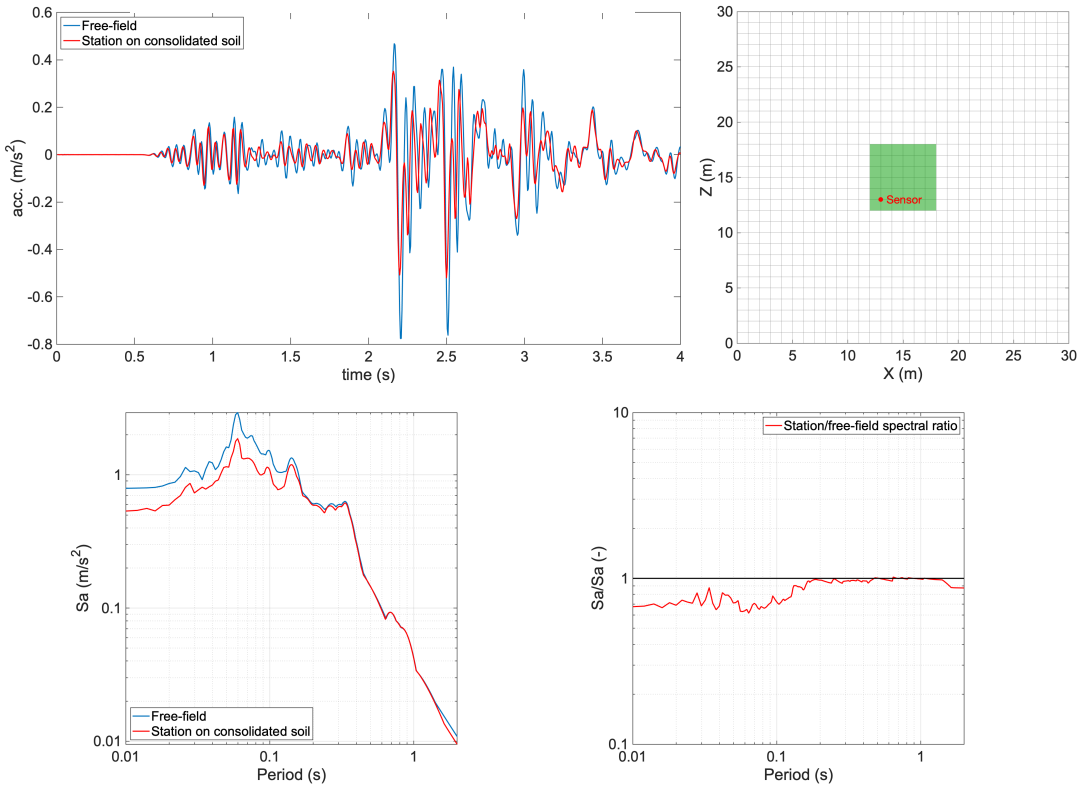


**Figure 7.17 Comparison between surface acceleration signals at free-field and from inside a structure (red dot) on consolidated soil, for the BOWW profile and record 23G461x3, in terms of time-histories, response spectra and spectral ratio.**

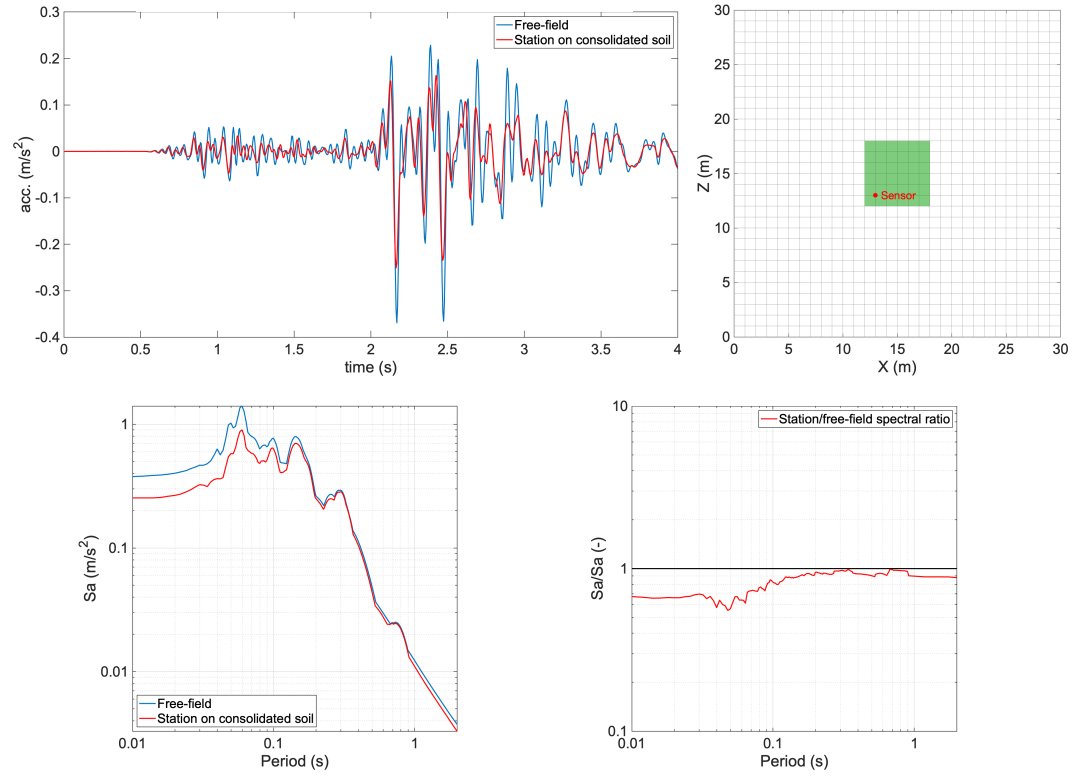


**Figure 7.18 Comparison between surface acceleration signals at free-field and from inside a structure (red dot) on consolidated soil, for the BUHZ profile and record 23G461, in terms of time-histories, response spectra and spectral ratio.**

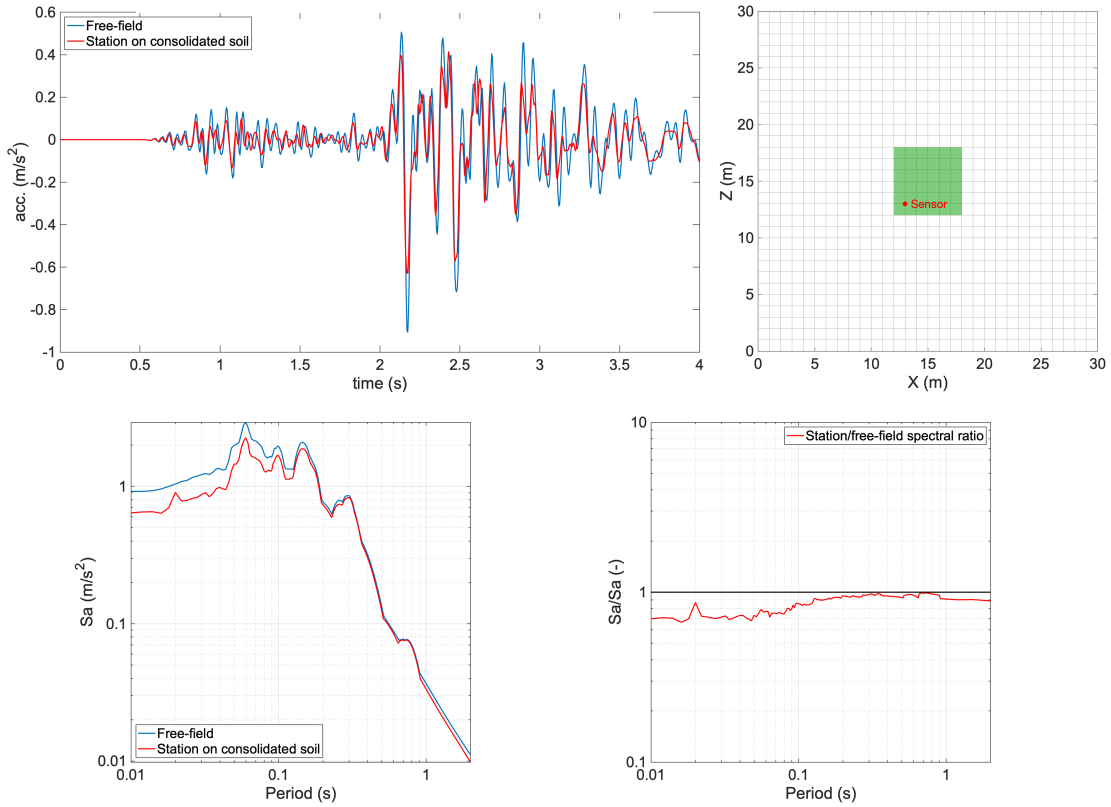


**Figure 7.19 Comparison between surface acceleration signals at free-field and from inside a structure (red dot) on consolidated soil, for the BUHZ profile and record 23G461x3, in terms of time-histories, response spectra and spectral ratio.**

# 8 Conclusions

In this work a nonlinear soil-structure finite element model capable of adequately capturing interaction between soil and structure was developed and verified through a number of analyses and cross-checks.

In one of these preliminary runs of the model, a relatively heavy building with basement was considered. As expected in such cases, the comparison between acceleration histories obtained at basement level against free-field ground motions clearly showed the presence of strong soil-structure interaction, confirming the ability of the model to capture inertial and kinematic SSI effects when these are supposed to be present. It was also demonstratively confirmed that, when required, basement recordings can be adjusted through the employment of embedment and base-slab averaging correction functions available in the literature, such as those described e.g. in NIST (2012).

The numerical model was then employed to check if recordings from instruments located in lightweight structures (like sheds or barns) may or may not be affected by SSI effects, considering soil profiles at the locations of different recording stations in the Groningen field, together with accelerograms from recent events in the region. The ensuing results showed that signals at free-field (G-stations) and from inside the structure (B-stations) are essentially identical, at different intensity levels, effectively precluding the possibility of any relevant SSI effects being developed by lightweight structures hosting B-network stations. Such observations were further confirmed and supported by an additional set of analyses that made use of a nonlinear SSI macro-element, and which assisted also in corroborating the opposing conclusions when thick slabs or pedestals/plinths are employed as a base for the recording instruments.

Having shown that SSI cannot constitute the explanation for the apparent trend for lower high-frequency spectral ordinates noticed in B-station recordings, it was then explored if soil consolidation before the construction of structures resting on shallow foundations (such as the sheds/barns where B-stations are hosted), a typical practice in the region of Groningen, could be a potential cause for the aforementioned observed trend in the ground-motion recordings. The results from this set of analyses, which thus featured improved soil mechanical properties underneath the shed footprint, did show attenuation of high-frequency amplitudes in the accelerograms from inside the shed.

The above implies that considering high-frequency spectral ordinates from B-station recordings in the development of a model to assess earthquake risk for structures sitting on shallow footings, such as e.g. barns and terraced houses (which are also the building typologies with higher seismic vulnerability in the Groningen region), is, in principle, not at all inappropriate. One needs to acknowledge, though, the challenges associated to the characterisation, through geotechnical testing, of the mechanical properties of the soil directly underneath the foundation of existing structures (be them the small houses hosting the recording stations, or the thousands of buildings whose seismic risk is to be assessed). This challenge is not Groningen-specific or constrained, however, but rather applies to most non-piled construction on soft soils anywhere else in the world, given that under the self-weight of buildings all such foundation materials will consolidate and stiffen, particularly near the surface.

## Acknowledgements

This work would not have been possible without the precious data input of Pauline Kruiver, who kindly provided access to the soil mechanical characterisation data and site response analysis results for the Groningen region. Many of the analyses described in this report, and in particular those included in Chapter 7, were driven by the valuable suggestions and insight provided by Julian Bommer, as well as by Brecht Wassing. The crucial roles played by Michael Ntinalexis and Elmer Ruigrok in the organisation of the very informative site visit to the B-network stations is also acknowledged. Finally, we are very thankful to Julian Bommer for his detailed review of a first draft of this report. Further, Michael Ntinalexis provided also the seismic input (i.e. the 50 m deep accelerograms), without which the analyses could not have been ran, as well as the response spectra comparisons between the recordings from “paired” B- and G- stations.

## References

Abrahamson N.A., Schneider J.F., Stepp J.C. [1991] "Empirical spatial coherency functions for application to soil-structure interaction analyses," *Earthquake spectra*, Vol. 7, No. 1, pp. 1-27.

Arup [2015] *External RVS Inspection Full Report Hoofdstraat-West 1, Uithuizen - Groningen Earthquakes – Structural Upgrading*, Report N. 9981AA_001_000_BE_REP_001. Version 6.3 | March 2015.

Bycroft G.N. [1978] "The effect of soil-structure interaction on seismometer readings," *Bulletin of Seismological Society of America*, Vol. 68, pp. 823-843.Castellaro S., Mulargia F. [2009] "The effect of velocity inversions on H/V," *Pure and Applied Geophysics*, Vol. 166, No. 4, pp. 567-592.

Cavalieri F., Correia A.A., Crowley H., Pinho H. [2020] "Dynamic Soil-Structure Interaction models for fragility characterisation of buildings with shallow foundations," *Soil Dynamics and Earthquake Engineering*, Vol. 132, 106004.

Chu J., Varaksin S., Klotz U., Mengé P. [2009] "State-of-the-art report: Construction Processes;" *Proceedings of the 17th International Conference on Soil Mechanics & Geotechnical Engineering: TC17 meeting on ground improvement*, Alexandria, Egypt, 7 October 2009.

Correia A.A., Paolucci R. [2020] "A 3D coupled nonlinear shallow foundation macro-element for seismic soil-structure interaction analysis," *Earthquake Engineering and Structural Dynamics*, submitted for publication.

Darendeli M. [2001] *Development of a new family of normalized modulus reduction and material damping curves*, Ph.D. Thesis, Department of Civil Engineering, University of Texas, Austin, Texas.

Dost B., Ruigrok E., Spetzler J. [2017] "Development of seismicity and probabilistic hazard assessment for the Groningen gas field," *Netherlands Journal of Geosciences*, Vol. 96, No. 5, pp. s235-s245.

Hollender F., Roumelioti Z., Maufroy E., Traversa P., Mariscal A. [2020] "Can we trust high-frequency content in strong-motion database signals? Impact of housing, coupling, and installation depth of seismic sensors," *Seismological Research Letters*, Vol. 91, No. 4, pp. 2192–2205.

Joyner W.B., Chen A.T. [1975] "Calculation of nonlinear ground response in earthquakes," *Bulletin of the Seismological Society of America*, Vol. 65, No. 5, pp. 1315-1336.Kottke A.R., Rathje E.M. [2008] *Technical manual for Strata*, Report No.: 2008/10. Pacific Earthquake Engineering Research Center, University of California, Berkeley.

Kruiver P.P., van Dedem E., Romijn R., de Lange G., Korff M., Stafleu J., Gunnink J.L., Rodriguez-Marek A., Bommer J.J., van Elk J., Doornhof D. [2017] "An integrated shear-wave velocity model for the Groningen gas field, The Netherlands," *Bulletin of Earthquake Engineering*, Vol. 15, No. 9, pp. 3555–3580.

Luco J.E., Anderson J.G., Georgevich M. [1990] "Soil–structure interaction effects on strong motion accelerograms recorded on instrument shelters," *Earthquake Engineering and Structural Dynamics*, Vol. 19, pp. 119–131.

Lysmer J., Kuhlemeyer R.L. [1969] "Finite dynamic model for infinite media," *Journal of the Engineering Mechanics Division*, Vol. 95, No. 4, pp. 859-878.

McKenna F., Fenves G.L., Scott M.H., Jeremic B. [2000] *OpenSees: Open system for earthquake engineering simulation*, Pacific Earthquake Engineering Research Center, University of California, Berkeley, USA. Available at http://opensees.berkeley.edu.

Menq F. Y. [2003] *Dynamic properties of sandy and gravelly soils*, Ph.D. Thesis, Department of Civil Engineering, University of Texas, Austin, Texas.

Mitchell J.K. [1981] "Soil improvement: state of the art report," *Proceeding of the 10th International Conference on Soil Mechanics and Foundation Engineering*, pp. 509-565.

NIST - National Institute of Standards and Technology [2012] *Soil-Structure Interaction for Building Structures*, Report n. 12-917-21, September 2012.

Ntinalexis M, Bommer J.J., Ruigrok E., Edwards B., Pinho R., Dost B., Correia A.A., Uilenreef J., Stafford P.J., van Elk J. [2019] "Ground-motion networks in the Groningen field: usability and consistency of surface recordings," *Journal of Seismology*, Vol. 23, No. 6, pp. 1233-1253.

Petridis C., Pitilakis D. [2018] "Soil-structure interaction effect on earthquake vulnerability assessment of moment resisting frames: the role of the structure," in *Proceedings of the 16th European Conference on Earthquake Engineering*, Thessaloniki, Greece, 18-21 June 2018.

Rodriguez-Marek A., Kruiver P.P., Meijers P., Bommer J.J., Dost B., van Elk J., Doornhof D. [2017] "A regional site-response model for the Groningen gas field," *Bulletin of the Seismological Society of America*, 107(5), 2067–2077.

Seismosoft [2020] *SeismoStruct 2020 - A computer program for static and dynamic nonlinear analysis of framed structures*, available at: http://www.seismosoft.com. [Accessed 22 September 2020].

Sotiriadis D., Klimis N., Margaris B., Sextos A. [2019] "Influence of structure–foundation–soil interaction on ground motions recorded within buildings," *Bulletin of Earthquake Engineering*, Vol. 17, No. 11, pp. 5867-5895.

Sotiriadis D., Klimis N., Margaris B., Sextos A. [2020] "Analytical expressions relating free-field and foundation ground motions in buildings with basement, considering soil-structure interaction," *Engineering Structures*, Vol. 216, 110757.

Stewart J.P. [2000] "Variations between foundation-level and free-field earthquake ground motions," *Earthquake Spectra*, Vol. 16, No. 2, pp. 511-532.

Stafford P.J., Zurek B.D., Ntinalexis M., Bommer J.J. [2019] "Extensions to the Groningen ground-motion model for seismic risk calculations: component-to-component variability and spatial correlation," Bulletin of Earthquake Engineering, Vol. 17, pp. 4417-4439.

van Elk J., Bourne S.J., Oates S., Bommer J.J., Pinho R., Crowley H. [2019] "A probabilistic model to evaluate options for mitigating induced seismic risk," *Earthquake Spectra*, Vol. 35, No. 2, pp. 537–564.

Veletsos A.S., Prasad A.M. [1989] "Seismic interaction of structures and soils: Stochastic approach," *Journal of Structural Engineering*, Vol. 115, No. 4, pp. 935-956.

Witteveen+Bos [2019] *Dynamic amplification effects for B-stations due to building response*, Report 113982/19-009.783. 12 June 2019.

# Annex A: Embedment and incoherence correction of basement recordings

This annex describes the procedure through which one may correct the B-station acceleration recordings obtained from instruments installed in buildings with a basement (BUHZ, BWIN, BZN1). Such procedure aims at correcting the effects of kinematic interaction, which are due to the foundation's structural stiffness, the basement's embedment, as well as the base-slab averaging. The latter results from adjustment of spatially variable ground motions that would be present within the envelope of the foundation, which are averaged within the foundation footprint due to the stiffness and strength of the foundation system (NIST, 2012). Applying the corrections, the original signals, recorded in the basement, are thus transformed into "estimated free-field" signals at surface.

### *Building properties*

Table A.1 summarises the building properties employed in the computation of the signal correction transfer functions. By sketching the footprint border of each building in Google Maps, as shown in Figure A.1, Figure A.2 and Figure A.3 for the three buildings, the footprint area $A$ was computed automatically by the web platform. The definitions of the equivalent dimensions $B$ and $L$, as well as $z_p$, can be found in the subsequent section. The building height, $H$, was estimated on the basis of existing drawings (for BUHZ), tested full-scale buildings of the same typology (for BWIN) and Google Maps 3D view (for BZN1). Concerning the building weight, $W$, reference was made to a portion of the building with basement on top of the BUHZ profile, which is shown in Figure 4.3 of this report. It has a 16x16 m base slab and total height (basement $D$ + superstructure $H$) equal to (2.5 + 8) = 10.5 m. Its volume is thus $V_{ref}$ = 2688 m$^3$, while its weight was estimated to be $W_{ref}$ = 3560 kN. The proportion between weight and volume for the reference building was applied to the three buildings considered herein, whose weight was thus computed as:

$$\frac{W_{ref} \cdot [A \cdot (D + H)]}{V_{ref}} \qquad \text{(A.1)}$$

**Table A.1: Building properties employed in the computation of the signal correction transfer functions.**

| Profile/ Building | Height of basement, $D$ (m) | Footprint area, $A$ (m$^2$) | Equivalent dimensions, $B = L$ (m) | $z_p$ (m) | Height, $H$ (m) | Weight, $W$ (kN) |
|---|---|---|---|---|---|---|
| BUHZ | 2.5 | 888 | 29.8 | 15.0 | 8 | 12349.0 |
| BWIN | 1.0 | 155 | 12.4 | 6.0 | 4 | 1026.4 |
| BZN1 | 2.5 | 217 | 14.7 | 7.5 | 6 | 2442.9 |

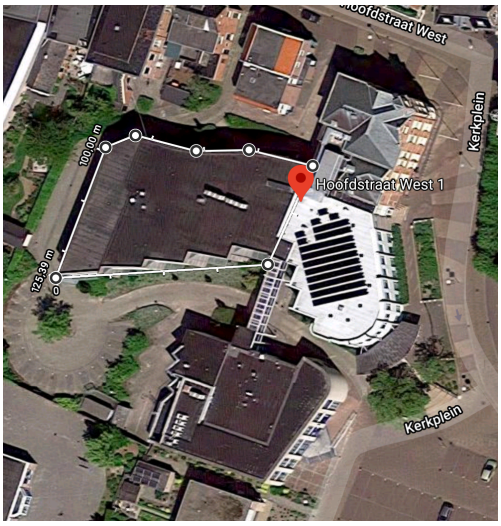


Figure A.1 Considered footprint (border shown with white line and dots) for the BUHZ building.

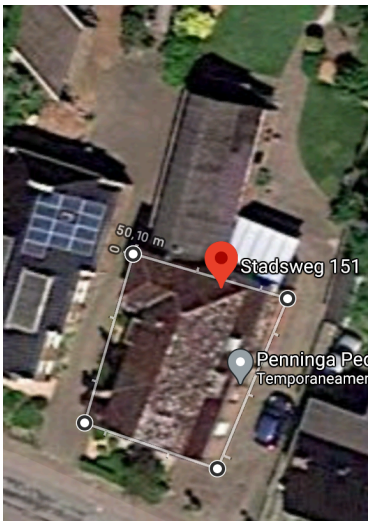


Figure A.2 Considered footprint (border shown with white line and dots) for the BWIN building.

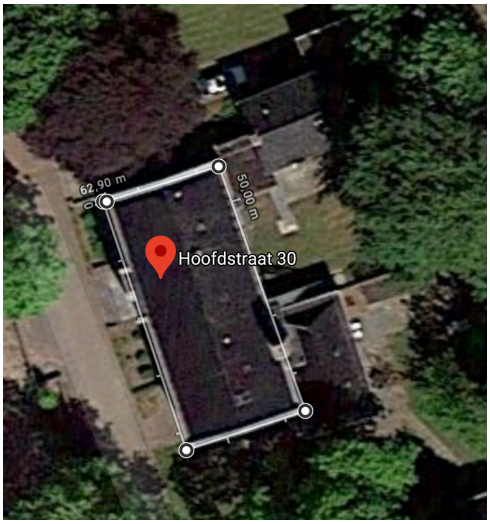


Figure A.3 Considered footprint (border shown with white line and dots) for the BZN1 building.

### *Average shear wave velocity for non-uniform soil profiles*

Based on the in-situ measurements and site response model for the Groningen region (Kruiver et al. 2017, Rodriguez-Marek et al. 2017), the mean effective stress was computed at the mid-point of each soil layer using the values of $\ln(\sigma_m'/p_a)$, where $p_a$ is the atmospheric pressure of 101.325 kPa. The earth pressure coefficient at rest, $k_0$, was also provided and the vertical effective stress, $\sigma_v'$, was thus computed according to:

$$\sigma_m' = \frac{1}{3}(\sigma_v' + 2\sigma_h') = \frac{1}{3}(1 + 2k_0)\sigma_v' \tag{A.2}$$

Subsequently, the water table level at the free-field was determined in order to get the same values of $\sigma_v'$ at depth from the unit weight of the soil. Water table depths resulted to be 1 m for all three profiles.

After assessing the weight of the building (as described above) and its equivalent plan dimensions $B$ and $L$ (an equivalent square foundation was considered, leading to $B = L = \sqrt{A}$ ), the overburden stresses due to the building weight below the basement depth, $D$, were determined assuming a 45º spanning of the soil stresses with depth:

$$\Delta\sigma_v = \frac{W}{[B + 2(z - D)][L + 2(z - D)]} \tag{A.3}$$

Note that this corresponds to a total stress increase which is equal to the corresponding effective stress increase. In fact, any increase in porewater pressure due to the building weight causes a potential flow of the excess porewater pressure which is assumed to have disappeared a few months after the construction of the building.

The overburden-corrected shear wave velocities may then be determined assuming i) a linear variation of the soil shear modulus with effective mean soil stress, i.e. $n$=1, ii) a variation of the effective mean soil stress proportional to the vertical effective stress, i.e. $k_0$ constant, and iii) the fact that the shear wave velocity is proportional to the square root of the soil modulus, i.e. $G_{max} = \rho\, V_s^2$. The corrected shear wave velocity is then given by (NIST, 2012):

$$V_{s,F} = V_s \left(\frac{\sigma_v' + \Delta\sigma_v}{\sigma_v'}\right)^{n/2} \tag{A.4}$$

For the purpose of the analysis of kinematic interaction effects, the average value of the shear wave velocity below the basement level may be computed on the basis of the travel-time of shear wave velocities within a depth $z_p$ equal to the half-dimension of an equivalent square foundation matching the area of the entire building footprint, i.e. $z_p = \sqrt{A/4}$ (see the report by NIST, 2012). It thus becomes:

$$V_{s,avg} = \frac{z_p}{\sum_{i=1}^{nl} z_i / V_{s,Fi}} \tag{A.5}$$

where *nl* is the number of layers, each with thickness $z_i$, in $z_p$. Note that the $z_p$ value was rounded so as to correspond to the sum of thicknesses of the *nl* layers over which the average $V_s$ is calculated. The values of $V_{s,avg}$ resulted to be 180.7 m/s, 101.8 m/s and 137.8 m/s for the BUHZ, BWIN and BZN1 profiles, respectively.

### *Transfer functions and signal correction*

In order to correct recordings obtained from instruments installed in buildings with basement, one or more transfer functions are needed. A transfer function expresses the ratio between the

Fourier transforms of the foundation input motion, $u_{FIM}$, and the free-field surface ground motion, $u_g$.

The two transfer functions considered herein are reported in Equations (6.1), (6.2) and (6.3) of this report. The first one, $H_{u,1}$, aims at correcting the effects of the foundation's structural stiffness and basement's embedment, while the second one, $H_{u,2}$, aims at correcting the base-slab averaging effect, occurring when seismic waves are incoherent. Incoherence of the incident waves at two different points means that they have variations in their phase angle (NIST, 2012). The member in $H_{u,2}$ containing the modified Bessel functions, zero and first order, $I_0$ and $I_1$, can be approximated as:

$$\left(I_0(2b_0^2) + I_1(2b_0^2)\right) = \begin{cases} 1 + b_0^2 + b_0^4 + \dfrac{b_0^6}{2} + \dfrac{b_0^8}{4} + \dfrac{b_0^{10}}{12} & \text{for } b_0 \leq 1 \\ \exp(2b_0^2)\left[\dfrac{1}{\sqrt{\pi}b_0}\left(1 - \dfrac{1}{16b_0^2}\right)\right] & \text{for } b_0 > 1 \end{cases} \quad \text{(A.6)}$$

Using expressions (6.1), (6.2) and (6.3), the two transfer functions for the three profiles/buildings were thus obtained, as shown in Figure A.4, Figure A.5 and Figure A.6. Both horizontal components of the signals originally recorded in BUHZ, BWIN, BZN1 may then then be corrected by following these steps:

1. The signal is first converted from the time domain to the frequency domain. To this aim, the discrete Fourier transform (DFT) of the signal is computed through a fast Fourier transform (FFT) (e.g. by using the function implemented in the software Matlab (The MathWorks Inc, 2019));
2. The DFT is divided by ($H_{u,1}$ * $H_{u,2}$), thus applying both corrections cumulatively;
3. The signal is finally converted back to the time domain applying the inverse Fourier transform to the corrected DFT obtained in point 2. above.

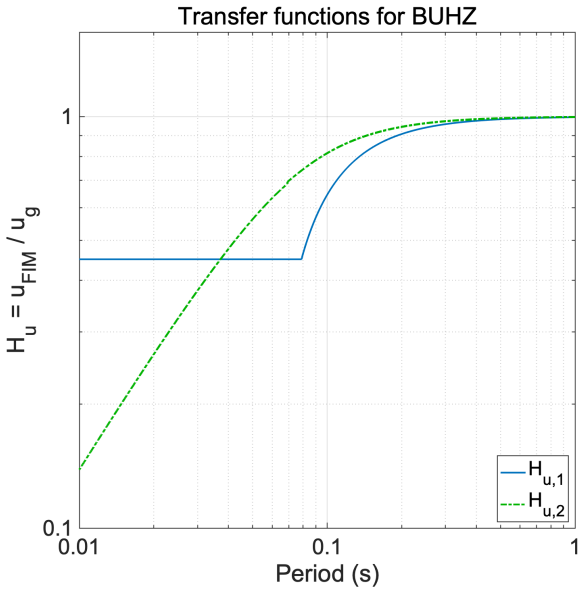


Figure A.4 Transfer function for BUHZ.

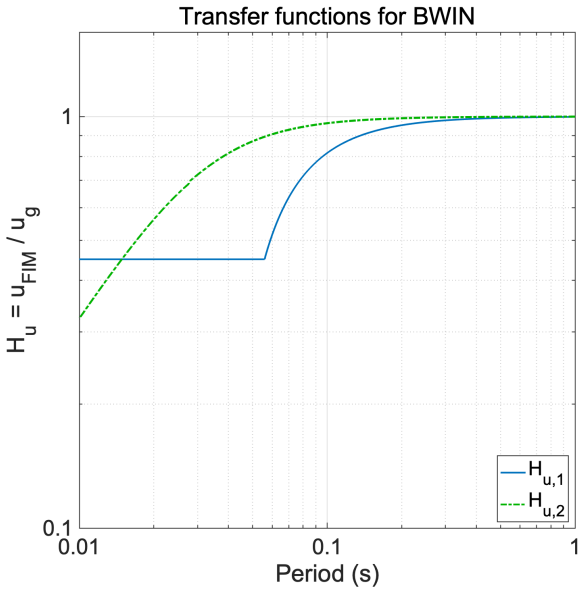


Figure A.5 Transfer function for BWIN.

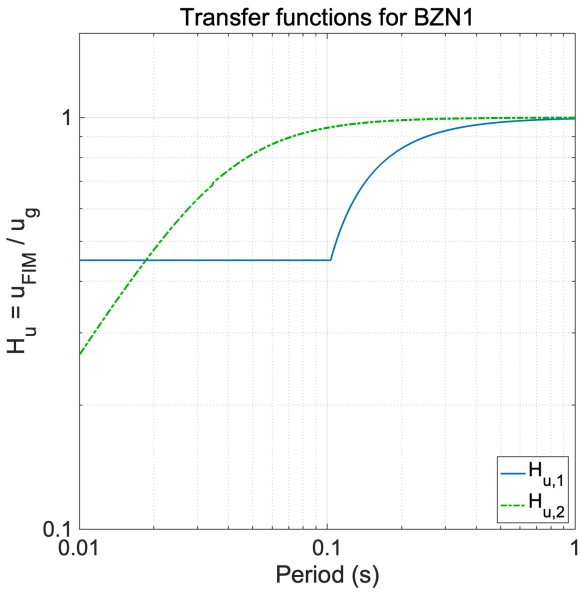


Figure A.6 Transfer function for BZN1.

It is noted and acknowledged that, given their reliance on superposition principles, the above transfer functions are strictly valid only in case of linear response of the soil. This does not constitute a major impediment in the present case, given that, notwithstanding the relatively low strength of the soil in the Groningen region, the intensity of the ground motions generated by the gas-extraction induced events is not sufficient to push the soil into a highly inelastic range, as shown in Section 6.3 above.

It is also underlined that these corrective transfer functions are of an empirical and approximative nature, and that further studies would be needed to better scrutinise the level of accuracy associated to their application to the basement recordings in Groningen. Nonetheless, the results shown in Section 6.6 do already lend some confidence to their employment in the present context.

# Annex B: Investigation of SSI effects in G-stations

We took advantage of the investigation on SSI effects carried out for B-stations (see the final part of Section 7.1 of this report) to check also the behaviour of the concrete slabs of the G-stations in the Groningen field (Figure B.1a). The G-station cabinet and the small concrete slab (2x1x0.14 m) on which it is anchored were thus also modelled in SeismoStruct, together with the nonlinear macro-element (Figure B.1b). The surface 23G461 recording was used as input.

The results shown in Figure B.2 confirm that, as expected, no SSI effects of notice are present. The very slight amplification of low-period spectral ordinates is, again, caused by the horizontal deformability of the soil, discussed already in Section 7.1.

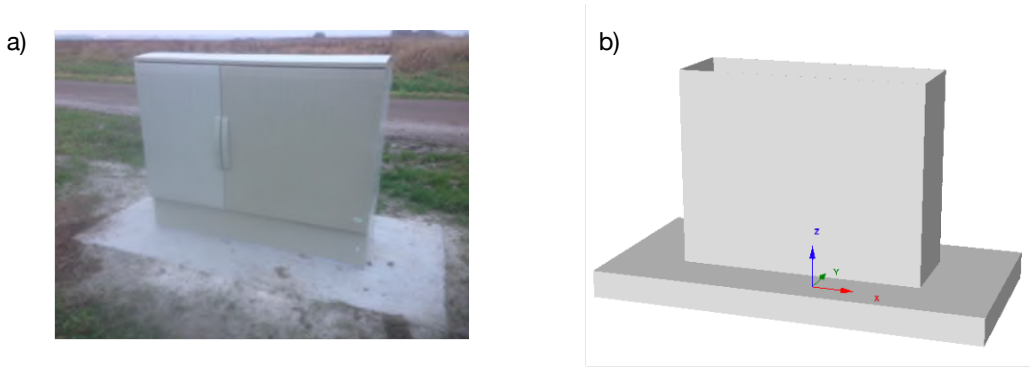


**Figure B.1 a) Typical G-station in the Groningen region; b) G-station model in SeismoStruct.**

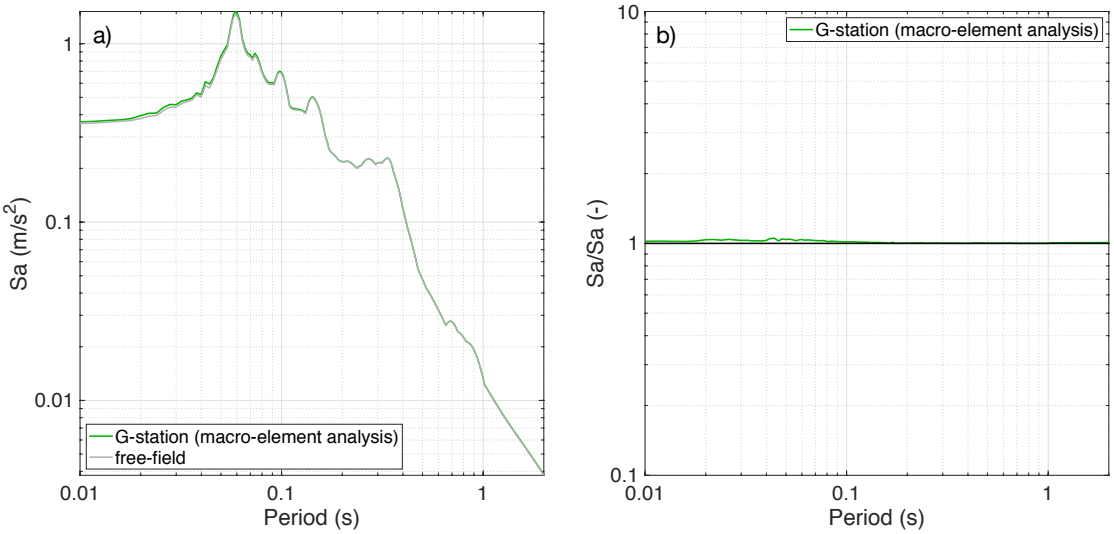


**Figure B.2 Comparison of surface acceleration signals in free-field conditions and from a macro-element analysis with the G-station model, considering the BOWW profile, for record 23G461, in terms of a) response spectra and b) spectral ratios.**